Julius-Maximilians Universität, Würzburg

Institut für Physikalische und
Theoretische Chemie

Exciton Coupling in Valence and Core Excited Aggregates of π-Conjugated Molecules

Dissertation zur Erlangung des
naturwissenschaftlichen Doktorgrades
der Julius-Maximilians-Universität Würzburg

vorgelegt von

Wenlan Liu

aus Neijiang, China

Würzburg 2011

Eingereicht bei der Fakultät für Chemie und Pharmazie am

_____

Gutachter der schriftlichen Arbeit

1. Gutachter:_____

2. Gutachter:_____

Prüfer des öffentlichen Promotionskolloquiums

1. Prüfer:_____

2. Prüfer:_____

3. Prüfer:_____

Datum des öffentlichen Promotionskolloquiums

_____

Doktorurkunde ausgehändigt am

_____

献给我挚爱的妻子
和
我们的女儿

Acknowledgements

While I was studying in this nice city for my Ph. D. degree, I have received a lot of help from many people regarding academic and non-academic issues. These good memories will stay with me for my whole life. I would like to express my sincere appreciation to them.

- First, I would like to thank my supervisor, who is also a good teacher and a kind and responsible person with great humor, Prof. Dr. Bernd Engels. Thank you for providing me this wonderful research topic and sharing your knowledge with me. It is really a pity that I can't drive which lost me many chances to talk to you. This is truly one of the reasons that I couldn't make my Ph. D. work even better.

- It is really my great luck that PD. Dr. Reinhold R. Fink was always extremely patient to any of all my questions, including the stupid ones. In each individual conversation, you either give me some wonderful ideas for solving problems or emphasize key points for understanding abstract quantum chemical theories. Besides the specific academic issues, the most treasured thing that I learned from you is your serious attitude towards the scientific research.

- I would like to thank Prof. Dr. Ingo Fisher for your agreement to be a referee in my Ph. D. degree defense.

- I would also like to thank Prof. Dr. Martin Kaupp and Prof. Dr. Volker Engel for making the examinations which allowed me to proceed my Ph. D. work here without a Master's Degree. I also learned much during the preparation for the exams.

- I have been working together with Volker Settels for two and a half years. We had many useful discussions which often gave me ideas to proceed my

work. I am also thankful for your works on writing the method validation paper and other calculation works for me as well as correcting my papers and thesis. Privately, you are also a nice guy who would like to help the people around you. I really enjoyed the time with you.

- I am indebted a lot to Prof. Dr. Hongmei Zhao. Your work of predicting the potential energy surface of the PBI dimer provides a comfortable starting point to my Ph. D. work. At the very beginning of my arrival in Würzburg, you are the one who gave me the most help concerning living and working. In my heart I already took you as my sister.

- Philipp H. P. Harbach and Prof. Dr. Andreas Dreuw have helped me calculating the excited states of PBI dimer with LC functionals in the method validation paper. I appreciate your efforts to this part of my work.

- I would like to thank Dr. Florian Holch and PD. Dr. Achim Schöll that your findings in the NEXAFS spectra of NTCDA provide me a nice topic to work with.

- Part of my thesis work is about an algorithm for calculating the adjugate matrix. Bettina Mai and Prof. Dr. Manfred Dobrowolski helped me a lot on this part of work. I would like to thank them for this.

- Ursula (Uschi) Rüppel was always trying her best to provide me as much convenience as possible. It was before I got to Würzburg, you found a cheap and comfortable flat for me. During my study here, I often had many problems with the complicated bureaucracy and it was you who solved most of the difficulties for me. I would also like to thank you for making the graduate plan for me that ensures my graduation in time.

- Besides many joys that Johannes Pfister brought to me, there were also many serious academic discussions between us. You are also my best "translator" when I receive any German letter. And you are the one who often modifies my English expressions. I am thankful for all the help you gave to me.

- I would like to thank Vera Stehr a lot for your patience to my questions especially those regarding LaTeX. Also thanks for the corrections to my thesis.

- Kay Ansorg helped me starting with LaTeX. Besides, I would also like to thank you for helping me with many personal issuss.

- Besides, I would like to thank all the other group members, Alexander Paasche, Thomas Schmidt, Johannes Becker, Christoph Grebner, Wook Lee, Christof Walter, Max Rieger and Dr. Maxim Tafipolski, as well as those who already left the group, Dr. Prabhat Sahu, Dr. Sebastian Schlund, Dr. Milena Mladenovic, Verena Schulz, Dr. Svetlana Stepanenko, and Dr. Mario Arnone. It is my great pleasure that I once worked together with you.

- I would like to thank all my friends in Würzburg and in Germany that your existences make me feel less homesick. I treasure the friendships with all of you.

- It is lucky for me that I have many possibilities to communicate with people from other research groups. This nice platform is provided by the Research Training School (GRK) 1221 project. I would like to thank all the people in the GRK1221 that I learned much from you.

- Although my German is still limited in simple conversations, I deeply thank the people who ever helped speaking German. Sie sind Frau Almut Lehrmann, Frau Verena Leidl und Frau Dr. Sabine Schmidt.

- I would like to thank Prof. Dr. Guangju Chen and Prof. Dr. Ruozhuang Liu for your kind recommendations to Bernd which made it possible that I was able to study in Bernd's group.

- China Scholarship Council (CSC) has supported my living in Würzburg for three years and GRK1221 for the remaining several months as well as all the expenses regarding the conferences I have attended. I would like to express my greatest appreciations to the two foundations.

- I would like to thank my parents for your support all the time. Also for my grandparents, ants, uncles and cousins, I feel proud to be one of the family.

- I have received the strongest support all the time from my wife Xiaoqian Li. Without you, my Ph. D. work would have been dull and strengthless. I want to thank you for being pregnant with our first daughter. I am even more proud of the title of father than the title of Doctor.

CONTENTS

Zusammenfassung

Im Rahmen dieser Arbeit werden theoretische Modelle zur Beschreibung von Valenz- und Rumpf-angeregten elektronischen Zuständen diskutiert. Im Fall der Valenz-Anregungen wurden time-dependend Hartree-Fock (TD-HF) und time-dependent Dichtefunktionaltheorie (TD-DFT) Methoden mit verschiedenen Funktionalen für ein Perylenbisimid (PBI) System validiert. Eine einfache Analyse der Charaktäre der angeregten Zustände wurde vorgeschlagen, die auf den berechneten Übergangsdipolmomenten basiert. Dieser Ansatz ist allerdings auf Zustände beschränkt, die ein signifikantes Übergangsdipolmoment aufweisen. Deshalb wurde eine allgemeinere und fundiertere Methode entwickelt, die auf einer Analyse der berechneten CIS Wellenfunktion basiert. Darüberhinaus wurde ein literaturbekannter Model-Hamiltonoperator Ansatz von einem lokalisierten Molekülorbitalbild (MO) abgeleitet, das aus der generelleren Analyse-Methode resultiert. Auf diesem Weg ist ein Zugang zu diabatischen angeregten Zuständen und korrespondierenden Kopplungsparametern auf der Basis von ab initio Rechnungen gegeben. Für rumpfangeregte elektronische Zustände wurden drei Methoden für C 1s-angeregte und ionisierte Zustände verschiedener kleiner Moleküle validiert. Darüberhinaus wurde die Basissatzabhängigkeit dieser Zustände untersucht. Anhand der Resultate wurde die frozen core Näherung ausgewählt um rumpfangeregte Zustände von Naphthalintetracarbonsäuredianhydrid (NTCDA) zu berechnen. Um experimentelle Ergebnisse zu erklären, wurde ein Algorithmus entwicklet, der die Exzitonenkopplungsparameter im Fall von nicht-orthogonalen MOs berechnet.

ABSTRACT

This work focuses on theoretical approaches for predicting the valence and core excited states of aggregate systems.
For the valence excitations, TD-HF and TD-DFT with different functionals have been tested at the Perylene bisimide (PBI) system. A simple character analysis method based on the calculated transition dipole moments is proposed. However, this method does not work for excited states without any transition dipole moment. Thus, we proposed a more general and more valid method based on a calculated CIS type wavefunction for the character analysis. Furthermore, a model Hamiltonian method is derived from a localized picture. The energies of the diabatic states and the corresponding coupling parameters were also determined on the basis of *ab initio* calculations.
For the core excitation, three different methods were validated for C 1s-excited and ionized states if several small molecules. Also we tested the basis sets dependence of these core excited states. Based on those results, we chose the frozen core approximation method to evaluate the core excited states of NTCDA molecules. In order to explain the findings in the experiments, we developed an algorithm to evaluate the exciton coupling parameter where non-orthogonal MOs are used.

List of Publications

Most of the work is based on the following publications.

1. "Charge transfer or neutral excited state? The character analysis of excited states in perylene bisimide dimers" Wenlan Liu, Volker Settels, Bernd Engels and Reinhold Fink, in preparation.

2. "How large is the order of magnitude of Davidov splittings in Near Edge X-ray Absorption Fine Structure Spectra of solid samples?" Wenlan Liu, Florian Holch, Bettina Mai, Achim Schöll, Manfred Dobrowolski, Bernd Engels and Reinhold Fink, in preparation.

3. "Excitation energy quenching in perylene based dye aggregates - a computational study." Volker Settels, Wenlan Liu, Reinhold Fink, Jens Pflaum and Bernd Engels, in preparation.

4. "Assessment of TD-DFT and TD-HF based approaches for the prediction of exciton coupling parameters, potential energy curves and electronic characters of electronically excited aggregates." Wenlan Liu, Volker Settels, Philipp H. P. Harbach, Andreas Dreuw, Reinhold F. Fink and Bernd Engels, accepted, Journal of Computational Chemistry.

5. "Electronic structure of organic materials investigated by quantum chemical calculations." Bernd Engels, Wenlan Liu, Johannes Pfister, Volker Settels, Hongmei Zhao and Reinhold Fink, Comprehensive Nanoscience and Technology, 2010, 1, 1-22

List of Presentations

- Poster: "Assessment of quantum chemical approaches for the predition of the properties of electronically excited dye aggregates: perylene bisimide dimers." at Sep. 26^{th} - 30^{th}, 2010, Münster, Germany, Quantum Chemistry for Large and Complex Systems: From Theory to Algorithms and Applications (The 46th Symposium on Theoretical Chemistry).
- Poster: "Quantum chemical computation on possible trapping mechanisms for the exciton transfer in organic dyes." at Mar. 29^{th} - 31^{st}, 2010, Stuttgart-Hohenheim, Germany, International Bunsen Discussion Meeting on Light Harvesting and Solar Energy Conversion.
- Poster: "Analysis of charge transfer and neutral character of excited states in organic solids." at Feb. 7^{th} - 10^{th}, 2010, RWTH Aachen, Germany, WE-Heraeus School on Physics: Density Functional Theory and its Application in Crystallography.
- Poster: "Solid state effects on NEXAFS spectra of π-conjugated organic molecules: a theoretical investigation" at Sep. 8^{th} - 12^{th}, 2009, Neuss am Rheim, Germany, Excited states: From Photophysics to Photobiology (The 45th Symposium on Theoretical Chemistry).
- Poster: "New theoretical tool for an efficient description of energy transfer in crystals." at Mar. 29^{th} - Apr.2^{nd}, 2009, Svendborg, Denmark, Summer School of 'Frontiers in Computational Chemistry'.

Chapter 1

Introduction

In the last decades, π-conjugated smart materials become increasingly important in everyday life.[1,2,3,4,5,6,7,8,9,10,11,12,13] One remarkable example is the application of organic light-emitting diodes[14] (OLED) in small displays. Compared with the liquid crystal displays (LCD), which is one of the most mature technology in this field, OLEDs benefit from better performance such as wider viewing angles, improved brightness, and better power efficiency. Besides, due to the electrical properties of (semi)conductors, organic materials are also used in semi-conducting layers of field-effect transistors (FET).[1,2,15,16] Rubrene-based organic FETs are found to have the highest carrier mobility 20 - 40 $cm^2/(V{\cdot}s)$.[17,18,19]

Another notable application of organic materials is in organic solar cells. They are discussed and developed as cheap substitutes for inorganic solar cells. However, presently the low energy conversion efficiency of organic solar cells is the main bottleneck which limits its usage. This drawback is partially due to the rather inefficient excitation energy transport (EET).[13,20] Computations may be useful for illuminating this inefficient EET,[21,22] but this is still a challenge as the EET in organic materials is determined by the interplay of a multitude of effects. Recent works concerning the exciton transfer process and excited state properties are discussed in detail in the latter sections (see sections 4.1.1, 4.2.1, 4.3.1 and 4.4.1).

In this work, the valence and core excited states for large π-conjugated aggregate systems are investigated by different theoretical approaches. We used a serials of well established quantum chemical procedures to calculate the corresponding physical properties. Their performances are discussed in detail.

For a proper interpretation of the calculations, it is important to know the character of the excited state. For that purpose, we developed a method for analyzing the characters of excited states of aggregate systems. This method has been compared with other analysis methods. Within the character analysis we obtain insight into the character mixing and the coupling between the excited configurations.
Another important property, the exciton coupling parameter V_{EC}, has been studied for both valence and core excited states. An algorithm is proposed for evaluating V_{EC} when non-orthogonal MOs are used. Besides, the electron (hole) transfer parameter is calculated in a model Hamiltonian method. This method allows to determine the energies of the diabatic excited states, their coupling parameters and to perform the character analysis as a function of the geometrical structure of the aggregates.

Chapter 2

Understanding excited states of molecular aggregates

2.1. Character of an aggregate excited state

Excited electronic states in aggregates can have charge transfer (CT) or neutral excited (NE) characters. The definitions of CT and NE states for aggregates are given by Peterlenz[23] in a localized picture. If an electron is excited from an occupied orbital of one monomer to a virtual orbital of itself, this is defined as an NE state (Fig. 2.1 left). Since the excitation is restricted to a single monomer, this type of excitation results in no charge separation. In contradiction to that, in an excited state where an electron is excited from one monomer to another one is called CT state (Fig. 2.1 right). At the first glance, one would assume that a CT excitation introduces a charge separation and a substantially increased dipole moment of the system. However, this is not always true. For example, in a dimer system, it is possible that a CT state includes not only an excitation from molecule A to monomer B, but also an excitation from B to A simultaneously. Those two contributions may introduce same amount of charge separation and compensate each other. This is always the case when the monomers are symmetrical to each other e. g. due to the fact that the geometry of the system has a center of inversion or a mirror plane. An often used way to distinguish the character of an excited state is to look at the corresponding orbitals which are related to the excitation. This predicts the qualitative correct character for an excited state if the corresponding orbitals are localized to each monomer. How-

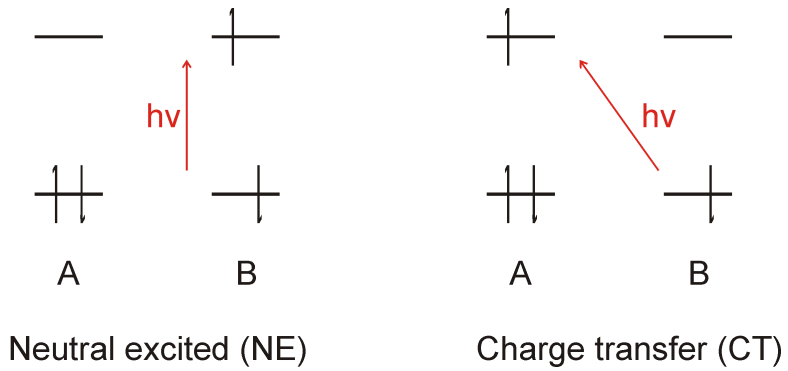

ever, it immediately fails if some of the corresponding orbitals are delocalized to the dimer system, because one can not easily specify the character of the corresponding excitation configuration. Unfortunately, this is often the case for an aggregate system, especially when symmetry is used for the calculation of the reference wavefunction.

2.2. Through a localized picture

Peterlenz[23,24,25,26], Brédas[1,2,27,28,29] and Scholz[30,31] have considered excited states for dimer systems from a localized picture. In this *model Hamiltonian method*, four diabatic configurations are taken into account and allow to calculate the energy and other physical properties of the delocalized excited states. For a dimer system which is composed of the monomers A and B, one first introduces two lowest diabatic NE states and two lowest diabatic CT states. The two NE states refer to excitations from the HOMO of monomer A to the LUMO of the same monomer ($|A^*B\rangle$) and from the HOMO to the LUMO both on monomer B ($|AB^*\rangle$), respectively. The two CT states refer to excitations from the HOMO of monomer A to the LUMO of monomer B ($|A^+B^-\rangle$) and from the HOMO of monomer B to the LUMO of monomer A ($|A^-B^+\rangle$), respectively. These excited states correspond to Peterlenz's definition[23] of NE and CT states in aggregate systems.

The actual states are represented by linear combinations of these configurations which can be obtained by diagonalizing the effective Hamiltonian matrix, a 4×4 matrix introduced by Petelenz. The non-diagonal elements in this matrix are the so called coupling matrix elements or coupling parameters.

$$\begin{pmatrix} \langle A^*B| \\ \langle AB^*| \\ \langle A^+B^-| \\ \langle A^-B^+| \end{pmatrix} \quad \hat{\mathbf{H}} \quad \left(|A^*B\rangle,\ |AB^*\rangle,\ |A^+B^-\rangle,\ |A^-B^+\rangle\right)$$

$$= \begin{pmatrix} E_{\mathrm{NE}} & V_{\mathrm{EC}} & D_e & D_h \\ V_{\mathrm{EC}} & E'_{\mathrm{NE}} & D'_h & D'_e \\ D_e & D'_h & E_{\mathrm{CT}} & W \\ D_h & D'_e & W & E'_{\mathrm{CT}} \end{pmatrix}. \tag{2.2.1}$$

E_{NE} and E'_{NE} are the excitation energies of $|A^*B\rangle$ and $|AB^*\rangle$ states respectively

$$E_{\mathrm{NE}} = \langle \Psi_{AB^*}|\hat{\mathbf{H}}|\Psi_{AB^*}\rangle, \qquad E'_{\mathrm{NE}} = \langle \Psi_{A^*B}|\hat{\mathbf{H}}|\Psi_{A^*B}\rangle. \tag{2.2.2}$$

V_{EC} is the exciton coupling parameter which is the coupling between the two NE states

$$V_{\mathrm{EC}} = \langle \Psi_{AB^*}|\hat{\mathbf{H}}|\Psi_{A^*B}\rangle. \tag{2.2.3}$$

E_{CT} and E'_{CT} are the excitation energies of $|A^+B^-\rangle$ and $|A^-B^+\rangle$ states respectively

$$E_{\mathrm{CT}} = \langle \Psi_{A^+B^-}|\hat{\mathbf{H}}|\Psi_{A^+B^-}\rangle, \qquad E'_{\mathrm{CT}} = \langle \Psi_{A^-B^+}|\hat{\mathbf{H}}|\Psi_{A^-B^+}\rangle. \tag{2.2.4}$$

W is the coupling between these two CT states

$$W = \langle \Psi_{A^-B^+}|\hat{\mathbf{H}}|\Psi_{A^+B^-}\rangle. \tag{2.2.5}$$

D_e $\left(D'_e\right)$ is the coupling between the NE $|A^*B\rangle$ $\left(|AB^*\rangle\right)$ state and the CT $|A^+B^-\rangle$ $\left(|A^-B^+\rangle\right)$ state

$$D_e = \langle \Psi_{A^+B^-}|\hat{\mathbf{H}}|\Psi_{A^*B}\rangle, \qquad D'_e = \langle \Psi_{A^-B^+}|\hat{\mathbf{H}}|\Psi_{AB^*}\rangle. \tag{2.2.6}$$

D_h $\left(D'_h\right)$ is the coupling between the NE $|A^*B\rangle$ $\left(|AB^*\rangle\right)$ state and the CT $|A^-B^+\rangle$ $\left(|A^+B^-\rangle\right)$ state

$$D_h = \langle \Psi_{A^+B^-}|\hat{\mathbf{H}}|\Psi_{AB^*}\rangle, \qquad D'_h = \langle \Psi_{A^-B^+}|\hat{\mathbf{H}}|\Psi_{A^*B}\rangle. \tag{2.2.7}$$

By diagonalizing this matrix, one gets the energies of the considered adiabatic

excited states as well as the expression of their wavefunctions. Furthermore, the character of each excited state is obtained immediately (for more details see section 4.2.5). These coupling parameters are often used for describing related physical phenomenons. For example, the exciton coupling parameter V_{EC}, is widely used for explaining the shift of absorption spectra for aggregate systems[3,32,33,34,35,36,37,38,39,40] and for calculating the exciton transfer rate.[1,35,39,40,41,42,43,44,45,46,47] D_e (D_h) can be used to evaluate the electron (hole) transfer rate[1,2,6,27,28,29,48]. Therefore, it is also called electron (hole) transfer parameter. W is less often discussed because its absolute value is generally much smaller than those of the other coupling parameters.

2.3. Through a supermolecular picture

As mentioned in the last section, there are many kinds of methods which are suitable for calculating excited states of aggregate systems. The most common methods are *configuration interaction* type methods (CI and CASSCF) and *propagator approaches* such as CC2, ADC, TD-DFT and TD-HF. In contrast to the *model Hamiltonian method*, these methods are *first principles* approaches. They require a reference ground state wavefunction for the aggregate system and consider excited configurations based on the reference wavefunction. Therefore, in most cases the MOs of the aggregate system are delocalized to the whole system, and these diabatic configurations no longer fit Peterlenz's definition for NE and CT states. The resulting adiabatic excited states are orthogonal to each other, which means that all the couplings of the diabatic states are already taken into consideration within these methods.

Compared to the *model Hamiltonian method*, these *first principles* methods give more accurate descriptions of the wavefunctions as well as the excitation energies and other physical properties of excited states of the aggregates. On the other hand, each of these methods has its drawbacks. *Configuration interaction* methods provide well defined wavefunction for excited states, but tend to be very expensive and hampered by the notorious size consistency error. In many cases, they extent the calculation limit for normal clusters. An exception is the CIS approach which is, however, often not sufficiently accurate. There are also many kinds of modified CC methods e.g. second-order approximate coupled-cluster (CC2), which is less expensive and yields often an excellent de-

scription for singly excited states. For further discussion of these methods, see section 3.1. The performance of the *random-phase approximation* largely depends on the reference wavefunction used. For example, the TD-HF method, where the HF ground state wavefunction is used as a reference, normally overestimates the excitation energies. Results of the TD-DFT method strongly depends on which exchange-correlation functional is used. In general, the *generalised gradient approximation* (GGA) functionals (BLYP[49,50,51,52,53], PBE[49,50,54,55] etc.) largely underestimate the excitation energy for CT states. Hybrid GGA functionals (B3LYP[49,51,53,56,57], PBE0[49,50,54,55,58] etc.) can improve the description for CT states. They replace a certain amount of the exchange functional by exact exchange. There is clear evidence that these functionals show improved performance for a variety of properties. However, it is hard to find a general way to fit the amount of exact HF exchange to the ground and excited states of different systems. A possible solution to this point is the *long range corrected* (LC) functionals (CAM-B3LYP[59] etc.). In the LC scheme, the exchange functional is partitioned into long-range and short-range parts with respect to the inter-electronic separation. The short-range part is represented by the ordinary exchange-correlation functional, while the long-range part is replaced by an exact exchange functional. This improves the performance for charge transfer states which are poorly described with ordinary or hybrid GGA functionals. However, in some cases, this type of functionals still fails in predicting the correct energy order of excited states (see section 4.1.3).

CHAPTER 3

THEORETICAL METHODS

3.1. ELECTRON CORRELATION METHODS

3.1.1. CONFIGURATION INTERACTION

3.1.1.1. FULL CONFIGURATION INTERACTION

For an N electrons system the electronic ground state wavefunction Φ_0 in the *Hatree-Fock* (HF) approximation is given by a *Slater determinant*

$$\Phi_0 = |\chi_1\chi_2\cdots\chi_N| = \frac{1}{\sqrt{N!}}\begin{vmatrix} \chi_1(\mathbf{x}_1) & \chi_2(\mathbf{x}_1) & \cdots & \chi_N(\mathbf{x}_1) \\ \chi_1(\mathbf{x}_2) & \chi_2(\mathbf{x}_2) & \cdots & \chi_N(\mathbf{x}_2) \\ \vdots & \vdots & \ddots & \vdots \\ \chi_1(\mathbf{x}_N) & \chi_2(\mathbf{x}_N) & \cdots & \chi_N(\mathbf{x}_N) \end{vmatrix}, \tag{3.1.1}$$

where the $\{\chi_1,\chi_2,\cdots\chi_N\}$ are the occupied orthonormal spin orbitals. $\{\mathbf{x}_1,\mathbf{x}_2\cdots\mathbf{x}_N\}$ are the combined spatial and spin coordinates for the electrons. In a Roothaan HF variant, besides the N occupied orbitals, the $M-N$ virtual orthonormal orbitals are also generated by the same SCF procedure. M is the number of basis functions used in the HF calculation. The energy of the ground state is given as

$$E_0 = \frac{\langle\Phi_0|\hat{\mathbf{H}}|\Phi_0\rangle}{\langle\Phi_0|\Phi_0\rangle}, \tag{3.1.2}$$

where $\hat{\mathbf{H}}$ is the electronic Hamiltonian. The HF ground state energy E_0 is still above the exact ground state energy $\mathscr{E}_0$. The difference $\mathscr{E}_0 - E_0$ is defined to be the correlation energy. A possible way is to describe the exact ground state Ψ_0

as a linear combination of a complete configuration set. This complete configuration set can be formed from the HF ground state Ψ_0 and its excited configurations $\{\Phi_1, \Phi_2, \cdots\}$. For clarification, the full configuration set is partitioned by the number excited electrons. Therefore, the exact ground state wavefunction is written as

$$\Psi_0 = a_0\Phi_0 + \sum_{a,i} c_a^i \Phi_a^i + \sum_{\substack{a<b,\\ i<j}} c_{ab}^{ij} \Phi_{ab}^{ij} + \sum_{\substack{a<b<c,\\ i<j<k}} c_{abc}^{ijk} \Phi_{abc}^{ijk} + \cdots, \tag{3.1.3}$$

where $a, b, c\cdots$ represent the occupied and $i, j, k\cdots$ the virtual orbitals. The excited configurations are constructed from the HF ground state *Slater determinant* Φ_0 by substituting the occupied orbitals in the subscript of the configuration, by the virtual orbitals in the superscript of the configuration. For example, a doubly excited configuration Φ_{ab}^{ij} has the following form

$$\Phi_{ab}^{ij} = |\chi_1 \cdots \chi_{a-1}\chi_i\chi_{a+1} \cdots \chi_{b-1}\chi_j\chi_{b+1} \cdots \chi_N| = \frac{1}{\sqrt{N!}} \begin{vmatrix} \chi_1(\mathbf{x}_1) & \cdots & \chi_{a-1}(\mathbf{x}_1) & \chi_i(\mathbf{x}_1) & \cdots & \chi_{b-1}(\mathbf{x}_1) & \chi_j(\mathbf{x}_1) & \cdots & \chi_N(\mathbf{x}_1) \\ \chi_1(\mathbf{x}_2) & \cdots & \chi_{a-1}(\mathbf{x}_2) & \chi_i(\mathbf{x}_2) & \cdots & \chi_{b-1}(\mathbf{x}_2) & \chi_j(\mathbf{x}_2) & \cdots & \chi_N(\mathbf{x}_2) \\ \vdots & \ddots & \vdots & \vdots & \ddots & \vdots & \vdots & \ddots & \vdots \\ \chi_1(\mathbf{x}_N) & \cdots & \chi_{a-1}(\mathbf{x}_N) & \chi_i(\mathbf{x}_N) & \cdots & \chi_{b-1}(\mathbf{x}_N) & \chi_j(\mathbf{x}_N) & \cdots & \chi_N(\mathbf{x}_N) \end{vmatrix}. \tag{3.1.4}$$

Similar to the equation (3.1.2), we obtain the exact ground state energy

$$\mathscr{E}_0 = \frac{\langle\Psi_0|\hat{\mathbf{H}}|\Psi_0\rangle}{\langle\Psi_0|\Psi_0\rangle}. \tag{3.1.5}$$

By inserting the definition of Ψ_0 equation (3.1.3), into the equation (3.1.5), we obtain a general expression for the CI energy which can be minimized diagonal-

izing the so-called *Full-CI* matrix

$$
\begin{array}{c}
 \\
 \\
\langle\Phi_0| \\
\langle\mathbf{S}| \\
\langle\mathbf{D}| \\
\langle\mathbf{T}| \\
\langle\mathbf{Q}| \\
\vdots
\end{array}
\begin{array}{c}
\begin{array}{ccccccc}
 & & \Phi_a^i & \Phi_{ab}^{ij} & \Phi_{abc}^{ijk} & \Phi_{abcd}^{ijkl} & \cdots \\
 & |\Phi_0\rangle & |\mathbf{S}\rangle & |\mathbf{D}\rangle & |\mathbf{T}\rangle & |\mathbf{Q}\rangle & \cdots
\end{array} \\
\begin{pmatrix}
\langle\Phi_0|\hat{\mathbf{H}}|\Phi_0\rangle & 0 & \langle\Phi_0|\hat{\mathbf{H}}|\mathbf{D}\rangle & 0 & 0 & \cdots \\
0 & \langle\mathbf{S}|\hat{\mathbf{H}}|\mathbf{S}\rangle & \langle\mathbf{S}|\hat{\mathbf{H}}|\mathbf{D}\rangle & \langle\mathbf{S}|\hat{\mathbf{H}}|\mathbf{T}\rangle & 0 & \cdots \\
\langle\mathbf{D}|\hat{\mathbf{H}}|\Phi_0\rangle & \langle\mathbf{D}|\hat{\mathbf{H}}|\mathbf{S}\rangle & \langle\mathbf{D}|\hat{\mathbf{H}}|\mathbf{D}\rangle & \langle\mathbf{D}|\hat{\mathbf{H}}|\mathbf{T}\rangle & \langle\mathbf{D}|\hat{\mathbf{H}}|\mathbf{Q}\rangle & \cdots \\
0 & \langle\mathbf{T}|\hat{\mathbf{H}}\rangle|\mathbf{S}\rangle & \langle\mathbf{T}|\hat{\mathbf{H}}|\mathbf{D}\rangle & \langle\mathbf{T}|\hat{\mathbf{H}}|\mathbf{T}\rangle & \langle\mathbf{T}|\hat{\mathbf{H}}|\mathbf{Q}\rangle & \cdots \\
0 & 0 & \langle\mathbf{Q}|\hat{\mathbf{H}}|\mathbf{D}\rangle & \langle\mathbf{Q}|\hat{\mathbf{H}}|\mathbf{T}\rangle & \langle\mathbf{Q}|\hat{\mathbf{H}}|\mathbf{Q}\rangle & \cdots \\
\vdots & \vdots & \vdots & \vdots & \vdots & \ddots
\end{pmatrix}
\end{array}, \tag{3.1.6}
$$

where the single, double, triple and quadruple excitation configurations are simplified as **S**, **D**, **T** and **Q** respectively. Due to *Brillouin's Theorem*,[60] the CI matrix element between the HF ground state Φ_0 and the singly excited configuration vanishes. The Φ_0 has also on interaction with to configurations which are more than doubly excited because of the *Slater-Condon rules*.[60] This rule causes that most CI-matrix elements in the *Full-CI* matrix vanish as well. One can further simplify the matrix by constructing *spin adapted configurations* (SAC), as only SACs with the same total spin interact with each other. For a singlet ground state, the number of singlet SACs for an N electron system with M basis functions is given by[61]

$$
\text{Number of SACs} = \frac{M!(M+1)!}{(\frac{N}{2})!(\frac{N}{2}+1)!(M-\frac{N}{2})!(M-\frac{N}{2}+1)!} \tag{3.1.7}
$$

For an instance, a benzene molecule with TZVPP[62] basis set ($N = 42,\ M = 106$), there are about 1.0×10^{116} SACs. Therefore, the *Full-CI* method is only applicable for small systems with very limited number of basis functions.

3.1.1.2. Configuration interaction singles

As discussed in the last section, the *Full CI* method is generally not applicable. In this section, we are going to introduce the a truncated CI method, which is called configuration interaction singles (CIS). It considers only the singly excited configurations in the CI matrix. Since they have no interaction with the ground state wavefunction, CIS is only meaningful for excited states.

The whole set of singly excited configurations $\{|\Phi_a^i\rangle,\ |\Phi_b^j\rangle\cdots\}$ forms a column vector $\vec{\Phi}$. The CIS matrix $\mathbf{A}$ is given by

$$\mathbf{A} = \vec{\Phi}^T \cdot \hat{\mathbf{H}} \cdot \vec{\Phi}. \tag{3.1.8}$$

The matrix element between the configurations $|\Phi_a^i\rangle$ and $|\Phi_b^j\rangle$ is

$$\langle \Phi_a^i | \hat{\mathbf{H}} | \Phi_b^j \rangle = (E_0 + \varepsilon_a - \varepsilon_i)\delta_{ab}\delta_{ij} - (ia||jb). \tag{3.1.9}$$

Assuming a unitary matrix $\mathbf{U}$ can diagonalize the matrix $\mathbf{A}$, one

$$\mathbf{U}^\dagger \cdot \mathbf{A} \cdot \mathbf{U} = \mathbf{E}. \tag{3.1.10}$$

The diagonal matrix $\mathbf{E}$ immediately gives the energies of all excited states. By inserting equation (3.1.8) to (3.1.10), the configuration vector $\vec{\Phi}$ is transformed to the singly excited state vector $\vec{\Psi}$

$$\mathbf{U}^\dagger \cdot \vec{\Phi}^T \cdot \hat{\mathbf{H}} \cdot \vec{\Phi} \cdot \mathbf{U} = \mathbf{E} \rightarrow \begin{cases} \vec{\Psi} = \vec{\Phi} \cdot \mathbf{U}, \\ \vec{\Psi}^\dagger \cdot \hat{\mathbf{H}} \cdot \vec{\Psi} = \mathbf{E}. \end{cases} \tag{3.1.11}$$

Besides the *Full CI*, CIS is the only size consistent (see appendix B) CI method. That is because of *Brillouin's Theorem*[60] that the CIS ground state is just the HF ground state wavefunction. Since only the singly excited configurations are taken into account in a CIS calculation, this method usually overestimates the excitation energy.

3.1.2. Coupled cluster methods

As we know, the *Full CI* method is not generally applicable and CIS gives no improvement for the ground state and only a qualitatively correct description of excited states. Furthermore, other truncated CI methods suffer a lot form the size consistency problem. Therefore, the *Coupled Cluster* (CC) method is proposed that its any truncated level of theory is size consistent (see appendix B). In intermediate normalization, the CC wavefunction for an N electron system is given as

$$\Psi_{CC} = e^{\mathbf{T}}\Phi_0, \tag{3.1.12}$$

where the reference wavefunction Φ_0 is the HF ground state. The *intermediate normalization* means that the CC wavefunction is not normalized but its overlap with the reference wavefunction is unity

$$\langle \Psi_{CC} | \Phi_0 \rangle = 1, \qquad \langle \Psi_{CC} | \Psi_{CC} \rangle \neq 1. \tag{3.1.13}$$

$\mathbf{T}$ is the so-called 'cluster operator' that generates all possible excited configurations

$$\mathbf{T}\Phi_0 = \sum_{i,a} t_a^i \Phi_a^i + \sum_{\substack{i<j,\\ a<b}} t_{ab}^{ij} \Phi_{ab}^{ij} + \sum_{\substack{i<j<k,\\ a<b<c}} t_{abc}^{iik} \Phi_{abc}^{ijk} + \cdots, \tag{3.1.14}$$

where the t_a^i, t_{ab}^{ij} and t_{abc}^{iik} etc. are the amplitudes for the corresponding excitation configurations. For simplicity, $\mathbf{T}$ is given in the following terms

$$\mathbf{T} = \mathbf{T}_1 + \mathbf{T}_2 + \mathbf{T}_3 + \cdots + \mathbf{T}_N, \tag{3.1.15}$$

that $\mathbf{T}_1$, $\mathbf{T}_2$ and $\mathbf{T}_3$ etc. generate the first, second and third terms in the equation (3.1.14) respectively by operating on Φ_0.
We rewrite the exponential ansatz $e^{\mathbf{T}}$ in equation (3.1.12) into the *Tayler series* and sort them by different excitation levels

$$\begin{aligned} e^{\mathbf{T}} &= 1 + \mathbf{T} + \frac{1}{2}\mathbf{T}^2 + \frac{1}{6}\mathbf{T}^3 + \frac{1}{24}\mathbf{T}^4 + \cdots \\ &= 1 + \mathbf{T}_1 + (\mathbf{T}_2 + \frac{1}{2}\mathbf{T}_1^2) + (\mathbf{T}_3 + \mathbf{T}_1\mathbf{T}_2 + \frac{1}{6}\mathbf{T}_1^3) \\ &\quad + (\mathbf{T}_4 + \mathbf{T}_1\mathbf{T}_3 + \frac{1}{2}\mathbf{T}_2^2 + \frac{1}{2}\mathbf{T}_1^2\mathbf{T}_2 + \frac{1}{24}\mathbf{T}_1^4) + \cdots. \end{aligned} \tag{3.1.16}$$

Therefore, the CC ground state energy is given by the time-independent *Schrödinger equation*

$$\hat{\mathbf{H}}\Psi_{CC} = E_{CC}\Psi_{CC} \;\leftrightarrow\; E_{CC}\, e^{\mathbf{T}}\Phi_0 = \hat{\mathbf{H}} e^{\mathbf{T}}\Phi_0. \tag{3.1.17}$$

We multiply the equation (3.1.17) from the left with Φ_0 and integrate

$$\begin{aligned} E_{CC}\langle\Phi_0|e^{\mathbf{T}}\Phi_0\rangle &= \langle\Phi_0|\hat{\mathbf{H}}e^{\mathbf{T}}|\Phi_0\rangle \\ E_{CC} &= \langle\Phi_0|\hat{\mathbf{H}}|(1+\mathbf{T}_1+\mathbf{T}_2+\frac{1}{2}\mathbf{T}_1^2+\cdots)\Phi_0\rangle \\ &= \langle\Phi_0|\hat{\mathbf{H}}|\Phi_0\rangle+\langle\Phi_0|\hat{\mathbf{H}}|\mathbf{T}_1\Phi_0\rangle+\langle\Phi_0|\hat{\mathbf{H}}|\mathbf{T}_2\Phi_0\rangle+\frac{1}{2}\langle\Phi_0|\hat{\mathbf{H}}|\mathbf{T}_1^2\Phi_0\rangle+\cdots \\ &= E_0+\sum_{i,a}t_a^i\underbrace{\langle\Phi_0|\hat{\mathbf{H}}|\Phi_a^i\rangle}_{=0}+\sum_{\substack{i<j,\\a<b}}(t_{ab}^{ij}+t_a^it_b^j-t_b^it_a^j)\underbrace{\langle\Phi_0|\hat{\mathbf{H}}|\Phi_{ab}^{ij}\rangle}_{=(ia||jb)} \\ &\quad +0. \end{aligned} \tag{3.1.18}$$

Note that

$$\begin{aligned} \mathbf{T}_1^2\Phi_0 &= \sum_{i,j,a,b}t_a^it_b^j\langle\Phi_0|\hat{\mathbf{H}}|\Phi_{ab}^{ij}\rangle \\ &= \sum_{\substack{i<j,\\a<b}}t_a^it_b^j\langle\Phi_0|\hat{\mathbf{H}}|\Phi_{ab}^{ij}\rangle+\underbrace{\sum_{\substack{i>j,\\a<b}}t_a^it_b^j\langle\Phi_0|\hat{\mathbf{H}}|\Phi_{ba}^{ij}\rangle}_{\text{exchange labels } i \text{ and } j} \\ &= \sum_{\substack{i<j,\\a<b}}(t_a^it_b^j-t_b^it_a^j)\langle\Phi_0|\hat{\mathbf{H}}|\Phi_{ab}^{ij}\rangle. \end{aligned} \tag{3.1.19}$$

Equation (3.1.18) shows that if we know the amplitudes of single and double excited configurations, the CC energy is calculated. This fits to the *Full CI* picture, which shows that the Hatree-Fock determinant couples only with doubly excited configurations. In the following section, we are going to introduce how to calculate the amplitudes.

3.1.2.1. Truncated coupled cluster (CCSD and CC2)

Coupled cluster singles and doubles (CCSD) as a generally applicable CC method will be discussed. Its major approximation is that the cluster operator $\mathbf{T}$ is composed of only single and double excitation operators

$$\mathbf{T}=\mathbf{T}_1+\mathbf{T}_2, \tag{3.1.20}$$

which simplifies the equation (3.1.16) to

$$\begin{aligned} e^{\mathbf{T}} &= 1+\mathbf{T}_1+(\mathbf{T}_2+\frac{1}{2}\mathbf{T}_1^2)+(\mathbf{T}_1\mathbf{T}_2+\frac{1}{6}\mathbf{T}_1^3) \\ &\quad +(\frac{1}{2}\mathbf{T}_2^2+\frac{1}{2}\mathbf{T}_1^2\mathbf{T}_2+\frac{1}{24}\mathbf{T}_1^4)+\cdots . \end{aligned} \tag{3.1.21}$$

To calculate the single amplitudes, we multiply equation (3.1.17) from the left with a singly excited configuration Φ_m^e and integrate

$$\begin{aligned} E_{CCSD}\langle\Phi_e^m|e^{\mathbf{T}}\Phi_0\rangle &= \langle\Phi_e^m|\hat{\mathbf{H}}|\left[1+\mathbf{T}_1+(\mathbf{T}_2+\frac{1}{2}\mathbf{T}_1^2)+(\mathbf{T}_2\mathbf{T}_1+\frac{1}{6}\mathbf{T}_1^3+\cdots)\right]\Phi_0\rangle \\ E_{CCSD}\sum_{ia}t_a^i\langle\Phi_e^m|\Phi_a^i\rangle &= \langle\Phi_e^m|\hat{\mathbf{H}}|\Phi_0\rangle+\langle\Phi_e^m|\hat{\mathbf{H}}|\mathbf{T}_1\Phi_0\rangle+\langle\Phi_e^m|\hat{\mathbf{H}}|(\mathbf{T}_2+\frac{1}{2}\mathbf{T}_1^2)\Phi_0\rangle \\ &\quad +\langle\Phi_e^m|\hat{\mathbf{H}}|(\mathbf{T}_1\mathbf{T}_2+\frac{1}{6}\mathbf{T}_1^3)\Phi_0\rangle+0 \\ E_{CCSD}\,t_e^m &= 0+\sum_{i,a}t_a^i\langle\Phi_e^m|\hat{\mathbf{H}}|\Phi_a^i\rangle+\sum_{\substack{i<j,\\ a<b}}(t_{ab}^{ij}+\underbrace{t_a^it_b^j-t_b^it_a^j}_{\frac{1}{2}\mathbf{T}_1^2})\langle\Phi_e^m|\hat{\mathbf{H}}|\Phi_{ab}^{ij}\rangle+ \\ &\quad \sum_{\substack{i<j<k,\\ a<b<c}}\Big[\underbrace{2(t_a^it_{bc}^{jk}-t_b^it_{ac}^{jk}+t_c^it_{ab}^{jk})}_{\mathbf{T}_1\mathbf{T}_2}+\underbrace{\left(\begin{smallmatrix}t_a^it_b^jt_c^k-t_a^it_c^jt_b^k-t_b^it_a^jt_c^k\\ +t_c^it_a^jt_b^k+t_b^it_c^jt_a^k-t_c^it_b^jt_a^k\end{smallmatrix}\right)}_{\frac{1}{6}\mathbf{T}_1^3}\Big]\langle\Phi_e^m|\hat{\mathbf{H}}|\Phi_{abc}^{ijk}\rangle \\ &\quad +0. \end{aligned} \tag{3.1.22}$$

Similarly, for getting the double amplitudes, we multiply the equation (3.1.17) from the left with a doubly excited configuration Φ_{ef}^{mn} and integrate

$$
\begin{aligned}
E_{CCSD}\langle\Phi_{ef}^{mn}|e^{\mathbf{T}}\Phi_0\rangle &= \langle\Phi_{ef}^{mn}|\hat{\mathbf{H}}|\left[1+\mathbf{T}_1+(\mathbf{T}_2+\frac{1}{2}\mathbf{T}_1^2)+(\mathbf{T}_2\mathbf{T}_1+\frac{1}{6}\mathbf{T}_1^3)\right.\\
&\quad\left.+(\frac{1}{2}\mathbf{T}_2^2+\frac{1}{2}\mathbf{T}_1^2\mathbf{T}_2+\frac{1}{24}\mathbf{T}_1^4)+\cdots\right]\Phi_0\rangle\\
E_{CCSD}\sum_{\substack{i<j,\\ a<b}}(t_{ab}^{ij}+t_a^it_b^j-t_b^it_a^j)\langle\Phi_{ef}^{mn}|\Phi_{ab}^{ij}\rangle &= \langle\Phi_{ef}^{mn}|\hat{\mathbf{H}}|\Phi_0\rangle+\langle\Phi_{ef}^{mn}|\hat{\mathbf{H}}|\mathbf{T}_1\Phi_0\rangle\\
&\quad+\langle\Phi_{ef}^{mn}|\hat{\mathbf{H}}|(\mathbf{T}_2+\frac{1}{2}\mathbf{T}_1^2)\Phi_0\rangle+\langle\Phi_{ef}^{mn}|\hat{\mathbf{H}}|(\mathbf{T}_1\mathbf{T}_2+\frac{1}{6}\mathbf{T}_1^3)\Phi_0\rangle\\
&\quad+\langle\Phi_{ef}^{mn}|\hat{\mathbf{H}}|(\frac{1}{2}\mathbf{T}_2^2+\frac{1}{2}\mathbf{T}_1^2\mathbf{T}_2+\frac{1}{24}\mathbf{T}_1^4)\Phi_0\rangle+0\\
E_{CCSD}(t_{ef}^{mn}+t_e^mt_f^n-t_f^mt_e^n) &= 0+\sum_{i,a}t_a^i\langle\Phi_{ef}^{mn}|\hat{\mathbf{H}}|\Phi_a^i\rangle+\sum_{\substack{i<j,\\ a<b}}(t_{ab}^{ij}+\underbrace{t_a^it_b^j-t_b^it_a^j}_{\frac{1}{2}\mathbf{T}_1^2})\langle\Phi_{ef}^{mn}|\hat{\mathbf{H}}|\Phi_{ab}^{ij}\rangle+\\
&\quad\sum_{\substack{i<j<k,\\ a<b<c}}\left[\underbrace{2(t_a^it_{bc}^{jk}-t_b^it_{ac}^{jk}+t_c^it_{ab}^{jk})}_{\mathbf{T}_1\mathbf{T}_2}+\underbrace{\begin{pmatrix}t_a^it_b^jt_c^k-t_a^it_c^jt_b^k-t_b^it_a^jt_c^k\\ +t_c^it_a^jt_b^k+t_b^it_c^jt_a^k-t_c^it_b^jt_a^k\end{pmatrix}}_{\frac{1}{6}\mathbf{T}_1^3}\right]\langle\Phi_{ef}^{mn}|\hat{\mathbf{H}}|\Phi_{abc}^{ijk}\rangle+\\
&\quad\sum_{\substack{i<j<k<l,\\ a<b<c<d}}\left[\underbrace{\begin{pmatrix}t_{ab}^{ij}t_{cd}^{kl}-t_{ac}^{ij}t_{bd}^{kl}+t_{ac}^{ij}t_{db}^{kl}\\ -t_{ca}^{ij}t_{db}^{kl}+t_{ca}^{ij}t_{bd}^{kl}+t_{cd}^{ij}t_{ab}^{kl}\end{pmatrix}}_{\frac{1}{2}\mathbf{T}_2^2}+\underbrace{3\begin{pmatrix}t_{ab}^{ij}t_c^kt_d^l-t_{ab}^{ij}t_d^kt_c^l+t_{ac}^{ij}t_d^kt_b^l-t_{ca}^{ij}t_d^kt_b^l-t_{ac}^{ij}t_b^kt_d^l\\ +t_{ad}^{ij}t_b^kt_c^l-t_{ad}^{ij}t_c^kt_b^l+t_{da}^{ij}t_c^kt_b^l+t_{cd}^{ij}t_a^kt_b^l-t_{dc}^{ij}t_a^kt_b^l\end{pmatrix}}_{\frac{1}{2}\mathbf{T}_1^2\mathbf{T}_2}\right.\\
&\quad\left.+\underbrace{\begin{pmatrix}t_a^it_b^jt_c^kt_d^l-t_a^it_c^jt_b^kt_d^l-t_b^it_a^jt_c^kt_d^l+t_c^it_a^jt_b^kt_d^l+t_b^it_c^jt_a^kt_d^l-t_c^it_b^jt_a^kt_d^l\\ -t_a^it_b^jt_d^kt_c^l+t_a^it_c^jt_d^kt_b^l+t_b^it_a^jt_d^kt_c^l-t_c^it_a^jt_d^kt_b^l-t_b^it_c^jt_d^kt_a^l+t_c^it_b^jt_d^kt_a^l\\ +t_a^it_d^jt_b^kt_c^l-t_a^it_d^jt_c^kt_b^l-t_b^it_d^jt_a^kt_c^l+t_c^it_d^jt_a^kt_b^l+t_b^it_d^jt_c^kt_a^l-t_c^it_d^jt_b^kt_a^l\\ -t_a^it_a^jt_b^kt_c^l+t_a^it_a^jt_c^kt_b^l+t_a^it_b^jt_a^kt_c^l-t_a^it_c^jt_a^kt_b^l-t_a^it_b^jt_c^kt_a^l+t_a^it_c^jt_b^kt_a^l\end{pmatrix}}_{\frac{1}{24}\mathbf{T}_1^4}\right]\langle\Phi_{ef}^{mn}|\hat{\mathbf{H}}|\Phi_{abcd}^{ijkl}\rangle\\
&\quad+0. \qquad (3.1.23)
\end{aligned}
$$

Besides the single and double amplitudes appearing in the equations (3.1.22) and (3.1.23), there are several CI matrix elements, such as $\langle\Phi_e^m|\hat{\mathbf{H}}|\Phi_a^i\rangle$, $\langle\Phi_e^m|\hat{\mathbf{H}}|\Phi_{ab}^{ij}\rangle$, $\langle\Phi_e^m|\hat{\mathbf{H}}|\Phi_{abc}^{ijk}\rangle$, $\langle\Phi_{ef}^{mn}|\hat{\mathbf{H}}|\Phi_a^i\rangle$, $\langle\Phi_{ef}^{mn}|\hat{\mathbf{H}}|\Phi_{ab}^{ij}\rangle$, $\langle\Phi_{ef}^{mn}|\hat{\mathbf{H}}|\Phi_{abc}^{ijk}\rangle$ and $\langle\Phi_{ef}^{mn}|\hat{\mathbf{H}}|\Phi_{abcd}^{ijkl}\rangle$, needs to be calculate. They can be derived by the *Slate-Condon's rule*. With given initial guess, the single and double amplitudes can be calculated iteratively. Normally, for the CCSD method, the *second order Møller-Plesset perturbation theory* (MP2) wave function is taken as initial guess for the single and double amplitudes.
CCSD method with moderate basis sets works well for calculating ground and excited states. However, this method is still too expensive to perform on larger molecules. O. Christiansen *et al.* [63] proposed a simplified CCSD method called *approximated coupled cluster singles and doubles* (CC2) method. They take the

double amplitudes from MP2 results and keep them fixed while using equation (3.1.22) to calculate the single amplitudes iteratively. This approximation largely simplifies the computational cost for calculating double amplitudes which are less important factors for singly excited states. Since the singly excited states are the naturally easiest approachable excited states, they are of major interest for spectroscopic and opto-electronic applications. As a matter of fact, the CC2 method nowadays is often used as a standard method for excited states calculations of larger systems.

3.2. Model Hamiltonian method

3.2.1. Matrix elements

As mentioned in section 2.2, the *model Hamiltonian method* is a useful tool and has been widely applied for dimer systems.[25,28,29,30,31,64,65] In this section we are going to derive this method through an *ab initio* way.
As an example, we consider a dimer system consisting of two identical monomers A and B oriented in a specific symmetry. The ground state wavefunction Ψ_0 of the dimer system, neglecting any interaction between the monomers, is written as

$$\Psi_0 = |h_A \bar{h}_A h_B \bar{h}_B\rangle, \tag{3.2.1}$$

where the h_A ($\bar{h}_A$) and h_B ($\bar{h}_B$) are the HOMO of monomer A and B with alpha (beta) spin respectively. The four energetically lowest diabatic excited states in equation (2.2.1) are given by

$$\Psi_{A^*B} = \frac{1}{\sqrt{2}}(|h_A \bar{l}_A h_B \bar{h}_B\rangle + |l_A \bar{h}_A h_B \bar{h}_B\rangle), \tag{3.2.2}$$

$$\Psi_{AB^*} = \frac{1}{\sqrt{2}}(|h_A \bar{h}_A h_B \bar{l}_B\rangle + |h_A \bar{h}_A l_B \bar{h}_B\rangle), \tag{3.2.3}$$

$$\Psi_{A^+B^-} = \frac{1}{\sqrt{2}}(|h_A \bar{l}_B h_B \bar{h}_B\rangle + |l_B \bar{h}_A h_B \bar{h}_B\rangle), \tag{3.2.4}$$

$$\Psi_{A^-B^+} = \frac{1}{\sqrt{2}}(|h_A \bar{h}_A h_B \bar{l}_A\rangle + |h_A \bar{h}_A l_A \bar{h}_B\rangle), \tag{3.2.5}$$

where the l_A ($\bar{l_A}$) and l_B ($\bar{l_B}$) are the LUMO of monomer A and B with alpha (beta) spin respectively.

We take D_h as an example. By inserting equations (3.2.3) and (3.2.4) in equation (2.2.7) and assuming the MOs are orthonormalized, we get

$$\begin{aligned}
D_h &= \langle \Psi_{A^+B^-} | \hat{\mathbf{H}} | \Psi_{AB^*} \rangle \\
&= \frac{1}{2}\big[\langle h_A \bar{l_B} h_B \bar{h_B} | \hat{\mathbf{H}} | h_A \bar{h_A} h_B \bar{l_B} \rangle + \langle h_A \bar{l_B} h_B \bar{h_B} | \hat{\mathbf{H}} | h_A \bar{h_A} l_B \bar{h_B} \rangle \\
&\quad + \langle l_B \bar{h_A} h_B \bar{h_B} | \hat{\mathbf{H}} | h_A \bar{h_A} h_B \bar{l_B} \rangle + \langle l_B \bar{h_A} h_B \bar{h_B} | \hat{\mathbf{H}} | h_A \bar{h_A} l_B \bar{h_B} \rangle\big] \\
&= \frac{1}{2}\big[-(h_B|\hat{\mathbf{h}}|h_A) - (h_B h_B|h_B h_A) - (h_A h_A|h_B h_A) - (l_B l_B|h_B h_A) + (l_B h_A|h_B l_B) \\
&\quad + (l_B h_A|h_B l_B) \\
&\quad - (h_B|\hat{\mathbf{h}}|h_A) - (h_B h_B|h_B h_A) - (h_A h_A|h_B h_A) - (l_B l_B|h_B h_A) + (l_B h_A|h_B l_B) \\
&\quad + (l_B h_A|h_B l_B)\big] \\
&= -(h_B|\hat{\mathbf{F}}|h_A) + 2(l_B h_A|h_B l_B) - (l_B l_B|h_B h_A), \qquad (3.2.6)
\end{aligned}$$

where $\hat{\mathbf{F}}$ is the *Fock operator*. Similar operations can be done for D_e, V_{EC} and W (see appendix C for explicit derivations) which result in

$$D_e = (l_B|\hat{\mathbf{F}}|l_A) + 2(h_A l_B|l_A h_A) - (h_A h_A|l_B l_A), \qquad (3.2.7)$$

$$V_{\mathrm{EC}} = 2(l_A h_A|h_B l_B) - (l_A l_B|h_B h_A), \qquad (3.2.8)$$

$$W = 2(h_A l_B|l_A h_B) - (h_A h_B|l_B l_A). \qquad (3.2.9)$$

Here, we use another approximation for the HOMO (ψ_H) and HOMO-1 (ψ_{H-1}) of the dimer written as linear combination of the HOMOs (h_A and h_B) of the monomers

$$\psi_H \approx \frac{1}{\sqrt{2}}(h_A - h_B), \qquad \psi_{H-1} \approx \frac{1}{\sqrt{2}}(h_A + h_B), \qquad (3.2.10)$$

which results in

$$h_A \approx \frac{1}{\sqrt{2}}(\psi_H + \psi_{H-1}), \qquad h_B \approx \frac{1}{\sqrt{2}}(\psi_H - \psi_{H-1}). \qquad (3.2.11)$$

Thus the one electron integral part of D_h in equation (3.2.6) $(h_B|\hat{\mathbf{F}}|h_A)$ is given

as

$$\begin{aligned}(h_B|\hat{\mathbf{F}}|h_A) &\approx \frac{1}{2}\big(\psi_H - \psi_{H-1}|\hat{\mathbf{F}}|\psi_H + \psi_{H-1}\big) \\ &= \frac{1}{2}(\psi_H|\hat{\mathbf{F}}|\psi_H) - (\psi_{H-1}|\hat{\mathbf{F}}|\psi_{H-1}) \\ &= \frac{1}{2}(\varepsilon_H - \varepsilon_{H-1}). \end{aligned} \tag{3.2.12}$$

ε_H and ε_{H-1} are the orbital energies of the HOMO and HOMO-1 of the dimer respectively. A more precise way to present these integrals, which are given in terms of monomer orbitals, is to transform the monomer MOs into dimer MOs (for details about orbital transforming, see section 3.4.1)

$$h_A = \sum_i C_i^{h_A}\psi_i, \qquad h_B = \sum_j C_j^{h_B}\psi_j. \tag{3.2.13}$$

This leads to $(h_B|\hat{\mathbf{F}}|h_A)$ as a linear combination of all the dimer orbital energies

$$\begin{aligned}(h_B|\hat{\mathbf{F}}|h_A) &= \left(\sum_j C_j^{h_B}\psi_j|\hat{\mathbf{F}}|\sum_i C_i^{h_A}\psi_i\right) \\ &= \sum_i C_i^{h_A}\cdot C_i^{h_B}\cdot\varepsilon_i. \end{aligned} \tag{3.2.14}$$

In most cases, equation (3.2.12) is a very good approximation for equation (3.2.14). Similarly, the one electron integral part $(l_B|\hat{\mathbf{F}}|l_A)$ of the *electron transfer parameter* D_e can be written as

$$\begin{aligned}(l_B|\hat{\mathbf{F}}|l_A) &= \sum_i C_i^{l_B}\cdot C_i^{l_A}\cdot\varepsilon_i \\ &\approx \frac{1}{2}(\varepsilon_L - \varepsilon_{L+1}), \end{aligned} \tag{3.2.15}$$

The two electron integral parts of these coupling parameters have been written in the *chemists notation* [60] that they can be understood as interactions between transition densities. In the *exciton coupling parameter* V_{EC}, the first term $(l_A h_A|h_B l_B)$ is composed of a transition density corresponding to the LUMO to HOMO excitation on A $(l_A h_A)$ and a transition density HOMO to LUMO on B $(h_B l_B)$. Förster recognized that this integral can be approximated with spectroscopically available quantities. [32,66] For the second term $(l_A l_B|h_B h_A)$, it describes

the interaction between a transition density corresponding to the LUMO of A to LUMO of B transition ($l_A l_B$) and a transition density corresponding to HOMO of B to HOMO of A transition ($h_B h_A$). This is called as the *Dexter type transition*. [67]

Similarly, the two electron integrals in the expressions of D_e, D_h and W are also interpreted as transition density interactions. Those transition densities, which are connected to two monomers e. g. $l_A l_B$ and $h_B h_A$ etc., are strong functions to the distance between the two monomers. For aggregate systems, if the closest intermolecular distance is about 3 - 4 Å or even larger, these integrals are relatively small that we can use the following approximate equations for evaluating the coupling parameters

$$V_{\mathrm{EC}} \approx 2(l_A h_A | h_B l_B), \tag{3.2.16}$$

$$D_e \approx \frac{1}{2}(\varepsilon_{L+1} - \varepsilon_L), \tag{3.2.17}$$

$$D_h \approx \frac{1}{2}(\varepsilon_{H+1} - \varepsilon_H), \tag{3.2.18}$$

$$W \approx 0. \tag{3.2.19}$$

3.2.2. Solutions of the model Hamiltonian method

The coupling matrix tells that the four lowest excited states are given as the linear combination of these four diabatic excitation configurations (Ψ_{A^*B}, Ψ_{AB^*}, $\Psi_{A^+B^-}$ and $\Psi_{A^-B^+}$). Diagonalizing the coupling matrix leads to the energies of the four lowest adiabatic excited states. Here, we will diagonalize the matrix $\mathbf{H}$ in two steps, which helps to understand the physical meaning of the coupling matrix and the corresponding excited states wavefunctions.
Due to the assumed symmetry of the system (C_i or C_s etc.), we can introduce a unitary matrix $\mathbf{U}_1$ to block diagonalize the coupling matrix. $\mathbf{U}_1$ is given as

$$\mathbf{U}_1 = \frac{1}{\sqrt{2}} \begin{pmatrix} 1 & 0 & 1 & 0 \\ 1 & 0 & -1 & 0 \\ 0 & 1 & 0 & 1 \\ 0 & 1 & 0 & -1 \end{pmatrix}. \tag{3.2.20}$$

We get the new coupling matrix $\tilde{\mathbf{H}}$ from the unitary transformation

$$\tilde{\mathbf{H}} = \mathbf{U}_1^{\dagger} \cdot \mathbf{H} \cdot \mathbf{U}_1 = \begin{pmatrix} E_F + V_{\mathrm{EC}} & D_e + D_h & 0 & 0 \\ D_e + D_h & E_{CT} + W & 0 & 0 \\ 0 & 0 & E_F - V_{\mathrm{EC}} & D_e - D_h \\ 0 & 0 & D_e - D_h & E_{CT} - W \end{pmatrix}. \tag{3.2.21}$$

According to the equation (2.2.1), the original basis set (column vector) is transformed by the matrix $\mathbf{U}_1^{\dagger}$

$$\mathbf{U}_1^{\dagger} \cdot \begin{pmatrix} \langle \Psi_{A^*B}| \\ \langle \Psi_{AB^*}| \\ \langle \Psi_{A^+B^-}| \\ \langle \Psi_{A^-B^+}| \end{pmatrix} = \frac{1}{\sqrt{2}} \begin{pmatrix} \langle \Psi_{A^*B}| + \langle \Psi_{AB^*}| \\ \langle \Psi_{A^+B^-}| + \langle \Psi_{A^-B^+}| \\ \langle \Psi_{A^*B}| - \langle \Psi_{AB^*}| \\ \langle \Psi_{A^+B^-}| - \langle \Psi_{A^-B^+}| \end{pmatrix}. \tag{3.2.22}$$

The first term is a NE configuration which is the plus combination of two NE diabatic configurations and the second term is a CT configuration which is the plus combination of two CT diabatic configurations. Both of them belong to the plus symmetry representation. Their linear combinations give the expression of the adiabatic excited states which have the *plus* symmetry ($\Phi_{1(+)}$ and $\Phi_{2(+)}$). It also shows that the combined coupling parameter $D_e + D_h$ is responsible for the character mixing for the states $\Phi_{1(+)}$ and $\Phi_{2(+)}$, that the larger is $D_e + D_h$, the stronger is the character mixing for the two states.

The latter two configurations in the equation (3.2.22) belong to the *minus* symmetry and they are orthogonal to the first two configurations. They generate the two adiabatic states which have the *minus* symmetry ($\Phi_{1(-)}$ and $\Phi_{2(-)}$). Their characters are depending on the value of the combined coupling parameter $D_e - D_h$.

Since the $\tilde{\mathbf{H}}$ matrix is block diagonalized, each block matrix can be treated separately. Let's take the upper block matrix to proceed solving the wavefunction. In order to get the analytical solution, we use *Jacobi's Diagonalization*[68] for the 2×2 matrix. A unitary matrix $\mathbf{U}_2$

$$\begin{pmatrix} \cos\alpha & -\sin\alpha \\ \sin\alpha & \cos\alpha \end{pmatrix} \tag{3.2.23}$$

is supposed to diagonalize the matrix

$$\begin{pmatrix} E_F + V_{\mathrm{EC}} & D_e + D_h \\ D_e + D_h & E_{CT} + W \end{pmatrix}. \tag{3.2.24}$$

Therefore, the rotational angle α must satisfy the equation $\tan 2\alpha = \frac{2(D_e+D_h)}{E_F+V_{\mathrm{EC}}-E_{CT}-W}$. This directly gives the solution for the two plus symmetry states

$$|\Phi_{1(+)}\rangle = \frac{\cos\alpha}{\sqrt{2}}(|\Psi_{A^*B}\rangle + |\Psi_{AB^*}\rangle) + \frac{\sin\alpha}{\sqrt{2}}(|\Psi_{A^+B^-}\rangle + |\Psi_{A^-B^+}\rangle), \tag{3.2.25}$$

$$E_{1(+)} = \frac{E_F + V_{\mathrm{EC}} + E_{CT} + W}{2} - \sqrt{(D_e + D_h)^2 + \frac{(E_F + V_{\mathrm{EC}} - E_{CT} - W)^2}{4}}, \tag{3.2.26}$$

$$|\Phi_{2(+)}\rangle = -\frac{\sin\alpha}{\sqrt{2}}(|\Psi_{A^*B}\rangle + |\Psi_{AB^*}\rangle) + \frac{\cos\alpha}{\sqrt{2}}(|\Psi_{A^+B^-}\rangle + |\Psi_{A^-B^+}\rangle), \tag{3.2.27}$$

$$E_{2(+)} = \frac{E_F + V_{\mathrm{EC}} + E_{CT} + W}{2} + \sqrt{(D_e + D_h)^2 + \frac{(E_F + V_{\mathrm{EC}} - E_{CT} - W)^2}{4}}. \tag{3.2.28}$$

For the two minus symmetry states, they can be solved in the similar way

$$|\Phi_{1(-)}\rangle = \frac{\cos\beta}{\sqrt{2}}(|\Psi_{A^*B}\rangle - |\Psi_{AB^*}\rangle) + \frac{\sin\beta}{\sqrt{2}}(|\Psi_{A^+B^-}\rangle - |\Psi_{A^-B^+}\rangle), \tag{3.2.29}$$

$$E_{1(-)} = \frac{E_F - V_{\mathrm{EC}} + E_{CT} - W}{2} - \sqrt{(D_e - D_h)^2 + \frac{(E_F - V_{\mathrm{EC}} - E_{CT} + W)^2}{4}}, \tag{3.2.30}$$

$$|\Phi_{2(-)}\rangle = -\frac{\sin\beta}{\sqrt{2}}(|\Psi_{A^*B}\rangle - |\Psi_{AB^*}\rangle) + \frac{\cos\beta}{\sqrt{2}}(|\Psi_{A^+B^-}\rangle - |\Psi_{A^-B^+}\rangle), \tag{3.2.31}$$

$$E_{2(-)} = \frac{E_F - V_{\mathrm{EC}} + E_{CT} - W}{2} + \sqrt{(D_e - D_h)^2 + \frac{(E_F - V_{\mathrm{EC}} - E_{CT} + W)^2}{4}}, \tag{3.2.32}$$

where the angle β should satisfy the equation $\tan 2\beta = \frac{2(D_e-D_h)}{E_F-V_{\mathrm{EC}}-E_{CT}+W}$.

3.3. ALGORITHMS FOR EVALUATING TRANSITION DENSITY

3.3.1. TRANSITION DENSITY AND TRANSITION DENSITY MATRIX

For a ground state Φ_0

$$\Phi_0 = |\hat{\chi}_1\hat{\chi}_2\cdots\hat{\chi}_n\rangle, \tag{3.3.1}$$

and its resulting excited state Φ_{ex}

$$\Phi_{ex} = |\chi_1\chi_2\cdots\chi_n\rangle, \tag{3.3.2}$$

a first order transition density P[69] is given as

$$\begin{aligned} P &= n\int d\sigma_1\cdots d\sigma_n d\mathbf{r}_1\cdots d\mathbf{r}_n\Phi_0^*\Phi_{ex} \\ &= \sum_{k,l}^{n}(-1)^{k+l}\int\hat{\chi}_k^*\chi_l d\sigma_1\cdot\underbrace{\langle\hat{\chi}_1\hat{\chi}_2\cdots\hat{\chi}_n|}_{no\ \hat{\chi}_k}\underbrace{|\chi_1\chi_2\cdots\chi_n\rangle}_{no\ \chi_l} \\ &= \sum_{k,l}^{n}(-1)^{k+l}\cdot T_{kl}\int\hat{\chi}_k^*\chi_l d\sigma_1. \end{aligned} \tag{3.3.3}$$

$d\sigma_i$ and $d\mathbf{r}_i$ are the spin and spatial coordinates for electron 'i'. T_{kl} is the transition density matrix. For the case if the two sets of MOs for ground and excited states are orthogonal to each other, $\mathbf{T}$ is the unit matrix[60]

$$T_{ij} = \delta_{ij}. \tag{3.3.4}$$

The following sections will discuss how to calculate the matrix $\mathbf{T}$ if nonorthogonal MOs are used. The nonorthogonal MOs give rise to the non-unit transition density matrix, by taking the definition from equation (4.4.16)

$$T_{kl} = \underbrace{\langle\hat{\chi}_1\hat{\chi}_2\cdots\hat{\chi}_n|}_{no\ \hat{\chi}_k}\underbrace{|\chi_1\chi_2\cdots\chi_n\rangle}_{no\ \chi_l}. \tag{3.3.5}$$

Matrix $\mathbf{T}$ is related the overlap matrix $\mathbf{S}$ between the ground and excited states

in terms of MOs

$$\begin{pmatrix} S_{1,1} & \cdots & S_{1,n} \\ \vdots & \ddots & \vdots \\ S_{n,1} & \cdots & S_{n,n} \end{pmatrix} \equiv \begin{pmatrix} \langle \hat{\chi}_1 | \chi_1 \rangle & \cdots & \langle \hat{\chi}_1 | \chi_n \rangle \\ \vdots & \ddots & \vdots \\ \langle \hat{\chi}_n | \chi_1 \rangle & \cdots & \langle \hat{\chi}_n | \chi_n \rangle \end{pmatrix}. \tag{3.3.6}$$

Then T_{kl} equals the cofactor of the matrix element $\langle \hat{\chi}_k | \chi_l \rangle$ of the matrix $\mathbf{S}$

$$T_{kl} = \det \begin{pmatrix} S_{1,1} & \cdots & S_{1,l-1} & S_{1,l+1} & \cdots & S_{1,n} \\ \vdots & \ddots & \vdots & \vdots & \ddots & \vdots \\ S_{k-1,1} & \cdots & S_{k-1,l-1} & S_{k-1,l+1} & \cdots & S_{k-1,n} \\ S_{k+1,1} & \cdots & S_{k+1,l-1} & S_{k+1,l+1} & \cdots & S_{k+1,n} \\ \vdots & \ddots & \vdots & \vdots & \ddots & \vdots \\ S_{n,1} & \cdots & S_{n,l-1} & S_{n,l+1} & \cdots & S_{n,n} \end{pmatrix}. \tag{3.3.7}$$

Therefore, the matrix $\mathbf{T}$ is just the adjugate matrix of the matrix $\mathbf{S}$

$$\mathbf{T} = \mathbf{S}^{adj}. \tag{3.3.8}$$

When matrix $\mathbf{S}$ is non-singular, the adjugate matrix $\mathbf{S}^{adj}$ is calculated in the following way

$$\mathbf{S}^{adj} = \det \mathbf{S} \cdot \mathbf{S}^{-1}. \tag{3.3.9}$$

If $\mathbf{S}$ is a singular matrix, $\mathbf{S}$ is not invertible. To calculate the $\mathbf{S}^{adj}$ becomes more tricky. A modified Gauss-Elimination algorithm was proposed by Prof. Dr. M. Dobrowolski (Department of Mathematics, University of Würzburg, in April, 2009), which can calculate the $\mathbf{S}^{adj}$ in any possible situation.

3.3.2. Modified Gauss-Elimination algorithm

By a standard Gauss-Elimination (GE) process for a matrix $\mathbf{S}$, the resulting upper triangular matrix $\mathbf{U}$ satisfies

$$\mathbf{U} = \mathbf{G} \cdot \mathbf{S}, \tag{3.3.10}$$

where the matrix $\mathbf{G}$ is the elimination matrix and has a unit determinant. Thus, the determinant of matrix $\mathbf{S}$ equals the one of matrix $\mathbf{U}$

$$\det \mathbf{S} = \det \mathbf{U} = (-1)^{\alpha} \prod_{i=1}^{n} U_{ii}. \tag{3.3.11}$$

α is the total permutation number after the full pivot in the GE process. With the pivot, one immediately gets an integer d such that the last d rows of matrix $\mathbf{U}$ are zeros.
Based on different values of d, three cases are distinguished:

$d = 0$

Matrix $\mathbf{S}$ is a non-singular matrix, that it is invertible. Thus, the adjugate matrix can be calculated with equations (3.3.9) and (3.3.11)

$$\mathbf{S}^{adj} = (-1)^{\alpha} \prod_{i=1}^{n} U_{ii} \cdot \mathbf{S}^{-1}. \tag{3.3.12}$$

$d = 1$

Matrix $\mathbf{S}$ is not invertible, that the equation (3.3.12) is not usable directly. Therefore, we are trying to built a new invertible matrix $\mathbf{S}_t$ with a variable matrix element t. Its adjugate matrix is a function of t. When t approaches 0, we get the exact adjugate matrix of the singular matrix $\mathbf{S}$.
First, we create a new invertible matrix $\mathbf{U}_t$ by only substituting the last matrix element U_{nn} in the triangular matrix $\mathbf{U}$ with a non-zero variable t

$$\mathbf{U}_t = \begin{pmatrix} U_{1,1} & \cdots & U_{1,n-1} & U_{1,n} \\ \vdots & \ddots & \vdots & \vdots \\ 0 & \cdots & U_{n-1,n-1} & U_{n-1,n} \\ 0 & \cdots & 0 & t \end{pmatrix}. \tag{3.3.13}$$

In order to satisfy the equation $\mathbf{U}_t \cdot \mathbf{S}_t^{-1} = \mathbf{G}$, the matrix $\mathbf{S}_t^{-1}$ can be written in the following form

$$\mathbf{S}_t^{-1} = \mathbf{Y} + t^{-1} \cdot \mathbf{Z}. \tag{3.3.14}$$

Just by taking the matrix $\mathbf{Y}$ with the form

$$\mathbf{Y} = \begin{pmatrix} S_{1,1}^{-1} & \cdots & S_{1,n-1}^{-1} & S_{1,n}^{-1} \\ \vdots & \ddots & \vdots & \vdots \\ S_{n-1,1}^{-1} & \cdots & S_{n-1,n-1}^{-1} & S_{n-1,n}^{-1} \\ 0 & \cdots & 0 & 0 \end{pmatrix}, \tag{3.3.15}$$

and matrix $\mathbf{Z}$ satisfies the equation

$$\mathbf{G}' = \mathbf{U}_{t=1}^{-1} \cdot \mathbf{Z}. \tag{3.3.16}$$

where matrix $\mathbf{G}'$ takes the form

$$\mathbf{G}' = \begin{pmatrix} 0 & \cdots & 0 & 0 \\ \vdots & \ddots & \vdots & \vdots \\ 0 & \cdots & 0 & 0 \\ G_{n,1} & \cdots & G_{n,n-1}^{-1} & G_{n,n}^{-1} \end{pmatrix}. \tag{3.3.17}$$

Therefore, we get the adjugate matrix of $\mathbf{S}$

$$\mathbf{S}^{adj} = (-1)^{\alpha} \prod_{i=1}^{n-1} U_{ii} \cdot \lim_{t\to 0} t(\mathbf{Y} + t^{-1}\mathbf{Z}) = (-1)^{\alpha} \prod_{i=1}^{n-1} U_{ii} \cdot \mathbf{Z}. \tag{3.3.18}$$

$d > 1$

For such case, all cofactors of the matrix $\mathbf{S}$ are 0, because each matrix of cofactor will have at least one zero line. Therefore, the adjugate matrix of $\mathbf{S}$ is a trivial zero matrix

$$\mathbf{S}^{adj} = \mathbf{0}. \tag{3.3.19}$$

3.4. Character analysis of excited states on delocalized picture

3.4.1. Based on the CIS type wavefunction

In the CIS approach, the adiabatic excited states for a system that is described with a closed shell Slater determinant Ψ_0 can be written as

$$\Psi_{CIS} = \sum_{a,i} C_{ai}^{d} \hat{E}_{ai} \Phi_0. \tag{3.4.1}$$

Here the superscript d indicates that the canonical (delocalized) MOs are used, C_{ai}^{d} is the CI (singles) coefficient for the excitation of the electrons from the spatial orbitals i to a, and $\hat{E}_{ai}$ is the spin-adapted single excitation operator rep-

resenting an excitation of one electron from the occupied orbital i to the virtual orbital a. The latter is defined by

$$\hat{E}_{ai} = \frac{1}{\sqrt{2}} \left(\hat{a}_i^\dagger \hat{a}_a + \hat{a}_{\bar{i}}^\dagger \hat{a}_{\bar{a}} \right), \tag{3.4.2}$$

where $\hat{a}_{\bar{a}}^\dagger$ ($\hat{a}_i$) represents the common creation (annihilation) operator of the spin orbital and the over-bar indicates β spin orbital.

Consider a dimer system which is composed of two monomers A and B. According to Peterlenz's definition of CT and NE states,[23] an analysis of the character of the CIS wave function requires a definition of the localized MOs. We have chosen to take the canonical MOs of the monomers for this purpose. In order to retain a proper definition of the wave function the localized MOs $\tilde{\psi}^l$ are orthonormalized using Löwdin's method[70,71]. This leads to an orthonormal basis set where each orbital is essentially localized on either one or the other monomer.

With these definitions, the delocalized MOs $\vec{\psi}^d$ can be represented from the localized orbitals by

$$\vec{\psi}^d = \mathbf{U} \cdot \vec{\tilde{\psi}}^l, \tag{3.4.3}$$

where $\mathbf{U}$ is a unitary matrix. It includes two-step operations of an orbital transformation ($\mathbf{T}$) and an orthogonalization ($\mathbf{D}$)

$$\mathbf{U} = \mathbf{D} \cdot \mathbf{T}. \tag{3.4.4}$$

Matrix $\mathbf{T}$ transform the delocalized MOs to localized MOs

$$\psi_m^d = \sum_p T_{m,p} \psi_p^l. \tag{3.4.5}$$

Its inverse matrix $\mathbf{T}^{-1}$ transforms the localized MOs back to delocalized MOs

$$\psi_p^l = \sum_m T_{p,m}^{-1} \psi_m^d. \tag{3.4.6}$$

Considering the orthogonality condition for delocalized MOs, we multiply equation (3.4.6) with $\psi_n^{d^*}$ from the left and integrate over the space

$$\begin{aligned} \langle \psi_n^d | \psi_p^l \rangle &= \sum_m T_{p,m}^{-1} \langle \psi_n^d | \psi_m^d \rangle \\ O_{n,p} &= \sum_m T_{m,p}^{-1} \cdot \delta_{n,m} \\ O_{n,p} &= T_{p,n}^{-1}. \end{aligned} \tag{3.4.7}$$

$O_{n,p}$ is the overlap between the delocalized and localized MOs. Since **O** and **T** are unitary matrices, we get the matrix **T**

$$\mathbf{T} = \mathbf{O} \tag{3.4.8}$$

Matrix **D** represents a standard Löwdin's orthogonalization

$$\mathbf{D} = \mathbf{S}^{-\frac{1}{2}} \tag{3.4.9}$$

where the matrix **S** is the overlap matrix of the atomic basis sets.
Thus, the excited wave function in terms of the localized orbitals can be represented by

$$\Psi_{CIS} = \sum_{ab} \sum_{ij} C_{ai}^d U_{ba} U_{ji}^\dagger \hat{E}_{bj} \Psi_0 = \sum_{bj} C_{bj}^l \hat{E}_{bj} \Psi_0, \tag{3.4.10}$$

where the CI coefficients in the delocalized basis are given by

$$C_{bj}^l = \sum_{ai} U_{ba} C_{ai}^d U_{ji}^\dagger. \tag{3.4.11}$$

As the localized orbitals can be unambiguously connected to the monomers, any diabatic configuration in the last equation can be designated as a pure CT or NE configuration and the CT contribution of the excited state is given by

$$P_{CT} = \frac{\sum (C_{CT}^l)^2}{\sum (C^l)^2}. \tag{3.4.12}$$

This analysis method works well for aggregate systems, as long as the monomer orbitals are well defined. However, the present method can not be easily applied for single molecules. For that purpose, one needs a clear cut definition for different domains in the monomer. A possible solution would be using the *natural atomic orbitals* (NAO) that form the domain basis set. This may be of interest

for large polyers or bio-molecules.

3.4.2. Based on the spatial overlap

The most widely used method for calculating excited state properties of medium or large size molecules is *time-dependent density functional theory* (TDDFT). However, it is now well-known that it underestimates the excitation energies of CT states substantially.[72,73,74,75] As mentioned before (section 2.3), *long range corrected* (LC) functionals have largely solved this problem. Tozer *et al.* established a method that evaluates the amount of CT character in an excited state.[76,77] They found the spatial overlap of the orbitals involved in the excitations correlates with the excitation energy error of an excited state. The spatial overlap between the occupied orbital φ_i and the virtual orbital φ_a is given as

$$O_{i,a} = \int |\varphi_i(\mathbf{r})| \cdot |\varphi_a(\mathbf{r})| d\mathbf{r}. \tag{3.4.13}$$

The moduli of the orbitals make sure that the integral would not be trivially zero. This integral is about one if the electron, before and after excitation, is located in the same spatial region. This 'unmoved' behavior just fits to the idea of an NE excitation. The NE character of an adiabatic excited state Λ, which is given as a linear combination of these single excitation configurations, can be written as

$$\Lambda = \frac{\sum_{i,a} \kappa_{i,a}^2 O_{i,a}}{\sum_{i,a} \kappa_{i,a}^2}, \tag{3.4.14}$$

where the $\kappa_{i,a}$ is the coefficient of the configuration Φ_a^i. This method gives a possibility to analyze the character of an excited state for a monomer system. Based on the idea, each excitation configuration has a clear ratio of each character. Compared to Kasha's definition[78], this method is more like analyzing the character of an excitation process that any change compared with the ground state wavefunction is taken as CT character.

For an extreme case, a dimer system consists of two monomers A and B with infinite distance. The lowest monomer excited state would have the same wavefunction as the lowest dimer excited state. In the Tozer's definition, the lowest monomer excited state is not necessarily a pure NE state. Thus, the corresponding dimer excited state should not be a pure NE state as well. However, in the Peterlenz's definition, the first dimer excited state is expected possessing pure

NE character. This shows that the Tozer's definition does not necessary satisfy the Peterlenz's definition for aggregates.

Chapter 4

Results and Discussion

4.1. Method validation for valence excited states calculation of dye aggregates

4.1.1. Introduction

In the weak coupling case [32,79] the rate for the resonance energy transfer (RET) process is given by Fermi's golden rule [80,81]

$$k_{\mathrm{EET}} = \frac{2\pi}{\hbar}|V_{\mathrm{EC}}|^2 J_{\mathrm{EET}} \tag{4.1.1}$$

Here J_{EET} represents the *Franck-Condon* weighted density i. e. the overlap of the bands of the donor fluorescence and acceptor absorption spectra. V_{EC} is the electronic coupling matrix element between the two neutral states indicated in Fig. 2.1 (left hand side). It is the central term in the EET as it represents the electronic interaction that gives rise to the process.
The involved states in EET are the so-called *neutral excited states* which are called *Frenkel excitons* in the context of solid state physics (Fig. 2.1 left hand side). The coupling between both NE states which is central for the energy transfer process can be approximated by the well-known Förster formula [32,66]

$$V_{\mathrm{EC}} = \frac{\vec{D}_A\vec{D}_B}{R_{AB}^3} - 3\frac{(\vec{D}_A\vec{R}_{AB})(\vec{R}_{AB}\vec{D}_B)}{R_{AB}^5}, \tag{4.1.2}$$

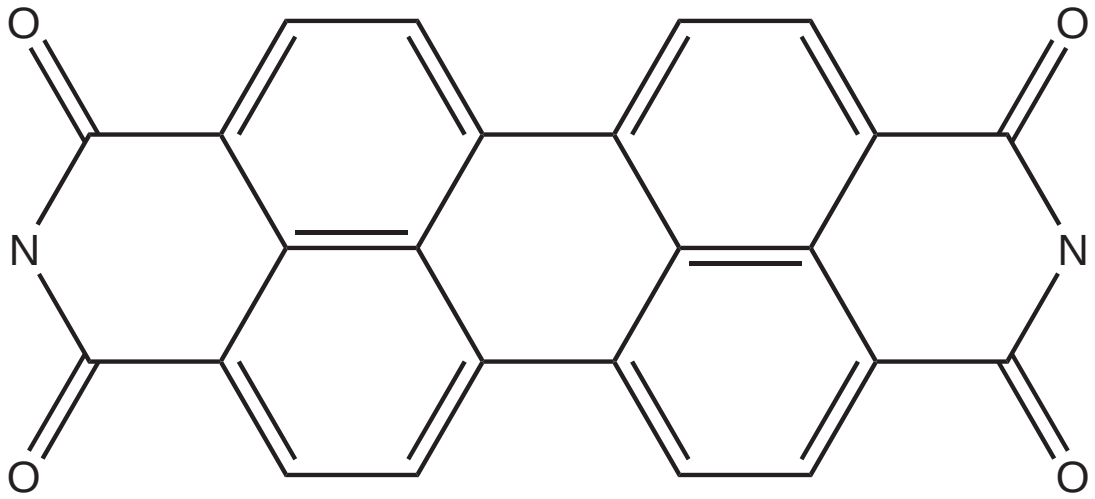

Figure 4.1.: The planar perylene tetracarboxylic bisimide (PBI) moiety.

where $\vec{D}_A$ and $\vec{D}_B$ are the transition dipole moments of both monomers and $\vec{R}_{AB}$ is the vector between A and B. As can be seen from this equation the mutual orientation of the monomers in the aggregate is crucial for the efficiency of the EET.

Besides these NE states, the transfer properties can also be influenced by so-called *charge-transfer* (CT) states (Fig. 2.1 right hand side). They arise from electron-transfer processes between the monomers. Pure CT states possess small to vanishing transition dipole moments, causing small coupling matrix elements within the Förster approach. If such states are populated after excitation they act as a trap in the energy transfer process. Consequently, a reliable description of the EET must comprise both kinds of states and their mutual interactions.

The potential importance of CT states for the spectral properties of 3,4,9,10-perylene tetracarboxylic dianhydride (PTCDA) and their possible role as exciton traps was pointed out by Bulovic *et al.*,[12,82] Gregg and coworkers,[83,84,85,86] Gomez *et al.*,[87] Scholz *et al.*,[30] and Hoffmann *et al.*[64] In the latter work, similar conclusions were also drawn for perylene tetracarboxylic bisimide (PBI) (Fig. 4.1). However, these indications are not unambiguous since they are based on empirical Hamiltonians for which the necessary parameters were fitted with respect to the experimental spectra. Furthermore, recent experimental investigations did not support an influence of charge-transfer states on the absorption spectra of PBI aggregates.[21,88,89]

Computing the necessary parameters by quantum-chemical methods leads to a

less ambiguous picture of the EET in aggregates, but naturally depends on the accuracy of the underlying quantum chemical approaches. Indeed, computing the coupling parameter V_{EC} from the transition densities of the isolated chromophores[46,90,91] a strong dependence on the underlying method is found. For PBI aggregates Munoz-Losa *et al.*[90] found that TD-DFT employing the well known B3LYP functional (TD-B3LYP) provided 20 to 40 % smaller coupling parameters than more sophisticated treatments as the symmetry adapted cluster-configuration interaction (SAC-CI) approach or the complete active space self consistent field (CASSCF) treatment. This finding agrees well with the calculations of Fückel *et al.*,[46] who found for a PBI dyad that TD-B3LYP predicts 15 % smaller coupling constants than the approximate coupled-cluster singles-and-doubles (CC2) model. The configuration interaction singles excitation (CIS) method which is closely related to time dependent Hartree-Fock (TD-HF) on the other hand predicts values which are about 20 % larger[90] than the values obtained from the more sophisticated treatments. The differences also seem to be quite general with respect to the molecular system since for rubrene similar trends were found by Gao *et al.*[92] They are also observed if V_{EC} is computed by a supermolecule approach.[2,22,93] For PBI dimers gas phase TD-HF gave a coupling constant V_{EC} of 1216 cm^{-1} (0.151 eV) while 875 cm^{-1} (0.108 eV) was computed with TD-B3LYP.

This difference might result from the well-known drawbacks of TD-HF and TD-B3LYP. While TD-HF tends to overestimate the excitation energies of CT states even more than their NE counterparts, the opposite holds true for most TD-DFT approaches. As a consequence TD-HF or related approaches predict the first CT states of PBI dimers to lie about 3 eV above the NE states while TD-B3LYP predicts that the two lowest excited states have CT character.[91,94] This difference is most probably owing to the poor performance of TD-B3LYP for low lying excitations in spatially separated systems which is caused by the self-interaction error.[72,73,74,75] The different energy order of these methods was also mentioned by Clark *et al.*[95] and Guthmuller *et al.*[93] Note that V_{EC} was obtained in all cases from the two electronic states with NE character.

A further test of the approaches was performed by Zhao *et al.*[91] in a work that investigates the crystallochromic solid state effect of several PBI dyes.[96] They computed the vertical excitation energies for twenty different crystal structures. For that purpose π-stacked PBI dimers were taken from the crystal structure. Their excitation energies were calculated and corrected for solid state effects.

A comparison of the theoretical results with the experimental absorption maxima showed that TD-HF perfectly reproduces the experimental changes of the excitation energies as a function of the crystal structure while TD-B3LYP failed completely since it predicts blue shifts of the absorption maxima for substances that show red shifts and vice versa. As the absorption maxima of the PBI derivatives are assigned to transitions to the NE states, this result was not expected because TD-B3LYP is generally known to describe excitations to NE states quite accurately, typically TD-B3LYP excitation energies are more reliable than those from TD-HF calculations.

As we will show in the present section, an explanation for the failure of TD-DFT approaches is that the employed states represent a mixing of the NE and the CT diabatic configurations. In this case wrong energetic order of both kinds of states leads to wrong energetic positions and characters of the low lying excited states. To test this assumption, different quantum chemical approaches are used to compute the energy ordering and the character of the states of PBI dimers. The most accurate method employed in the present section is the spin-component scaling modification of CC2 (SCS-CC2).[97] This method was shown to describe the energy position of NE and CT states with remarkably small errors typically below 0.15 eV. Thus, SCS-CC2 is clearly much more reliable than TD-HF and any TD-DFT approach. Due to its accuracy SCS-CC2 provides a reliable picture about the energy order and the characters of the involved states. But this method has limits as well, e. g. it cannot reliably describe doubly excited states. However, more accurate methods, which overcome this limits, are by far too expensive for such large systems like PBI dimers. Therefore, SCS-CC2 serves as a reference to check the quality of less sophisticated linear response theories. In this section we investigate pure GGA functional like BLYP and PBE and hybrid functions like B3LYP, BHLYP and PBE0. Within the description of charge transfer (CT) states, these DFT functionals are well known to show a wrong behavior of the exchange potentials, which should decay as $-r^{-1}$ at large distances.[72,73,74,75] This behavior is approximately correct in LC functionals, so that an improved description of CT states should result. To test the outcome of such an LC functional for the present problem, we chose the popular CAM-B3LYP functional as an example. This functional is a combination of the hybrid functional B3LYP with a long-range correction for the two-electron operator ($1/r_{12}$), which contains three additional parameters.[59] Therefore, depending on r_{12} the mixture of exact Hartree-Fock and DFT exchange varies for different regions

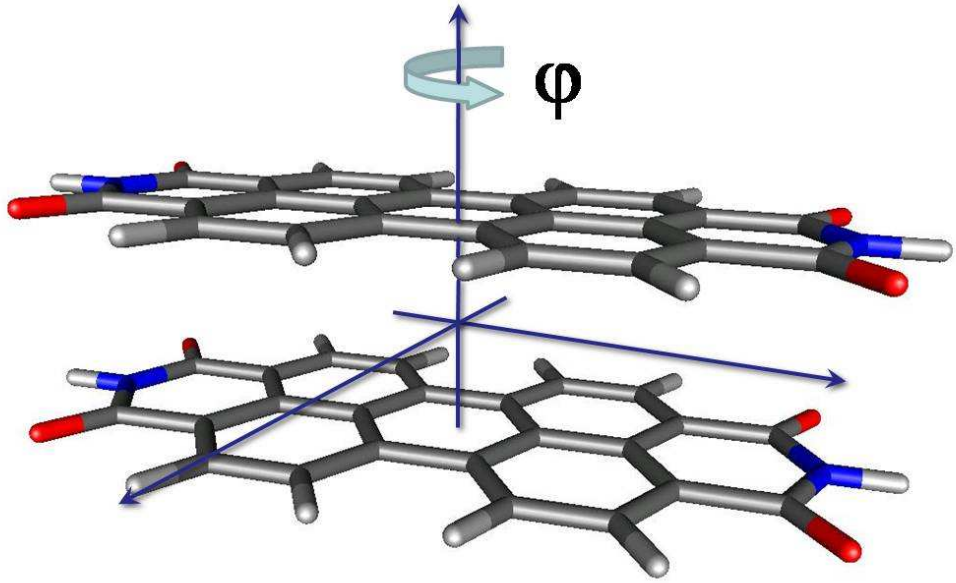

Figure 4.2.: Torsional motion of the dimer system around the angle φ.

of the molecule. In the literature it was shown that CAM-B3LYP can describe charge transfer states quite accurately for a wide range of molecules.[76,98,99]

4.1.2. Calculation procedure

The computations are performed for the PBI dimer as a model system for dye aggregates. To investigate variations in energy order and characters of the involved states as a function of the relative orientation of both monomers, potential energy curves are computed, which describe a torsion of the two monomers with respect to each other (Fig. 4.2). Most of the calculations were performed with the Turbomole 5.9 package[100] using the TZV[101] basis set for the hydrogen atoms and the TZVP[97] basis at non-hydrogen atoms {TZV(P)}. Ground state energies were calculated with BLYP,[49,50,51] PBE,[49,50,54,55] PBE0,[49,50,54,55,58] BHLYP,[49,50,51,52,53] B3LYP,[49,50,51,53,56,57] CAM-B3LYP[59] and SCS-CC2.[63,97,102,103] In order to speed up computational time, BLYP, PBE and SCS-CC2 were used combined with the resolution of identity (RI) approximation[62,104,105] with

the TZVP auxiliary basis sets.[101] The CAM-B3LYP calculations were performed with the Gaussian09[106] program. For this method the 6-311G** [107,108,109,110] basis set was employed.

Dispersive interactions are crucial for the ground and excited states of dimers of large π-conjugated molecules. To take them into account we have included Grimme's empirical dispersion correction[111] and computed ground state energies at the dispersion corrected BLYP (BLYP-D) level. As shown previously the binding energies resulting from BLYP-D/TZV(P) and SCS MP2/QZVPP[112] computations are quite similar.[94]

Here, the PBI monomer structure from the work of Zhao *et al.*[91] was used. This structure was optimized at the BLYP-D/TZV(P) level of theory. The dimer structures were built up in a π-stacked face-to-face orientation with an intermolecular distance of 3.4 Å. For the potential energy curves shown in this work the torsion angle about the stacking axis was varied from 0° to 90°.

Excited state calculations were performed with SCS-CC2,[97] TD DFT,[113,114] and TD-HF. While SCS-CC2 accounts for dispersion effects this is not the case for the other methods. Hence, potential energy curves of the excited states were approximated by adding the excitation energies of the considered method to the BLYP-D ground state energy.[91] In the following these methods will be designated as TD-DFT-D and TD-HF-D. It has to be mentioned that the convergency of the wavefunction for PBI dimers represents a big problem due to the small HOMO to LUMO gap. For all the calculations presented here it was only possible to achieve convergency, if HF wavefunctions were used as starting guess. While this worked for the methods presented here, it fails for various other functionals, especially long-range corrected ones.

It was already pointed out that the electronic states represent mixing of NE and CT diabatic configurations. In the two state approximation the wave functions of the two lowest lying adiabatic states (ψ_1, ψ_2) of $^1B_1$ and $^1B_2$ symmetry can be written as linear combination of a NE and a zwitterionic configuration (Fig. 2.1)

$$\psi_1 = a\phi_{\mathrm{NE}} + b\phi_{\mathrm{CT}}, \quad \psi_2 = c\phi_{\mathrm{NE}} + d\phi_{\mathrm{CT}}. \tag{4.1.3}$$

Their corresponding transition dipole moments μ_1 and μ_2 are given as

$$\mu_1 = \langle\psi_0|e\vec{\mathbf{r}}|\psi_1\rangle, \quad \mu_2 = \langle\psi_0|e\vec{\mathbf{r}}|\psi_2\rangle, \tag{4.1.4}$$

where $e\vec{\mathbf{r}}$ is the dipole moment operator, ψ_0 is the ground state wavefunction and ψ_1 and ψ_2 are the adiabatic excited states. Also, considering the orthonormalization condition for the excited states ψ_1 and ψ_2, the following equations are valid

$$\begin{cases} \langle\psi_1|\psi_1\rangle = 1 \\ \langle\psi_2|\psi_2\rangle = 1 \\ \langle\psi_1|\psi_2\rangle = 0 \end{cases} \rightarrow \begin{cases} a^2+b^2 = 1 \\ c^2+d^2 = 1 \\ ac+bd = 0 \end{cases} . \tag{4.1.5}$$

With the assumption that the transition dipole moment of the CT configuration μ_{CT} is negligible

$$\mu_{\mathrm{CT}} = e\langle\psi_0|\vec{\mathbf{r}}|\phi_{\mathrm{CT}}\rangle = 0, \tag{4.1.6}$$

and the NE configuration has a transition dipole moment μ_{NE}

$$\mu_{\mathrm{NE}} = e\langle\psi_0|\vec{\mathbf{r}}|\phi_{\mathrm{NE}}\rangle. \tag{4.1.7}$$

By inserting equation (4.1.3) into equation (4.1.4) and using equations (4.1.7) and (4.1.6), we get

$$\begin{aligned} \mu_1 &= e\langle\psi_0|\vec{\mathbf{r}}|a\phi_{\mathrm{NE}}+b\phi_{\mathrm{CT}}\rangle \\ &= e\langle\psi_0|\vec{\mathbf{r}}|a\phi_{\mathrm{NE}}\rangle = a\mu_{\mathrm{NE}}, \end{aligned} \tag{4.1.8}$$

and

$$\begin{aligned} \mu_2 &= e\langle\psi_0|\vec{\mathbf{r}}|c\phi_{\mathrm{NE}}+d\phi_{\mathrm{CT}}\rangle \\ &= e\langle\psi_0|\vec{\mathbf{r}}|c\phi_{\mathrm{NE}}\rangle = c\mu_{\mathrm{NE}}. \end{aligned} \tag{4.1.9}$$

We can divide equation (4.1.8) by equation (4.1.9)

$$\frac{\mu_1}{\mu_2} = \frac{a}{c}. \tag{4.1.10}$$

Together with equation (4.1.5), we can calculate the CT ratio of the excited states

$$CT_1 = \frac{b^2}{a^2+b^2} = \frac{\mu_2^2}{\mu_1^2+\mu_2^2}, \quad CT_2 = \frac{d^2}{c^2+d^2} = \frac{\mu_1^2}{\mu_1^2+\mu_2^2}. \tag{4.1.11}$$

However, the transition dipole moments of $^1\mathrm{B}_2$ states go to zero in the limit of

$\varphi = 0°$. As the corresponding squared transition dipole moments become very small, for these states the analysis can only be applied for $\varphi > 30°$. At 0° rotation the symmetry of the dimer is D_{2h} and so that $^1B_2$ state becomes a $^1B_{2g}$ one and the transition from the ground state to this state is symmetry forbidden. In the following the symmetry of the structures at 0° and 90° (D_{2d}) are decreased to D_2 for reasons of simplicity. But this change of symmetry does not change the picture introduced above.

4.1.3. Potential energy curves and transition dipole moments

In contrast to the local approach, the super molecule approach also accounts for effects resulting from the mixing of orbitals of both monomers, i. e. it should be the method of choice for aggregates with distances smaller than 4 Å.[37] In this approach the electronic coupling matrix element V_{EC} is given as one half of the energy difference between the positive and the negative linear combinations of both NE states.[90,115] Super molecule computations provide a delocalized picture for dimers consisting of two identical monomers. The resulting delocalized adiabatic states are formally linear combinations of the diabatic NE and CT configurations (Fig. 2.1). Hence, they can also be classified as NE and CT states. Nevertheless, for such approaches the terms NE or CT excited state become misleading as they actually characterize single diabatic configurations[61,116] rather than complete adiabatic electronic wave functions. The natures of the latter are determined by linear combinations of several configurations with different characters. However, as a starting point it is justified to classify the states according to their dominating character as NE or CT states. As this is also the common terminology in the field, we will use this in the following. For qualitative and quantitative decisions the computed transition dipole moments are used.
Fig. 4.3 compares TD-HF-D (left) and SCS-CC2 (right) for a torsional motion of a perylene bisimide (PBI) dimer. As expected from this level of theory, TD-HF-D overestimates the excitation energies. But besides this the shapes of the potential energy curves, in particular the minima and the crossing points, are very similar to the SCS-CC2 results. This is pointed out in Fig. 4.4, which gives the differences between excitation energies calculated with TD-HF-D and SCS-CC2 as a function of the torsion angle φ. TD-HF-D overestimates the excitation energies of the two lowest electronically excited states (1^1B_1, 1^1B_2) by about 0.2 eV.

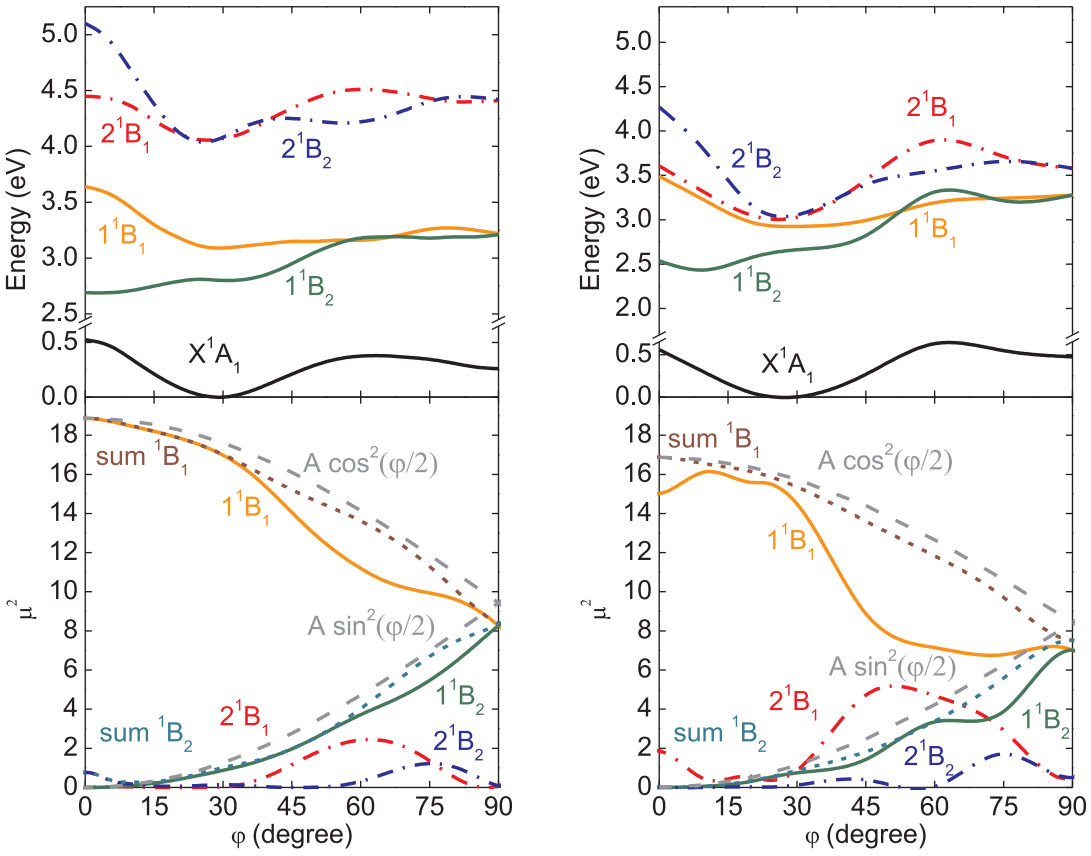

Figure 4.3.: Comparison of TD-HF-D (left) and SCS-CC2 (right) results on a PBI dimer. Upper part: Potential energy curves of the ground (black) and NE excited (color, solid) and charge transfer (color, dot-dashed) states as a function of the torsional angle φ. Lower part: Squared transition dipole moment of the NE excited (solid) and charge transfer (dot-dashed) states. The dashed lines are the sum of the squared transition dipole moments of $^1B_1$ (brown) and $^1B_2$ (blue) states.

But the relative error is less than 0.1 eV. For the next higher states (2^1B_1, 2^1B_2), which mainly have CT character, the absolute error is considerably larger (0.9 - 1.0 eV). However, the relative error is again very constant and varies by only about 0.2 eV. This shows that the TD-HF-D data are shifted by 0.2 eV for mainly NE and 0.9 eV for mainly CT states. It provides relative excitation energies with error bars within the accuracy of the SCS-CC2 method. In Fig. 4.3 the squares of the transition dipole moments are also plotted. For this property TD-HF-D is in good agreement with SCS-CC2 as well. This underlines the good performance of TD-HF-D and explains the success of this method in the work of Zhao

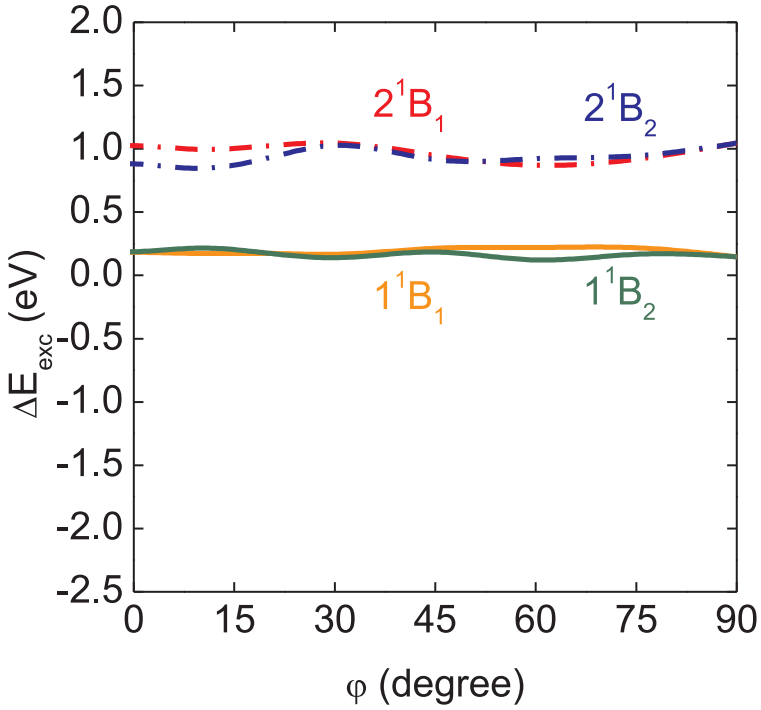

Figure 4.4.: Difference between the excitation energies of TD-HF-D and SCS-CC2 $\left(\Delta E_{\text{exc}} = E_{\text{exc}}(\text{TD-HF-D}) - E_{\text{exc}}(\text{SCS-CC2})\right)$.

et al..[91,94]

TD-DFT approaches are very useful for the description of optical properties of dye monomers.[99,117,118] As mentioned before, they are problematic for dimers or larger aggregates since they strongly underestimate the excitation energy of CT states.[72] As shown in Fig. 4.5 and Fig. 4.6, this is the case for PBI dimers as well. The figures summarize the adiabatic potential energy curves computed with dispersion corrected TD-BLYP-D, TD-B3LYP-D, TD-BHLYP-D and TD-CAM-B3LYP-D. Further DFT functionals like PBE and PBE0 behave very similar. Hence, their results are listed in the appendix D. TD-B3LYP-D predicts four excited states within the energetic range of 1.8 - 3.3 eV (Fig. 4.6 left). The computed transition dipole moments reveal that the energy position of predominantly NE and CT states are reversed in comparison to SCS-CC2. While SCS-CC2 for example predicts stronger transition dipole moments for 1^1B_1 and 1^1B_2 and considerably smaller ones for 2^1B_1 and 2^1B_2, TD-B3LYP-D predicts the opposite. Interestingly, while the considered adiabatic states possess different characters the shapes of the two lowest potential energy curves predicted by TD-B3LYP-D strongly resemble the shapes of the two lowest excited SCS-CC2 curves. Both

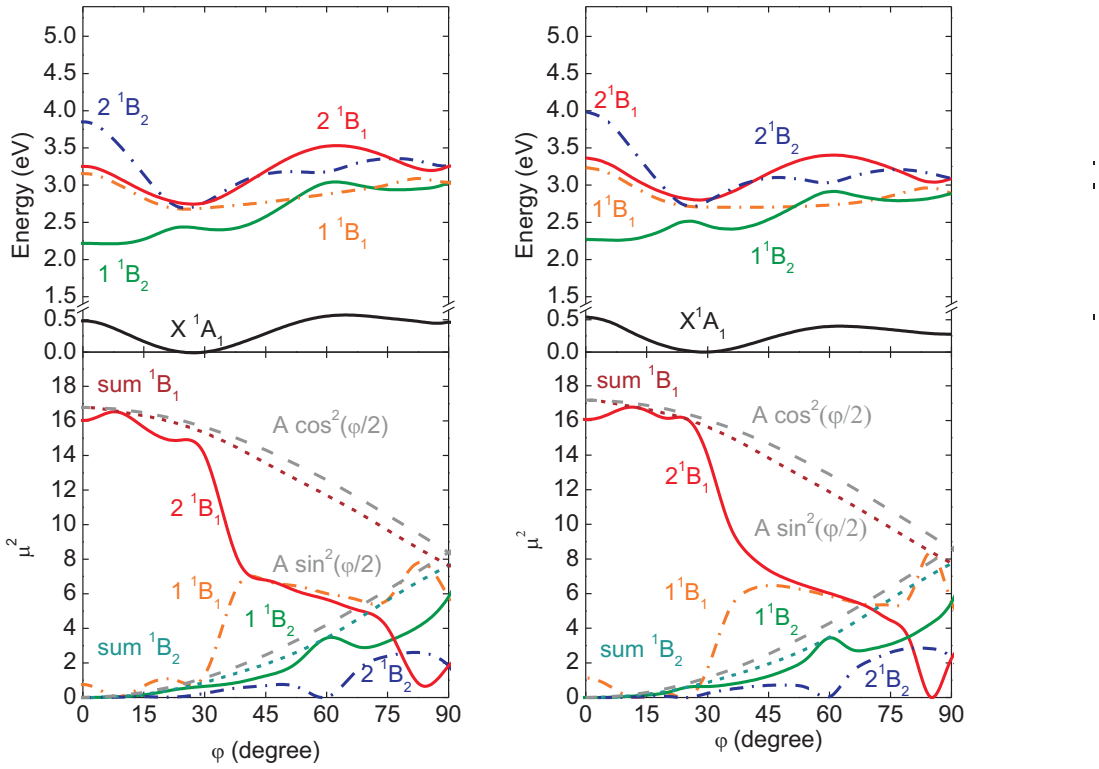

Figure 4.5.: Comparison of an LC and a hybrid DFT functional: CAM-B3LYP-D (left), BHLYP-D (right). See Fig. 4.3 for further explanations of the curves.

methods predict that the potential energy curve of 1^1B_1 state has a global minimum at $\varphi \approx 30°$. The minimum of 1^1B_2 state is found at about $\varphi = 15°$ with a slight ascend to $\varphi = 0°$. Both methods also predict crossings of 1^1B_2 and 1^1B_1 states at about 50° and 65°. But they differ in the energy separation of both states for $15° < \varphi < 45°$. However, this difference is astonishingly small, if one takes into account that the TD-B3LYP-D states have predominantly CT character while SCS-CC2 characterizes them as NE states.

Also the predicted shapes of the upper potential energy curves (2^1B_1, 2^1B_2) resemble the ones predicted by SCS-CC2 despite their different characters. In comparison to SCS-CC2, TD-B3LYP-D underestimates their energy separation. For $\varphi = 0°$ both methods predict 2^1B_2 to be higher in energy than 2^1B_1. However, while the energy difference is about 0.7 eV for SCS-CC2, TD-B3LYP-D provides a separation of less than 0.5 eV. Since both methods predict very similar shapes for 2^1B_2, TD-B3LYP-D finds a crossing between both states already at about 15° which is not found by SCS-CC2. It predicts 2^1B_2 to be beneath 2^1B_1

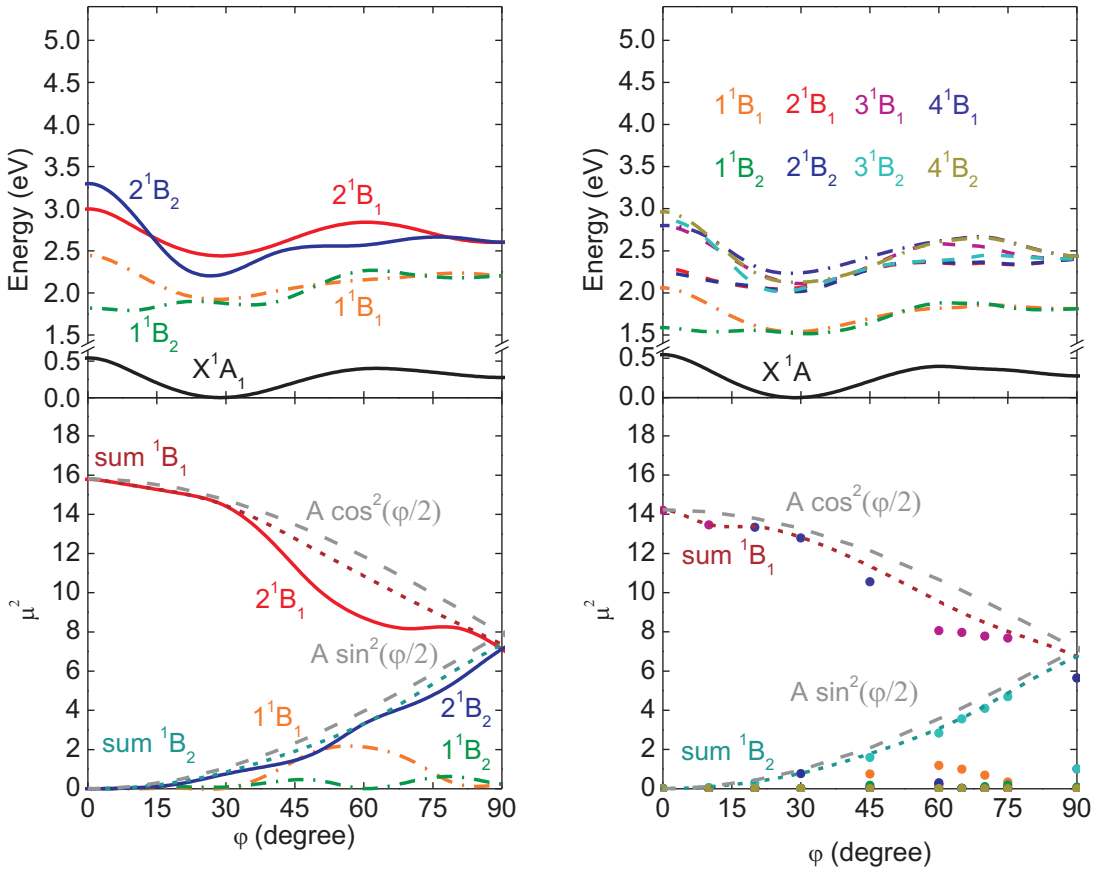

Figure 4.6.: Comparison of DFT functionals with different amount of exact HF exchange: B3LYP-D (left), BLYP-D (right). Upper part: Potential energy curves of the ground (black), charge transfer (color, dot-dashed), neutral (color, solid) and character undefined (color, dashed) excited states as a function of the torsion angle φ. Lower part: Squared transition dipole moment of the excited states (points). The dashed lines are the summation of the transition dipole moments of the excited states with B_1 symmetry (brown) and B_2 symmetry (turquoise) respectively.

for $15° < \varphi < 75°$. For $\varphi > 75°$ both states are virtually degenerate. SCS-CC2 finds no crossing for smaller ψ values. Both states are virtually degenerate for $25° < \varphi < 45°$. For $45° < \varphi < 75°$ also SCS-CC2 finds 2^1B_2 to be beneath 2^1B_1. For $\varphi > 75°$ both states are predicted to be virtually degenerate again in agreement with TD-B3LYP-D. Please note, that both methods predict a maximum of 2^1B_1 potential energy curve at about 60°. Summarizing, the shape of TD-B3LYP-D and SCS-CC2 potential energy curves are similar, but the characters of the corresponding states are interchanged.

This is underlined by Fig. 4.7. On the left side the differences in the excitation energies of the states (TD-B3LYP-D vs. SCS-CC2) not considering the character of the states but only their energy order are depicted. The excitation energies are slightly too low but the relative errors are below 0.5 eV, slightly larger than found for TD-HF-D. The picture changes completely if we compare the excitation energies to the states with NE and CT character (Fig. 4.7 right). In this case the relative errors made by TD-B3LYP are in the order of 1.5 eV. Such an error is unacceptable because it reflected in the calculated absorption spectra as the strong transitions are correlated to excitations to NE states, while the weak ones corresponds to excitation to CT states. All these findings for TD-B3LYP-D hold for TD-PBE0-D as well (see appendix D).

TD-HF-D strongly overestimates the energetic position of the CT states. Hence, one expects that an enhanced exact exchange contribution to the functional increases the energy of CT states relative to the energy of NE states. A lowering of the fraction of exact exchange should lead to the opposite behavior. This is indeed found if the TD-BHLYP-D and TD-BLYP-D curves are compared to their TD-B3LYP-D counterparts. The TD-BHLYP-D results are given in Fig. 4.5, while the TD-BLYP-D curves are shown in Fig. 4.6. Like TD-B3LYP-D, TD-BHLYP-D predicts four low lying electronic states. As found for B3LYP 1^1B_1 and 2^1B_1 curves resemble their SCS-CC2 counterparts but the energy order of NE and CT states are reversed. The potential energy curves of $^1B_2$ states are considerably different to their SCS-CC2 counterparts. Both SCS-CC2 and TD-BHLYP-D predict a maximum of 1^1B_2 curves at around 65°. However, TD-BHLYP-D predicts a distinct second maximum at about 30° which is neither found by SCS-CC2 nor TD-HF-D. Considering the shapes of the potential energy curves of both $^1B_2$ states this second maximum results from avoided crossings between both states. Similar avoided crossings are not observed in SCS-CC2. Since the shape of the potential energy curves differ completely from the SCS-CC2 ones, we refrain from further discussions.

As an example for LC DFT we used the TD-CAM-B3LYP-D method to test its applicability for the PBI dimer. In Fig. 4.5 the potential energy curves of the ground and the four lowest excited states are plotted. The shapes of the states resemble closely the ones of TD-BHLYP-D. So 1^1B_1 and 2^1B_1 curves resemble their SCS-CC2 counterparts, but again the energy order of the CT and NE states is reversed as shown by the transition dipole moments. For angles smaller than 45° 2^1B_1 state for example possesses a non-vanishing transition dipole moment,

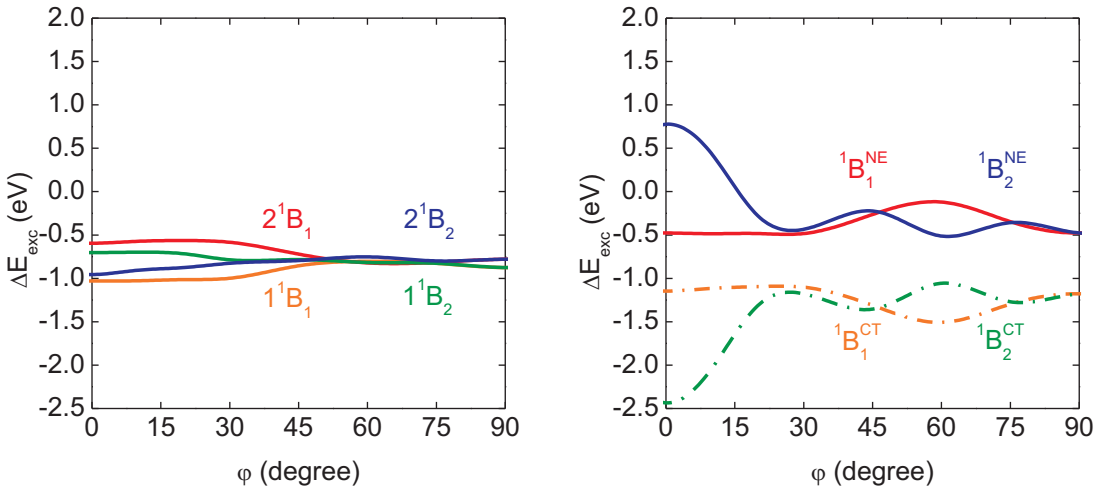

Figure 4.7.: (left) Difference between the excitation energies of TD-B3LYP-D and SCS-CC2 $\left(\Delta E_{\mathrm{exc}} = E_{\mathrm{exc}}(\text{TD-B3LYP-D}) - E_{\mathrm{exc}}(\text{SCS-CC2})\right)$ only considering the energy sequence of the states. (right) Difference between the excitation energies of TD-B3LYP-D and SCS-CC2 $\left(\Delta E_{\mathrm{exc}} = E_{\mathrm{exc}}(\text{TD-B3LYP-D}) - E_{\mathrm{exc}}(\text{SCS-CC2})\right)$ for the states of corresponding characters.

which is characteristic for NE states. A possible reason for the surprising failure of TD-CAM-B3LYP-D is that for the PBI dimer the energetic positions of one diabatic CT and one NE states of the same symmetry are very close to each other. Therefore already small deviations can result in a completely different energy order of the calculated adiabatic states. This may result from the characters of the involved orbitals. In the PBI dimer the highest two occupied and the lowest two unoccupied orbitals, which mainly describe the investigated NE and CT excited states, are completely delocalized over both monomers. Therefore r_{12} value for the transitions into both types of states should be comparable. According to T. Yanai *et al.* [59] such intermediate values for r_{12} should result in a more or less equal mixture of exact and DFT exchange, which may explain the strong similarity between TD-CAM-B3LYP-D and TD-BHLYP-D.

In contrast to all other methods considered up to now, TD-BLYP-D (see Fig. 4.6) describes eight electronic states in the energy range of 1.5 to 3.0 eV, which possess non-zero transition dipole moments. The same holds for TD-PBE-D (see appendix D). From the transition dipole moments it is obvious that two sets of CT states lie below the NE states. As for the two other TD-DFT approaches 1^1B_1 and 1^1B_2 states are energetically separated from the next higher lying states but

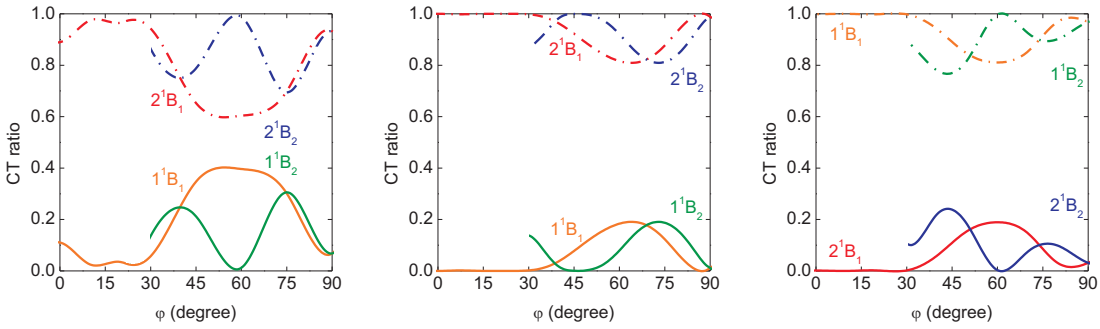

Figure 4.8.: Calculated ratio of CT character for the four lowest excited states given by SCS-CC2, TD-HF-D, and TD-B3LYP-D (from left to right).

due to the high density of states a strong mixing of the characters is found. This is corroborated by the transition dipole moments. In TD-BLYP-D as well as in TD-PBE-D 2^1B_1, 3^1B_1, and 4^1B_1 excited states have significant transition dipole moments. Since both functionals deviate much more from the more reliable SCS-CC2 results than the other approaches we refrain from further discussions and present the corresponding data in the appendix D.

4.1.4. Characters of the adiabatic states

Within Förster theory the square of the transition moments of the two NE states are proportional to $\cos^2(\varphi/2)$ and $\sin^2(\varphi/2)$ for $^1B_1$ $^1B_2$ states respectively.[78] Fig. 4.3 shows that this behavior is only found for the sum of the squares of the transition dipole moments of both $^1B_1$ or $^1B_2$ states. Furthermore the transition dipole moments of the so-called CT states which were expected to be zero become astonishing large for some orientations. This indicates that the computed adiabatic states represent linear combinations of NE and CT configurations. The contributions of both types of diabatic configurations to the overall adiabatic wave functions are plotted in Fig. 4.8. As discussed above they are estimated from the transition dipole moments of the adiabatic states assuming that the diabatic CT configurations do not contribute to this value. For B_2 symmetry this approach can only be used for structures at which the transition dipole moment of the NE $^1B_2$ configuration is significantly different from zero ($\varphi > 30°$).
In the case of SCS-CC2 Fig. 4.8 reveals an almost pure NE character in 1^1B_1 state for $\varphi < 45°$. Some CT character is only found for $\varphi < 10°$ but the contribution remains below 15 %. For torsion angles between 45° and 75° 1^1B_1 and

2^1B_1 states show a strong mixing of the NE and CT configurations. With about 60 % contribution 1^1B_1 is still predicted to be predominantly neutral. However, for this range it is no longer justified to classify it as a NE state. The same holds for 2^1B_1 state with respect to its CT character. Similar trends exist for the two lowest $^1B_2$ states as well. The strong mixture of NE and CT character in the adiabatic excited states clearly confirms that the terms NE and CT states has to be regarded with suspicion. They only designate the dominating character of the states. For the regions around the minimum of the ground state ($\varphi \approx 30°$) the classification in NE and CT is still appropriate since the admixtures are less than 15 %. Hence, this differentiation still holds for the excitation spectrum of PBI dimers.

The character analysis of the TD-HF-D curves reproduces the trends achieved with SCS-CC2. As the CT configurations are predicted at too high energies, the mixing of the characters of the excited states is too small. Please note, that the conclusions drawn for $^1B_2$ states are less clear cut as the transition dipole moments are quite small for $\varphi < 45°$. Nevertheless, for $0° < \varphi < 40°$ TD-HF-D and SCS-CC2 deliver very similar pictures. This explains the success of TD-HF-D in the interpretation of the absorption and emission spectra of PBI aggregates [91,94] which are mainly determined by the properties in this region. For wide ranges of the potential energy curves, TD-B3LYP-D predicts the wrong energy order of the predominantly NE and CT states. However, the admixture of CT character to the predominantly NE state and vice versa agrees qualitatively with the SCS-CC2 results. Keeping this in mind, it is surprising that this agreement is not reflected in the potential energy curves. In contrast our computations clearly show that the TD-B3LYP-D potential curves of the predominantly NE states resemble the SCS-CC2 potential curves of the states with predominantly CT character and vice versa.

This behavior is explainable from the mixed characters of the states. The mixing indicates strong interactions between the underlying diabatic configurations which influence the shapes of the resulting adiabatic states. In such a case the upper state is always shifted to higher energies while the lower one is moved in the opposite direction. [61,119] The sizes of the shifts depend on the coupling matrix element and the energy separation between the diabatic configurations. The energy difference between NE and CT diabatic states is given by the interaction between (i) a ground state and a HOMO-LUMO excited PBI molecule and (ii) a PBI anion and a PBI cation. These energy differences are typically rather inde-

pendent of the mutual orientation of the PBI moieties. Hence, if the coupling matrix element between the NE and the CT configurations is of the same order of magnitude as their energy difference, the predominantly NE states which are predicted to be lower with SCS-CC2 are shifted to even lower energies. Simultaneously, the energy of the states with predominating CT character lying above are increased. For the two $^1B_1$ states this situation is found for $\varphi \approx 60°$. According to the transition dipole moments and the mixed character a strong interaction between the diabatic states takes place. The interaction shifts the adiabatic 2^1B_1 state upwards so that a maximum is found. The corresponding adiabatic 1^1B_1 state is shifted downwards. Also for TD-B3LYP-D the upper state is up shifted while the lower state is down shifted. As a consequence the potential energy curve of the upper TD-B3LYP-D states resembles the potential energy curve of the upper SCS-CC2 state, i. e. the curve of the NE TD-B3LYP-D state looks like the one found for the CT state with SCS CC2. The same is found for both lower states. The comparable shapes indicate that TD-DFT even describes the size of the interaction between both states qualitatively correct. However, due to the different order, the resulting splittings go in the wrong direction.
For $\varphi < 20°$, similar interactions seem to affect the shape of both adiabatic $^1B_2$ states quite significantly. For SCS-CC2 the lower lying NE state 1^1B_2 is moved downwards while the corresponding higher lying CT state 2^1B_2 moves upwards. This behavior can be explained by an increasing interaction between the underlying diabatic states. This explanation is supported by the fact that also the TD-B3LYP-D curves behave similarly. However, due to the wrong energy order now the lower lying CT states move downwards while the higher lying NE states move upwards. For TD-BHLYP-D the influence of such interactions is even stronger, since NE and CT configurations are even closer in energy. As a consequence $^1B_2$ states show several avoided crossings which are not found by the other approaches.
These findings explain the failure of TD-B3LYP-D and TD-BHLYP-D in the work of Zhao *et al.* [91] In this work they used vertical transition energies to the electronic state which possesses the highest transition dipole moment. The calculations compared differently substituted PBIs which have different geometrical orientation in the crystals. This means that the trends in these vertical excitation energies mainly reflect the shapes of the NE excited states. As TD-DFT incorrectly predicts CT states to lie below these NE states, the NE states are shifted upwards at regions of significant couplings between the CT and NE states. As the energy

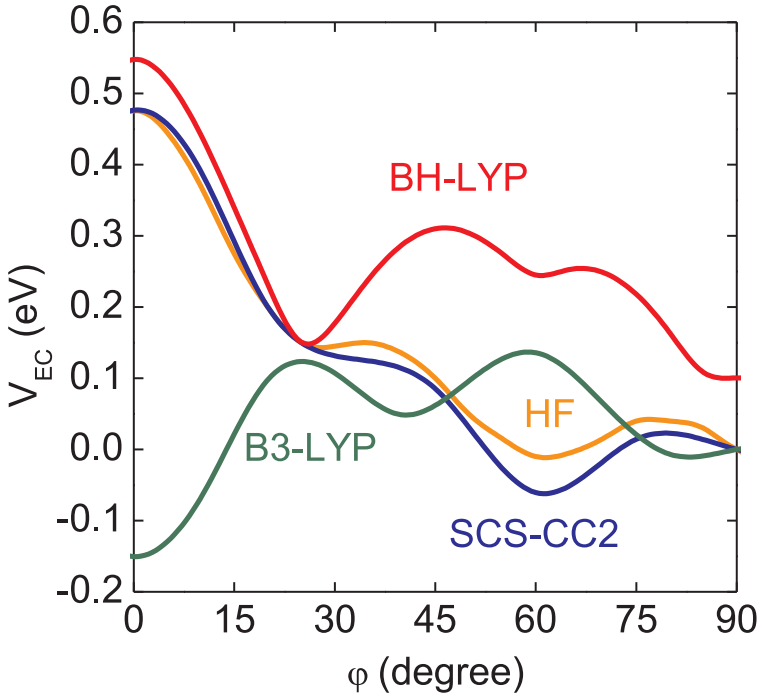

Figure 4.9.: Comparison of the electronic coupling parameter V_{EC} predicted by different methods.

difference between the diabatic NE and the CT configuration is almost constant, the excited state potential energy curves are shifted in the wrong direction and a severe disagreement with the correct values is found. For TD-HF-D on the other side, the shapes of the NE states are correctly reproduced. The errors made in the energy positions of the CT states do not influence the conclusion that can be drawn out of the potential energy curves.

4.1.5. Implications to the exciton transfer process

The question arises how the different approaches differ in the predictions of the electronic coupling parameter V_{EC}. The computed values are given in Fig. 4.9. For all methods the parameter was computed as half of the energy differences of the predominantly NE states. Fig. 4.9 clearly shows that both B3LYP-D deviates strongly from the SCS-CC2 values for $0° < \varphi < 20°$ and $50° < \varphi < 70°$, while BHLYP-D deviates for $30° < \varphi < 90°$. The strong deviations in V_{EC} result from the interactions between the diabatic states in combination with the wrong energy order which leads to an up shift of the NE $^1B_2$ while a downshift is pre-

dicted for SCS-CC2. For $20^\circ < \varphi < 50^\circ$ the deviations are considerably smaller. For the minimum of the ground state (30°) TD-B3LYP-D and TD-BHLYP-D predict $V_{EC} \approx 863\ cm^{-1}$ (0.107 eV) and 1428 cm^{-1} (0.177 eV) respectively, while SCS-CC2 and TD-HF-D compute $V_{EC} \approx 1061$ cm^{-1} (0.132 eV) and 1170 cm^{-1} (0.145 eV) respectively. These values agree quite nicely to the corresponding values given by Guthmuller *et al.* [93] (875 cm^{-1} for TD-B3LYP and 1260 cm^{-1} for TD-HF). While TD-DFT-D approaches deviate quite strongly from the SCS-CC2 values, TD-HF-D is in nearly perfect agreement to it. Smaller deviations between TD-HF-D and SCS-CC2 are only found for $50^\circ < \varphi < 70^\circ$ a region being less important for the optical properties of PBI aggregates.

Detailed models about exciton traps are very important since such traps are responsible for the low efficiency of the excitation energy transfer in organic materials. On the basis of TD-HF-D computations we recently suggested a new model for exciton trapping in π-conjugated materials which in contrast to previous models by Forrest *et al.* [12,82] does not depend on relaxations to CT states. Instead, the trapping results from a quenching of the photoabsorption to 1^1B_2 state (Fig. 4.3) followed by a vibrational relaxation along the torsional coordinate. This relaxation happens on a highly anharmonic potential energy curve and leads to the minimum of 1^1B_2 state at $\varphi \approx 0^\circ$ to 10°. In this geometrical orientation the exciton is trapped since the fluorescence is reduced and even becomes dipole forbidden at $\varphi = 0^\circ$. Furthermore, the emission is strongly red shifted with respect to the absorption due to the different shapes of the potential curves of the ground and excited states.

SCS-CC2 predicts the same model, as the energy order of the excited states and the shapes of the potential energy curves do not differ considerably from the data obtained with TD-HF-D. Note that all calculations introduced here are done for the gas phase and therefore environmental effects are neglected. Most importantly the CT states remain above the NE ones although they are strongly shifted to lower energies. As a consequence the new, considerably more accurate curves also do not predict the involvement of CT states in the trapping processes. The present analysis, however, shows that the involved states are not purely neutral in character but have admixtures of CT character. This is in line with recent works of Scholz *et al.* [30,120] which, however, does not consider anharmonic potentials.

In the DFT picture, the trapping would result from relaxations to these CT states, because the predominantly CT states are predicted to be below the NE ones. This

would be in line with previous models,[12,64,86] but the more reliable SCS-CC2 approach proves that the energy order is wrong. Beside the wrongly shaped potential energy curves this is the second reason why TD-DFT based models should be handled with great care.

4.1.6. Conclusion

The present section investigates the reliability of different quantum mechanical methods for the description of optoelectronic properties of PBI aggregates. We concentrate on properties which are important for the use of PBI in optoelectronic devices e. g. UV/VIS absorption and emission spectra and electronic exciton transfer effects. Using PBI dimers as model systems, the accuracy of TD-HF-D, TD-CAM-B3LYP-D, TD-BHLYP-D, TD-B3LYP-D, and TD-BLYP-D are determined by a comparison with the SCS-CC2 method which is well known for its accuracy of 0.1 to 0.2 eV. The reliabilities of the methods are demonstrated by the predicted shapes of the potential energy curves, the characters and the energy order of the four lowest lying excited states. TD-HF-D agrees very well with SCS-CC2 in matters of energy orders, characters and shapes of the computed potential energy. This explains the success of this method for the description of crystallochromic solid-state effects of PBI dyes. It also supports a recent model for exciton traps which is based on TD-HF-D computations for the assignment of absorption and emission spectra of PBI aggregates.
In almost all cases, TD-DFT approaches place the predominant CT states erroneously below the NE state. Due to the different order of NE and CT states the electronic interactions lead to wrong shifts of the given states. As a consequence the shapes of the potential energy curves are wrongly described. Surprisingly, this holds also for the long-range corrected TD-CAM-B3LYP-D method. Due to this failure the used TD-DFT-D methods are also not able to predict reliable electronic exciton coupling elements. Accidentally, only small deviations from SCS-CC2 are found for the region around the minimum of the ground state.
The SCS-CC2 computations support our recent model for exciton trapping in π-conjugated materials, which is based on gas-phase calculations. In line with previous suggestions the present analysis shows that the involved states are not purely neutral in character but have admixtures of CT character. In the next section, we will apply the better formulated character analysis method on the SCS-CC2 calculation results of the PBI dimer system. A character analysis

method based on the model Hamiltonian method will be discussed as well.

4.2. Character analysis for the PBI dimer

4.2.1. Introduction

According to Petelenz,[23] CT states of solid molecular species are defined by a transfer of at least one electron between the constituting molecules of the sample. Such states appear upon aggregation and cannot be observed in spectra that contain exclusively electronic transitions within individual molecules which gives rise to NE states. A pictorial representation of CT and NE states is shown in Fig. 2.1 for a dimer system of two molecules A and B. Here a one particle transition between the highest occupied orbital (HOMO) to a lowest unoccupied orbital (LUMO) is considered. In the left hand side of Fig. 2.1, an electron is excited from the HOMO of monomer B to the LUMO of monomer B, which corresponds to a NE state. Similarly, in the right hand side of the figure, an electron is excited from the HOMO of monomer B to the LUMO of monomer A, which gives rise to a CT state.

Due to the quantum mechanical nature of electronic wave functions the definitions given above are an oversimplification of the reality. In fact, an unambiguous assignment of a wavefunction of such a dimer system to one or the other monomer is not possible, even if such an assignment is given by an *ad hoc* definition, any electronic state of an aggregate system will contain admixtures of both CT and NE configurations as we show in the last section. These are only diabatic configurations that can be set up to define the actual wavefunction. Thus, electronic states of two or more molecules will practically always contain an admixture of both characters.

One could argue that a charge transfer state can, nevertheless, be recognized by the fact that one electron is transferred from one monomer to the other one which causes a significant change of the dipole moment of the system. However, in many systems of interest the two monomers are symmetric. Thus, the properly symmetric CT states will contain equal contributions of charge transfer from A to B as for a transfer from B to A and the total dipole moment of such an electronic state is small or even zero. The same holds for NE states. For a further discussion about this point see the works of Dreuw, Head-Gordon, Hierlinger and Görling.[72,73,74,75] Nevertheless, it is often justified to designate

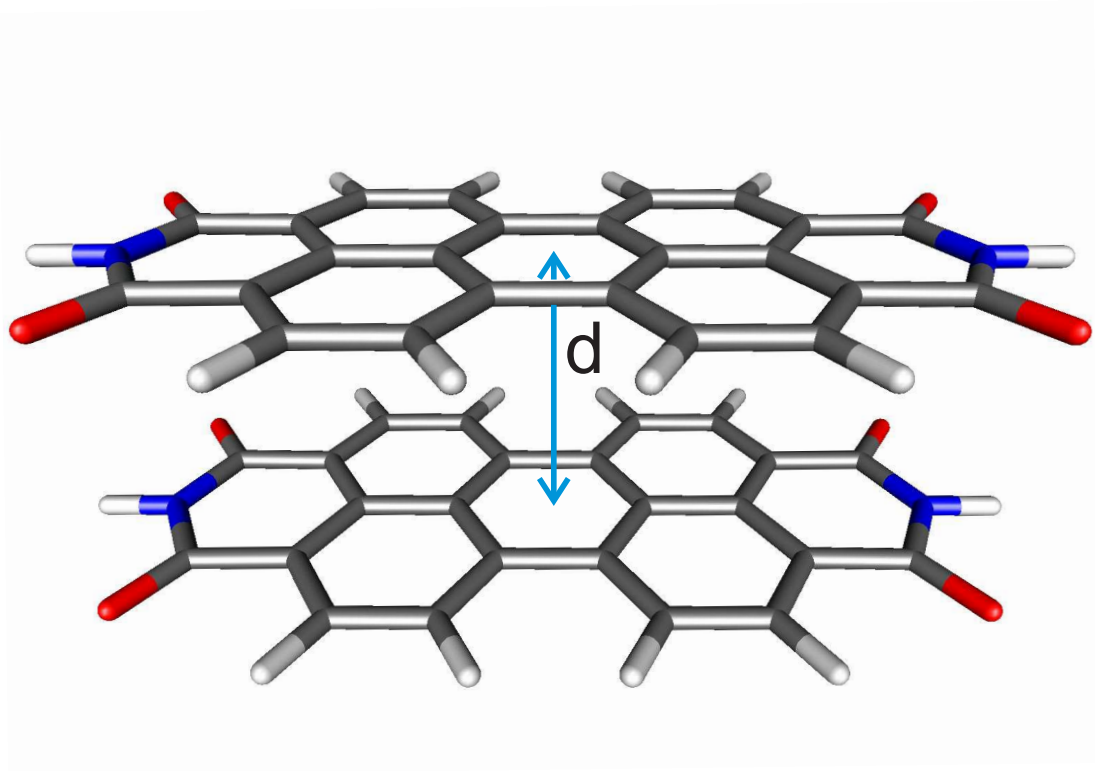

Figure 4.10.: Translation mode for PBI dimer.

the electronic states as NE or CT according to its predominant character. In typical quantum chemical calculations, e. g. those of configuration interaction type and propagator methods such as time-dependent density functional theory (TD-DFT), the excited states are represented in terms of delocalized orbitals. An analysis of the CT and NE character actually requires localization and orthogonalization of the orbitals. In the present section we propose such a method (3.4) and apply it to a system of two 3,4,9,10-perylene tetracarboxylic acid bisimide (PBI) monomers.

4.2.2. Calculation procedures

We consider the character analysis using the example of a system of two PBI molecules.[91,94] A translation and a torsion motion are investigated for two PBI molecules as shown in Fig. 4.10 and 4.2. For the translation motion the PBI molecules are placed in a π-stacked, eclipsed (face to face) orientation and the distance between the two monomers centers is varied from 3.0 Å to 10.0 Å. All

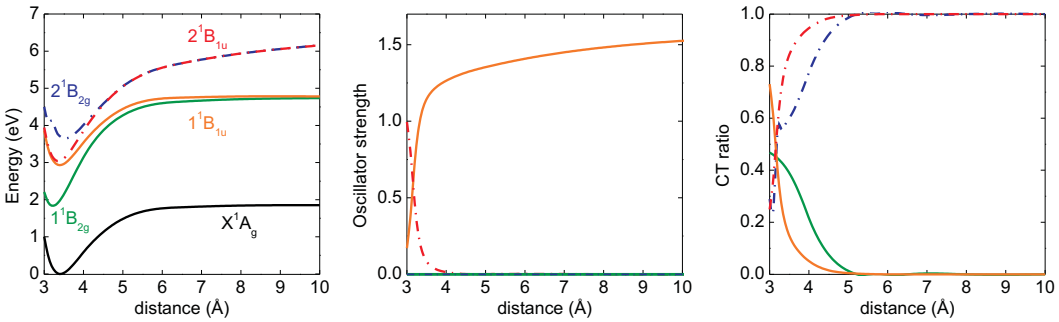

Figure 4.11.: Translation motion: (left) potential energy curves of ground and excited states; oscillator strengths of excited states; ratio of charge transfer character of excited states.

the structures in the translation motion have D_{2h} symmetry. The ground state and the four lowest excited states were calculated (Fig. 4.11 left) at the spin component scaled second order approximate coupled-cluster (SCS-CC2) combined with resolution-of-the-identity (RI) approximation.[97,102,103] We took the TZV basis set[62] for the H atoms and TZVP basis set[62] for all other atoms, and the TZVP auxiliary basis[101] for all atoms. The four excited states consist of two $^1B_{1u}$ states and two $^1B_{2g}$ states due to the HOMO-1, HOMO, LUMO and LUMO+1 orbitals which belong to the irreducible symmetry representations B_{3g}, A_u, B_{2u} and B_{1g}, respectively. The oscillator strengths of the excited states are also calculated (Fig. 4.11 middle).

For the torsion motion the PBI molecules are placed in the same way as the translation motion but the distance between the two monomers planes was fixed to 3.4 Å. Then we counter-rotated the monomers with respect to the axis that is orthogonal to the monomer planes from 0° to 90° (Fig. 4.2). These dimer structures can have D_{2h} (at 0°), D_{2d}(at 90°) and D_2(others) symmetries. To be constant, we rotated the structures at 0° and 90° by a tiny angle (0.001°) and calculated all the structures with D_2 symmetry. The oscillator strengths and the character analysis of the excited states are shown in Fig. 4.11 middle and Fig. 4.15 middle. All these calculations were conducted with the TURBOMOLE 6.0 program package.[100]

As a comparison, the character analysis based on the simplified two-state model for SCS-CC2 results (section 4.1.4) is discussed. Furthermore, the torsion motion was calculated with the model Hamiltonian method. Necessary integrations for model Hamiltonian method were calculated in the CISD(4,4)/SV(P)[121]

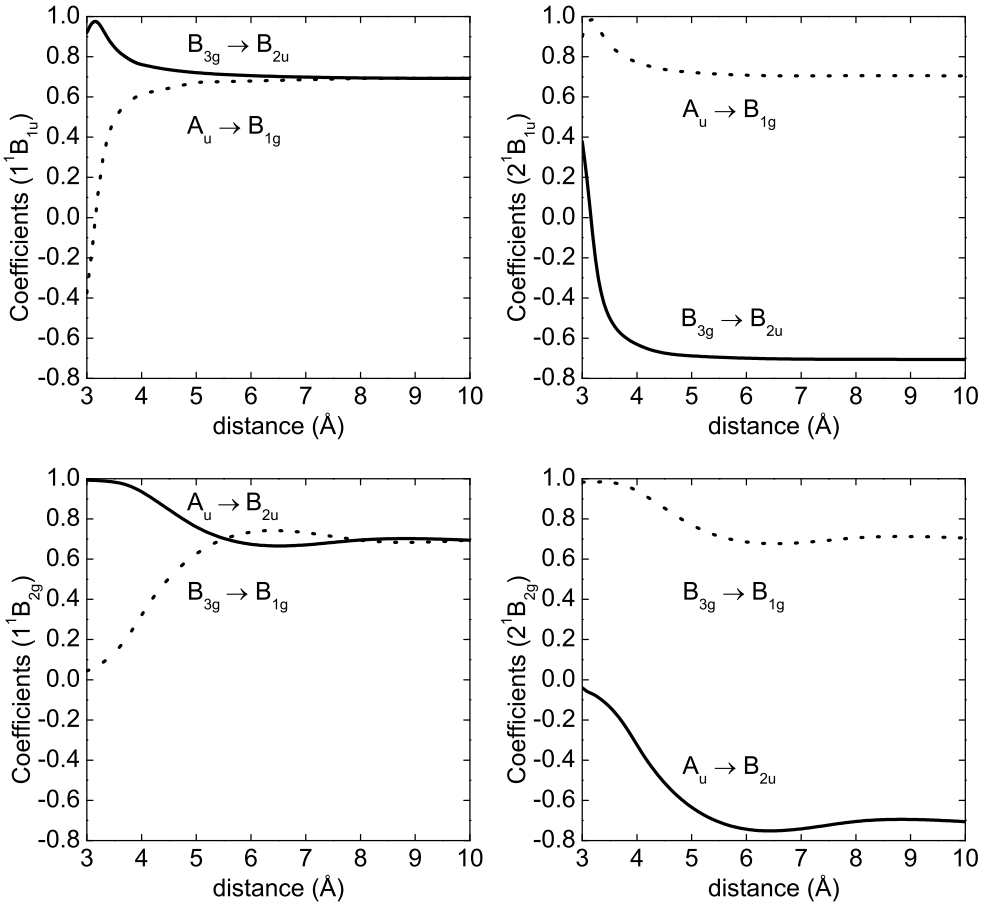

Figure 4.12.: CI coefficients of the major configurations of excited states.

level of theory with the WAVELS program package. [122]

4.2.3. Translation motion

For the considered translation motion of the PBI dimer, the potential energy curves (Fig. 4.11 left) of the two energetically lower excited states (1^1B_{1u} and 1^1B_{2g}) reach a limiting energy (of 4.8 eV) at long distance region. In the character analysis figure (Fig. 4.11 right), these two states are also approaching pure NE character at long distance region. On the other hand, at long distances the potential energy curves of the two energetically higher excited states (2^1B_{1u} and 2^1B_{2g}) show a $-1/r$ behavior of the Coulomb interaction that is characteristic for CT states. [73] As expected the character analysis shows that these two states are approaching pure CT character at long distances. To understand these curves, it is important to look at the wavefunctions of the excited states. Therefore, we

plotted the coefficients of the largest two diabatic excitation configurations of each excited state (Fig. 4.12) as a function of the monomer distance. For each excited state the two major configurations already contribute more than 95 % to the excited states. Thus, simplified but qualitatively correct wavefunctions are given by these two configurations

$$\Psi_{1^1\mathrm{B}_{2g}} = a_{11}\Phi_H^L + a_{12}\Phi_{H-1}^{L+1}, \tag{4.2.1}$$

$$\Psi_{2^1\mathrm{B}_{2g}} = a_{21}\Phi_H^L + a_{22}\Phi_{H-1}^{L+1}, \tag{4.2.2}$$

$$\Psi_{1^1\mathrm{B}_{1u}} = a_{31}\Phi_{H-1}^L + a_{32}\Phi_H^{L+1}, \tag{4.2.3}$$

$$\Psi_{2^1\mathrm{B}_{1u}} = a_{41}\Phi_{H-1}^L + a_{42}\Phi_H^{L+1}. \tag{4.2.4}$$

These wavefunctions include only the HOMO-1, HOMO, LUMO and LUMO+1 orbitals of the PBI dimer. The character of these configurations can be analyzed if the relation of the dimer orbitals and the monomer orbitals is known. For long distances, where the overlap between the monomer orbitals becomes negligible, the dimer orbitals can be written in terms of the monomer HOMOs and LUMOs as

$$\psi_{H-1} = \frac{1}{\sqrt{2}}(\varphi_{H^1} - \varphi_{H^2}), \tag{4.2.5}$$

$$\psi_H = \frac{1}{\sqrt{2}}(\varphi_{H^1} + \varphi_{H^2}), \tag{4.2.6}$$

$$\psi_L = \frac{1}{\sqrt{2}}(\varphi_{L^1} - \varphi_{L^2}), \tag{4.2.7}$$

$$\psi_{L+1} = \frac{1}{\sqrt{2}}(\varphi_{L^1} + \varphi_{L^2}). \tag{4.2.8}$$

φ_{H^1} and φ_{H^2} are the HOMO of monomer I and II respectively. φ_{L^1} and φ_{L^2} are the LUMO of monomer I and II respectively. These equations will be more valid at long distances. However, even in the short distance region they are also qualitatively correct. For instance, Fig. 4.13 shows these dimer orbitals at the distance of 3.4 Å, and Fig. 4.14 shows the HOMO and LUMO of PBI monomer.
With these approximations, we can rewrite the configurations in terms of monomer

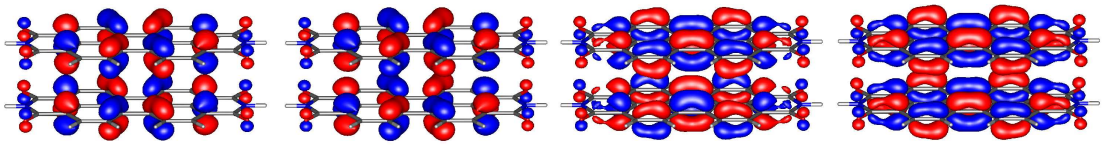

Figure 4.13.: PBI dimer orbitals of distance 3.4 Å from left to right are HOMO-1, HOMO, LUMO and LUMO+1 respectively.

Figure 4.14.: PBI monomer HOMO (left) and LUMO (right).

orbitals. As an example, Φ_H^L which denotes the electron excited from the HOMO to the LUMO is

$$\begin{aligned}
\Phi_H^L &= \frac{1}{2\sqrt{2}} \quad \Big(\quad \big|\psi_1\bar{\psi}_1\cdots\psi_H\bar{\psi}_L\big\rangle + \big|\psi_1\bar{\psi}_1\cdots\psi_L\bar{\psi}_H\big\rangle \quad \Big) \\
&= \frac{1}{2\sqrt{2}} \quad \Big(\quad \big|\cdots(\varphi_{H^1}+\varphi_{H^2})(\bar{\varphi}_{L^1}-\bar{\varphi}_{L^2})\big\rangle + \big|\cdots(\varphi_{L^1}-\varphi_{L^2})(\bar{\varphi}_{H^1}+\bar{\varphi}_{H^2})\big\rangle \quad \Big) \\
&= \frac{1}{2\sqrt{2}} \quad \Big(\quad \big(|\cdots\varphi_{H^1}\bar{\varphi}_{L^1}\rangle - |\cdots\bar{\varphi}_{H^1}\varphi_{L^1}\rangle\big) - \big(|\cdots\varphi_{H^2}\bar{\varphi}_{L^2}\rangle - |\cdots\bar{\varphi}_{H^2}\varphi_{L^2}\rangle\big) \\
&\quad - \quad \big(|\cdots\varphi_{H^1}\bar{\varphi}_{L^2}\rangle - |\cdots\bar{\varphi}_{H^1}\varphi_{L^2}\rangle\big) + \big(|\cdots\varphi_{H^2}\bar{\varphi}_{L^1}\rangle - |\cdots\bar{\varphi}_{H^2}\varphi_{L^1}\rangle\big) \quad \Big).
\end{aligned} \tag{4.2.9}$$

It is obvious that the first two terms $\big(|\cdots\varphi_{H^1}\bar{\varphi}_{L^1}\rangle - |\cdots\bar{\varphi}_{H^1}\varphi_{L^1}\rangle$ and $|\cdots\varphi_{H^2}\bar{\varphi}_{L^2}\rangle - |\cdots\bar{\varphi}_{H^2}\varphi_{L^2}\rangle\big)$ of equation (4.2.9) denote the NE configurations, which show the localized excitations from the HOMO of monomer 1 to the LUMO of monomer 1 and from the HOMO of monomer 2 to the LUMO of monomer 2, respectively. As the remaining terms refer to CT configurations, each of the delocalized excited configuration has 50% CT and 50% NE character.
By using equations (4.2.1) to (4.2.9), $\Psi_{1^1\mathrm{B}_{2g}}$ state can be rewritten as

$$\begin{aligned}
\Psi_{1^1\mathrm{B}_{2g}} \quad = \quad & \frac{1}{2\sqrt{2}}\Big(a_{11}\Big(\big|\psi_1\bar{\psi}_1\cdots\psi_H\bar{\psi}_L\big\rangle + \big|\psi_1\bar{\psi}_1\cdots\psi_L\bar{\psi}_H\big\rangle\Big) \\
& + a_{12}\Big(\big|\psi_1\bar{\psi}_1\cdots\psi_{H-1}\bar{\psi}_{L+1}\big\rangle + \big|\psi_1\bar{\psi}_1\cdots\psi_{L+1}\bar{\psi}_{H-1}\big\rangle\Big)\Big)
\end{aligned} \tag{4.2.10}$$

As shown in Fig. 4.12, at the short distances, $\Psi_{1\mathrm{B}_{2g}}$ state is dominated by the configuration Φ_H^L. Therefore, the state has roughly 50% NE and 50% CT character mixing.

In the long distance region, the state has equal contributions from the two major configurations Φ_H^L and Φ_{H-1}^{L+1}, where $a_{11} = a_{12}$, and turns out

$$\Psi_{1^1B_{2g}} = \frac{a_{11}}{\sqrt{2}}\left(|\cdots\varphi_{H^1}\bar{\varphi}_{L^1}\rangle + |\cdots\bar{\varphi}_{H^1}\varphi_{L^1}\rangle + |\cdots\varphi_{H^2}\bar{\varphi}_{L^2}\rangle + |\cdots\bar{\varphi}_{H^2}\varphi_{L^2}\rangle\right). \quad (4.2.11)$$

The diabatic CT configurations were compensated with each other. This results the pure NE character dominating $\Psi_{1^1B_{2g}}$ state. Similarly, for $\Psi_{1^1B_{1u}}$ state it has roughly 50% NE and 50% CT character mixing at short distances and pure NE character at long distances. The $\Psi_{2^1B_{2g}}$ and $\Psi_{2^1B_{1u}}$ states have an equal admixture of NE and CT character at short distances and pure CT characters at long distances.

So far, this approximation explained well for all the character changes of all the excited states in the translation motion. This is because the HOMO and LUMO of the PBI monomer are separated in energy from the other orbitals. Therefore, other configurations participate only merely in the four lowest excited states of the PBI dimer.

So far the driving forces that change these curves in this way are not well understood. In our analysis method, the CIS wavefunctions are transformed into a local MO basis making it possible to distinguish NE and CT configurations. It is obvious that the NE configuration energy is independent of the changes of the distance between two monomers, but the energy of CT configurations increases with the monomer distance with an asymptotic behavior of -1/r. Therefore, the NE and CT configurations may contribute both to the character of an excited state at short distances where they are energetically close to each other. However, at long distances the NE configurations dominate the energetically lower states, while CT configuration dominate the higher ones.

4.2.4. Torsion motion

In the works of Fink and Zhao *et al.* [91,94] about the EET trapping mechanism of PBI aggregates, we calculated a torsion motion of the PBI dimer. As shown in Fig. 4.15, the energy of the ground state and the four energy lowest excited states were calculated as well as their oscillator strengths and character analysis. The two energetically lower lying excited states are dominated by NE character, and the two higher excited states are mainly of CT character. The two $^1B_1$ states show strong character mixing in the 45° to 60° region. At the same time, the

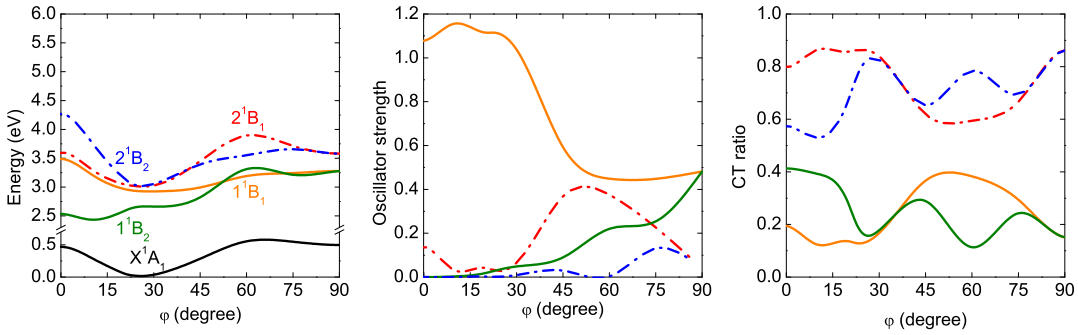

Figure 4.15.: Torsion motion: (left) potential energy curves of ground and excited states; (middle) oscillator strengths of excited states; (right) ratio of charge transfer character of the excited states.

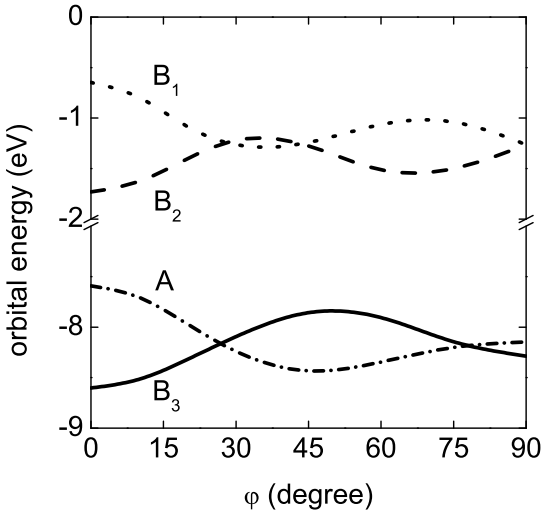

Figure 4.16.: Orbital energies of HOMO-1, HOMO, LUMO, LUMO+1 of the PBI dimer as a function of the torsion angle φ.

corresponding two energy curves repel each other strongly and the oscillator strength difference between the two states decreases. Similarly, for the two $^1B_2$ states an increase of the character mixing of the excited states always goes along with repulsion of the energy curves and a reduced oscillator strength difference. To understand the behavior of these curves, we used a similar explanation as we did for translation motion of PBI dimer. Since the torsion motion does not change the distance between the PBI monomers, the NE and CT configuration energies are roughly independent of this coordinate. However, the delocalized dimer MO energies change a lot along the torsional angles (Fig. 4.16), because the overlap of the monomer orbitals is a strong function of this coordinate.

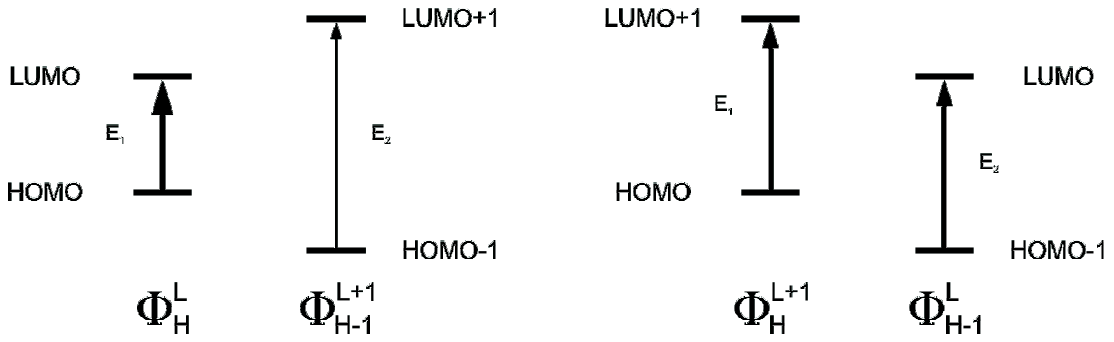

Figure 4.17.: Left: large ΔE results in unequal excitation contributions; Right: small ΔE results in equal excitation contributions.

Therefore, the excitation energy of different configurations also changes dramatically along the torsional angles. Since the two-configuration picture is valid for the excited state wavefunction of the PBI dimer (see appendix D), we introduce a term ΔE which is given as the excitation energy difference of these two configurations

$$\Delta E = E_1 - E_2. \tag{4.2.12}$$

As shown in Fig. 4.17 left, the excited state is expected to be dominated by one configuration for large absolute values of ΔE, which also results in strong NE and CT character mixing of the excited state (equation (4.2.9)). On the other hand, an equal contribution of the two both configurations is also expected if the excitation energies of the two configurations are identical (Fig. 4.17 right). Fig. 4.18 shows the excitation energy differences ΔE as a function of the torsional angles. For $^1B_2$ states ΔE is defined as $\Delta E = E_{\Phi^A_{B_2}} - E_{\Phi^{B_3}_{B_1}}$. For $^1B_1$ states ΔE is defined as $\Delta E = E_{\Phi^{B_3}_{B_2}} - E_{\Phi^A_{B_1}}$. The $\Phi^A_{B_2}$ represents a configuration in which an electron is excited from the occupied MO with A symmetry to virtual MO with B_2 symmetry and similar definitions apply for $\Phi^{B_3}_{B_1}$, $\Phi^A_{B_1}$ and $\Phi^{B_3}_{B_2}$. By comparing Fig. 4.18 and the right hand side of Fig. 4.15, it's obvious that large absolute ΔE value results in large character mixing in the excited states and vice versa. This corroborates our two-configuration approximation.

4.2.4.1. Comparison with the simplified model

Fig. 4.19 shows the CT ratio of these four excited states calculated with the simplified character analysis method (left) and with the analysis method proposed before. We found a good agreement between these two methods. For regions

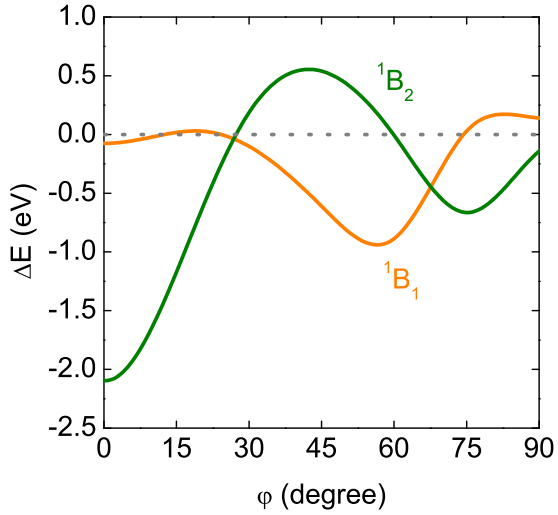

Figure 4.18.: ΔE for excited states of different symmetry representations as a function of the torsion angle φ.

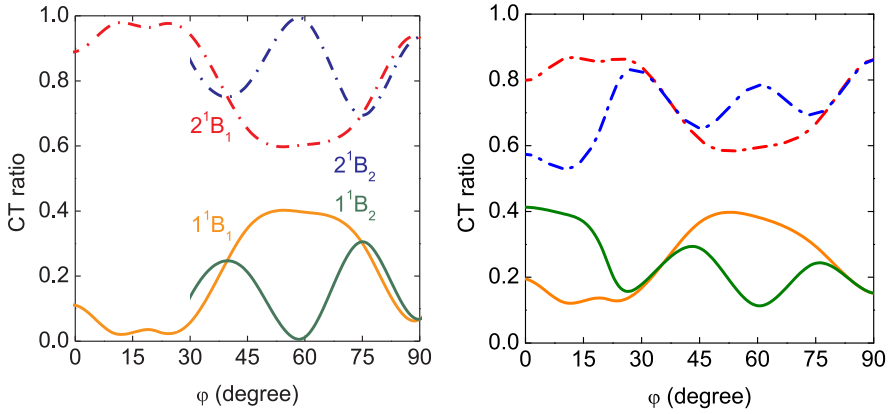

Figure 4.19.: Left: charge transfer analysis based on the transition dipole moment; Right: charge transfer analysis based on the SCS-CC2 results.

with strong character mixing, e. g. $^1B_2$ states at around 45° and 75° and $^1B_1$ states at around 60°, the two methods yield essentially the same CT ratios. At those region, the corresponding state is always dominated by one configuration. Since this approximation neglects the contributions from other configurations, it underestimates the character mixing at other regions, where the two major configurations contribute equally to the state.

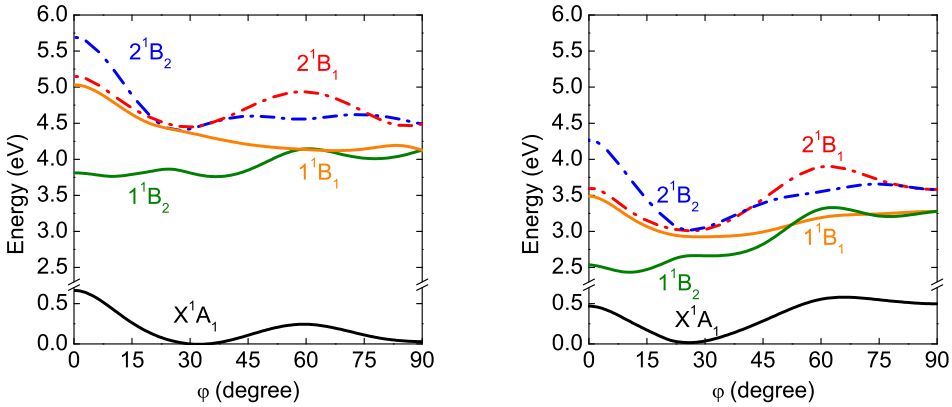

Figure 4.20.: Left: potential energy curves of ground and excited states calculated with the CISD method; Right: potential energy curves of ground and excited states calculated with the SCS-CC2 method.

4.2.5. Application of the model Hamiltonian method

Since Petelenz introduced the model Hamiltonian (MH) method,[23] this method has been widely used for considering exciton and charge transport properties in organic crystals and aggregates.[25,28,29,30,31,64,65] The method has been carefully discussed in section 3.2. We applied this method on the PBI dimers for describing the torsion motion. Necessary integrals were calculated in the CISD(4,4)/SV(P) level of theory. Fig. 4.20 left shows the potential energy curves for ground and excited states calculated with the CISD approach. Compared with SCS-CC2 curves (Fig. 4.20 right), the ground state energy curve of the CISD approach shows the largest difference in the large φ region. As discussed in the work of Zhao *et al.*[91], in the large φ region the dispersion effect for the ground state becomes more important than in the small φ region. Therefore, this difference is expected and vanishes if a better correlation method or semiempirical dispersion corrections are applied. Also, we found a absolute excitation energy difference ($\approx$ 1.2 eV) for all the excited states between the two methods. This is clearly owing to the limited four configuration CI which provides a much less balanced description of the different states than in the SCS-CC2 method. Even though, the CI method still gives a much better description of excited states than TD-HF and TD-DFT methods (see 4.1.3). It is also important to mention that the potential energy curves of the CISD(4,4) method are identical to the ones of the MH method. Because of the symmetry of the states the reference and the doubly excited configurations have no coupling with singly excited configurations.

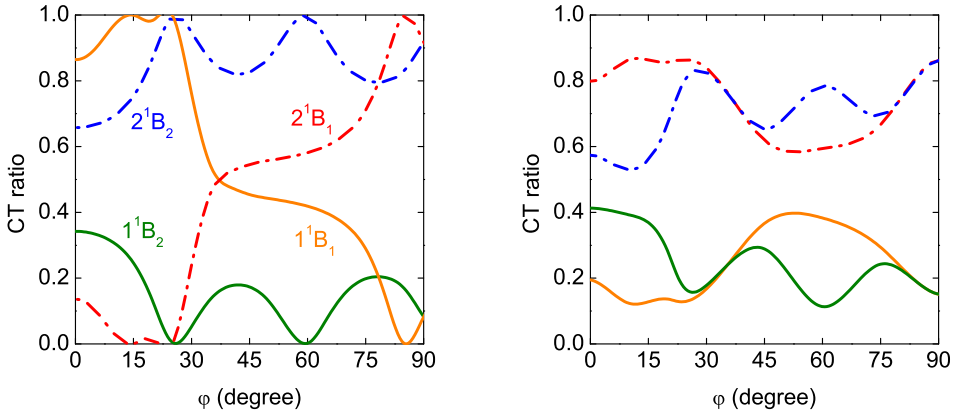

Figure 4.21.: Left: ratio of CT character of excited states based on Model Hamiltonian method results; Right: ratio of CT character of excited states based on SCS-CC2 results.

For the character analysis curves of the MH method (Fig. 4.21 left), we found a character misplacement for $^1B_1$ states in small φ region (0° to 30°). This is because the CISD approach provides a different ordering of these two excited states which are very close in energy. As shown in the left side of Fig. 4.20, this error is only in the order of 0.1 - 0.2 eV which vary still small compared to the expected accuracy of this method. However, the CISD approach works well for $^1B_2$ states as well for $^1B_1$ states in large φ region. Similar to the transition dipole moment approximation (4.19 left), the MH method predicts less admixture of the mixing character of a state when more than two delocalized configurations have significant contributions, e. g. $^1B_2$ states at around 25° and 60° and $^1B_1$ states at around 15° and 75°. Nevertheless, it can describe the case when the excited states possess no oscillator strength, and gives a qualitatively correct picture for excited states.

The character exchange of the two $^1B_1$ states in small φ region can be understood better in the MH method. As shown on the left hand side of Fig. 4.22, the excitation energies of the two degenerate diabatic NE states are of about 0.3 eV constantly lower than the ones of the two degenerate diabatic CT states. According to equation (3.2.21), we introduce a block diagonalization for the MH matrix based to the symmetry of the system. The two degenerate NE states split into two symmetry adapted NE states as well as the two degenerate CT states (Fig. 4.22 right). Due to these splittings, we find that the excitation energies of the NE state with B_1 symmetry is slightly higher than the ones of the CT states

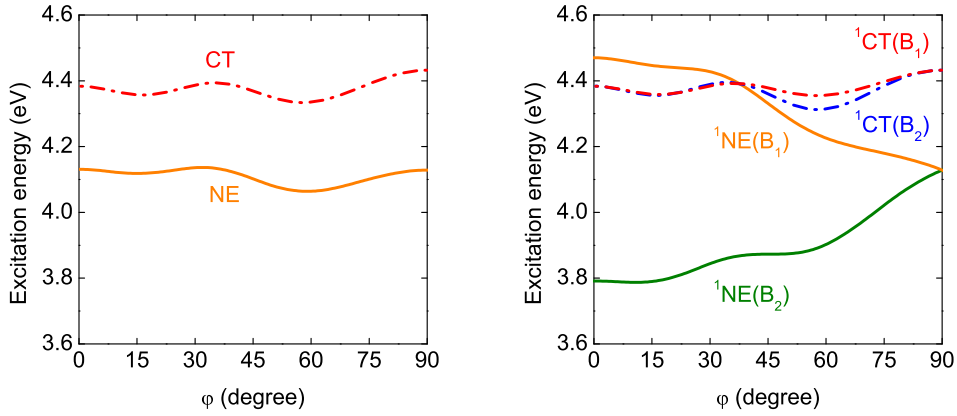

Figure 4.22.: Left: excitation energies of the diabatic NE and CT excited states, where NE represents Ψ_{A^*B} and Ψ_{AB^*} states and CT represents $\Psi_{A^+B^-}$ and $\Psi_{A^-B^+}$ states; Right: excitation energies of the symmetry adapted NE and CT excited states, where ^{1}NE(B$_1$) represents $\frac{1}{\sqrt{2}}(\Psi_{A^*B}-\Psi_{AB^*})$ state, ^{1}NE(B$_2$) represents $\frac{1}{\sqrt{2}}(\Psi_{A^*B}+\Psi_{AB^*})$ state, ^{1}CT(B$_1$) represents $\frac{1}{\sqrt{2}}(\Psi_{A^+B^-}-\Psi_{A^-B^+})$ state and ^{1}CT(B$_2$) represents $\frac{1}{\sqrt{2}}(\Psi_{A^+B^-}+\Psi_{A^-B^+})$ state.

when $\varphi < 35°$. Furthermore, the coupling between the symmetry adapted NE and CT states [equation (3.2.24)] can not change the order them. Therefore, the energetically lower ^{1}B$_1$ state in the small φ region possess majorly CT character.

4.2.5.1. Coupling parameters

As shown in Fig. 4.23, V_{EC} behaves as a cosine function

$$V_{\mathrm{EC}} = -A\cos\varphi, \tag{4.2.13}$$

where A is chosen to be the value of V_{EC} at 0°.
It can be explained with the Förster theory[32]

$$\begin{aligned} V_{\mathrm{EC}} &= \frac{1}{R_{AB}^3}\left(\vec{\mu}_A\cdot\vec{\mu}_B - 3\frac{(\vec{\mu}_A\cdot\vec{R}_{AB})(\vec{R}_{AB}\cdot\vec{\mu}_B)}{R_{AB}^2}\right) \\ &= \frac{1}{R_{AB}^3}\left(\mu_A\mu_B\cos\alpha - 3\frac{(\mu_A R_{AB}\cos\beta)(R_{AB}\mu_B\cos\gamma)}{R_{AB}^2}\right) \\ &= \frac{\mu_A\mu_B}{R_{AB}^3}(\cos\alpha - 3\cos\beta\cos\gamma), \end{aligned} \tag{4.2.14}$$

where α is the angle between transition dipole vectors $\vec{\mu}_A$ and $\vec{\mu}_B$. Since a PBI

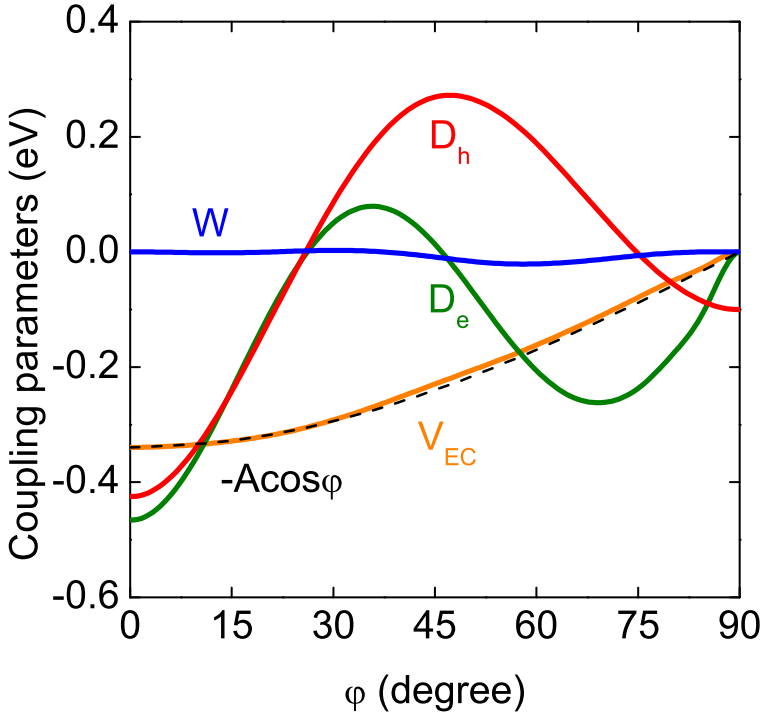

Figure 4.23.: Coupling parameters as functions of torsion angle φ.

monomer transition dipole vector is pointing along the monomer's long axis, [91] α equals the torsion angle φ. β (γ) is the angle between $\vec{\mu}_A$ ($\vec{\mu}_B$) and the distance vector $\vec{R}_{AB}$. As described before, $\vec{R}_{AB}$ is perpendicular to the direction of the transition dipole moments of the monomers, which means β and γ are both equal to 90°. Therefore, equation 4.2.14 is simplified to

$$V_{\mathrm{EC}} = \frac{\mu_A \mu_B}{R_{AB}^3} \cos\varphi. \tag{4.2.15}$$

Considering that the sign in front of V_{EC} is arbitrary, it agrees with the results in Fig. 4.23 perfectly.
As we discussed in the section 3.2.2, the two combined parameter $2(D_e + D_h)$ and $2(D_e - D_h)$ denote the coupling between the symmetry adapted NE and CT states. The larger values of $2(D_e + D_h)$ and $2(D_e - D_h)$ are, the stronger character mixing for the corresponding excited states will be.

We show the excitation energy differences for the four lowest excited states introduced in section 4.2.4 (Fig. 4.24 right), as well as the combined parameter curves of $2(D_e + D_h)$ and $2(D_e - D_h)$ (Fig. 4.24 left). Both curves are almost

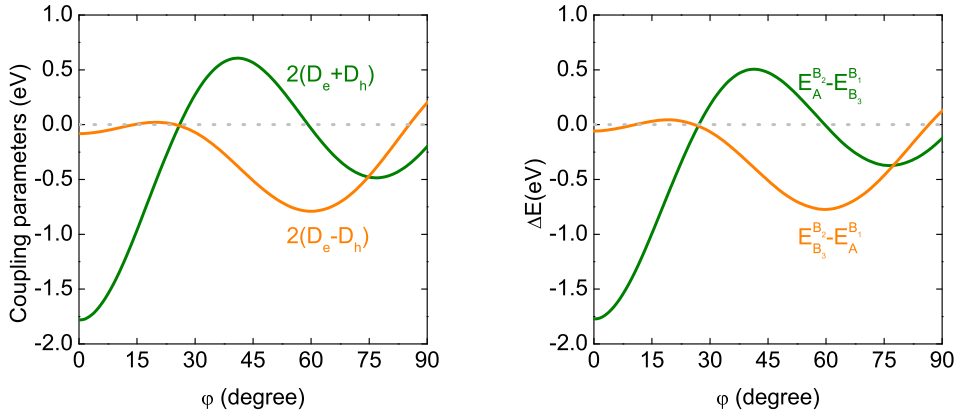

Figure 4.24.: Left: combined coupling parameter curves of $2(D_e + D_h)$ and $2(D_e - D_h)$; Right: excitation energy differences between CI configurations.

identical to each other, which means that

$$\begin{cases} 2(D_e+D_h) \approx E_{\mathrm{A}}^{\mathrm{B}_2} - E_{\mathrm{B}_3}^{\mathrm{B}_1} \\ \qquad\qquad = (\varepsilon_{\mathrm{B}_2} - \varepsilon_{\mathrm{A}}) - (\varepsilon_{\mathrm{B}_1} - \varepsilon_{\mathrm{B}_3}) \\ 2(D_e-D_h) \approx E_{\mathrm{B}_3}^{\mathrm{B}_2} - E_{\mathrm{A}}^{\mathrm{B}_1} \\ \qquad\qquad = (\varepsilon_{\mathrm{B}_2} - \varepsilon_{\mathrm{B}_3}) - (\varepsilon_{\mathrm{B}_1} - \varepsilon_{\mathrm{A}}) \end{cases} \rightarrow \begin{cases} D_e \approx \frac{1}{2}(\varepsilon_{\mathrm{B}_2} - \varepsilon_{\mathrm{B}_1}) \\ D_h \approx \frac{1}{2}(\varepsilon_{\mathrm{B}_3} - \varepsilon_{\mathrm{A}}) \end{cases} . \quad (4.2.16)$$

Thus, the 'electron transfer parameter' D_e is essentially given by the orbital energy difference between LUMO and LUMO+1 of the dimer and the 'hole transfer parameter' D_h is essentially given by the orbital energy difference between the corresponding HOMO and HOMO-1 energy difference. This agrees with equations (3.2.17) and (3.2.18), and the small deviations are due to the two electron integral terms in equations (3.2.7) and (3.2.6). It is worth to note that the differences between Fig. 4.24 right and Fig. 4.18 are due to the different basis sets being used for the calculations.
The last coupling parameter W is the coupling between the diabatic CT states. As shown in Fig. 4.23 left, it is too small, compared to the other parameters, to influence the character of the excited states. Therefore, we refrain to discuss it in detail.

4.2.6. Conclusions

We presented a general method for analyzing the character of excited states that is based on CIS type wavefunctions for aggregates. In this method, the delocalized MOs have been localized to each monomer, then the excited configurations are transformed in the localized basis set. It has been used for analyzing the excited states of PBI aggregates for a translation motion and a torsion motion. This method also helped in understanding the electronic structure of these excited states in aggregate systems. The behaviors of the calculated potential energy curves and the character curves were well explained under a two-configuration approximation. For the translation motion, the CT and NE configurations are energetically close to each other at short distances but well separated at long distances. This leads to stronger character mixing of excited states at short distances and weaker mixing at long distances. For the torsion motion, the behavior of character curves and potential curves are majorly affected by the overlap between the MOs of the two monomers. By introducing an excitation energy difference ΔE, one can qualitatively predict the behavior of these curves.
The character analysis results are also compared with the simplified two-state approximation method. It shows that the simplified method described the character of excited states of the PBI dimer qualitatively correct. The simplified method is essentially good enough to justify the major character of an excited state.
Furthermore, we used the model Hamiltonian method to calculate the PBI dimer system of the CISD(4,4)/SV(P) level of theory. This method shows a surprisingly good agreement with SCS-CC2 results such as the shape of potential energy curves, the excitation energy difference between the NE and CT states and the character analysis. For such a closely contacted π conjugated dimer system, the Förster theory which assumes no overlap between the monomer MOs is still valid. The parameters D_e and D_h) can be approximated as the orbital energy differences. Compared to all these coupling parameters, the coupling between the diabatic CT states is negligible.

4.3. Method and basis set validation for carbon atom K-shell excited states

4.3.1. Introduction

A K-shell core orbital in a molecule is strongly localized on a specific atom, while a valence orbital is generally delocalized and spread over the whole molecule. A core excitation normally results in strong deformations of the corresponding core and valance orbitals. Besides, electronic correlation is always an important issue for an accurate description of the excited states. Different from a valence excitation, the relativistic effect plays a role in considering the core excitation energy. For the second row elements it is less pronounced than for heavier atoms, and gives rise to energy corrections in the order of 0.1 eV. For a given atom, these corrections are essentially independent of the molecular environment.[123]

4.3.2. Computational procedure

We suggested two classes of methods considering these two major effects for the core excited states. The first class of methods, which only consider the orbital deformation effect, employs the *Restricted Open-shell Hatree-Fock* (ROHF) and the *Frozen core approximation* (FCA). For the second class of methods, we chose the *Multi-Configuration Coupled Electron Pair Approximation*[124] (MCCEPA) for considering the electronic correlation effects. For each method, we tested several basis sets. They are varying gradually from non-polarized and non-diffused basis sets to those including polarization and diffuse basis functions.
Strongly decontracted basis sets are used for the core excited atom. They are derived from standard basis sets of Schäfer *et al.* to those including additional primitive Gaussian functions. The exponents of these basis functions in the following texts are given in a. u.:

- Core0 (8s5p2d/[8s5p2d]) is formed by decontracting the standard SV basis set[121] and additionally adding an *s* function (with an exponent 0.1309), a *p* function (with an exponent 0.1527) and two *d* functions (with

exponents 20.00 and 0.5500).

- Core1 (11s8p3d1f/[9s8p3d1f]) is formed by decontracting the standard 11s7p/[6s4p] basis set[125] and additionally adding a *p* function (with an exponent 0.08663), three *d* functions (with exponents 20.00, 1.097 and 0.3180) and an *f* function (with an exponent 0.7610).

- Core2 (11s8p4d2f/[9s8p4d2f]) is formed by decontracting the standard 11s7p/[6s4p] basis set[125] and additionally adding a *p* function (with an exponent 0.08663), four *d* functions (with exponents 20.00, 1.848, 0.6490 and 0.2280) and two *f* functions (with exponents 1.419 and 0.485).

In order to better describe *Rydberg states*, the extended version of those basis sets are used. They include:

- Core0d (9s6p3d/[9s6p3d]) adds a diffuse *s* function (with an exponent 0.04529), a diffuse *p* function (with an exponent 0.04491) and a diffuse *d* function (with an exponent 0.1650) upon the Core0 basis set.

- Core1d (12s9p4d2f/[10s9p4d2f]) adds a diffuse *s* function (with an exponent 0.04444), a diffuse *p* function (with an exponent 0.03257), a diffuse *d* function (with an exponent 0.09220) and a diffuse *f* function (with an exponent 0.2540) upon the Core1 basis set.

- Core2d (12s9p5d3f/[10s9p5d3f]) adds a diffuse *s* function (with an exponent 0.04444), a diffuse *p* function (with an exponent 0.03257), a diffuse *d* function (with an exponent 0.08140) and a diffuse *f* function (with an exponent 0.1670) upon the Core2 basis set.

For other atoms, the standard Aldrich basis sets are used which include SV(P),[121] SVP,[121] TZVP[62] and TZVPP.[62] We tested these methods on CO, CO_2, CH_4,C_2H_2, C_2H_4, HCHO, C_4H_6 and C_6H_5N molecules. Three different kinds of core-hole states are considered: $1s \rightarrow \pi^*$ and $1s \rightarrow$ *Rydberg excited states* as well as core-ionized ones where the core *ionization potential* (IP) was calculated.

4.3.3. Discussion

In the FCA, the ground state wavefunction is first calculated with the RHF method. Then, a specific core hole, with a singly occupied core orbital, is opti-

mized with a ROHF approach. Finally, core excited states are generated by optimizing the virtual orbitals of the former calculation which the occupied orbitals are kept frozen. Thus, the FCA can be taken as a method that partially includes the orbital deformation effect. Compared to the FCA, the ROHF method allows as much orbital relaxation as possible. It starts from the FCA wavefunction. After the core hole is optimized, the 'excited' electron is assigned to a specific virtual orbital. The singly occupied orbital is optimized with the frozen core. Here a special SCF technique is used to prevent the electron falling down to the energetically lower virtual orbitals. Then the core hole and the doubly occupied orbitals are again optimized with the now frozen singly occupied orbital. This is repeated iteratively, until the orbitals are converged. Therefore, for IP calculations, where only the core hole is optimized, FCA and ROHF make no difference. The MCCEPA method considers a major part of the electronic correlation by explicitly considering all correlation effects of the singly and doubly excited configurations and approximate treatment of higher excited configurations. It is by far the best of the three methods.

Table 4.1.: Calculated and experimental carbon K-shell vertical excitation energies and ionization potential (IP) of CO, CO_2, CH_4,C_2H_2, C_2H_4, HCHO, C_4H_6 and C_6H_5N. For each theoretical method, the Core2d-TZVPP basis set is used. All numbers are in eV.

		FCA	ROHF	MCCEPA	exp
CO	$1s \rightarrow 1\pi^*$	289.06	288.00	287.57	287.41 [126]
	$1s \rightarrow 3s$	293.91	293.90	292.97	292.4 [127]
	$1s \rightarrow 3p(\pi)$	294.70	294.69	293.87	293.3 [127]
	$1s \rightarrow 3p(\sigma)$	294.83	294.82	294.08	293.5 [127]
	IP	297.06		296.38	296.1 [127]
CO_2	$1s \rightarrow 1\pi^*$	293.01	291.92	291.20	290.77 [128]
	$1s \rightarrow 3s$	295.10	294.94	293.00	292.74 [128]
	$1s \rightarrow 3p(\pi)$	296.99	296.98	295.54	294.96 [128]
CH_4	$1s \rightarrow 3s$	287.38	287.39	287.00	287.03 [129]
	$1s \rightarrow 3p(\pi)$	288.48	288.46	288.26	287.98 [129]

Table 4.1.: (continued)

		FCA	ROHF	MCCEPA	exp
C_2H_2	$1s \rightarrow \pi^*$	287.21	286.35	286.02	285.81 [127]
	$1s \rightarrow 3s$	288.56	288.54	288.19	287.74 [127]
	$1s \rightarrow 3p(\pi)$	288.77	288.74	288.32	288.76 [127]
	$1s \rightarrow 3p(\sigma)$	289.37	289.36	289.10	288.8 [130]
C_2H_4	$1s \rightarrow \pi^*$	284.44	285.28	284.34	284.7 [128]
HCHO	$1s \rightarrow 1\pi^*$	286.01	285.02	284.57	285.590 [131]
	$1s \rightarrow 3a(A_1)$	291.30	291.44	290.62	290.178 [131]
	$1s \rightarrow 3p(B_2)$	292.13	292.39	291.56	291.253 [131]
	$1s \rightarrow 3p(B_1)$	292.40	292.42	291.71	291.729 [131]
	IP	294.80		294.49	294.352 [131]
C_4H_6	$C_t 1s \rightarrow 1\pi^*$	286.72	285.34	285.05	285.07 [132]
	IP(C_t)	290.65		290.73	290.87 [132]
	$C_m 1s \rightarrow 1\pi^*$	286.01	285.02	284.57	284.41 [132]
	IP(C_m)	289.88		290.09	290.23 [132]
C_6H_5N	$C_{orth} 1s \rightarrow 1\pi^*$	287.31	286.55	285.97	285.2 [133]
	$C_{orth} 1s \rightarrow 2\pi^*$	288.65	288.01	286.90	286.1 [133]
	IP(C_{orth})	291.35		291.34	291.1 [133]
	$C_{meta} 1s \rightarrow 1\pi^*$	286.75	285.97	285.43	284.8 [133]
	$C_{meta} 1s \rightarrow 2\pi^*$	287.74	286.98	286.02	285.5 [133]
	IP(C_{meta})	290.43		290.63	290.5 [133]
	$C_{para} 1s \rightarrow 1\pi^*$	286.71	285.92	285.41	284.7 [133]
	$C_{para} 1s \rightarrow 2\pi^*$	288.54	287.93	286.80	286.0 [133]
	IP(C_{para})	290.98		290.98	290.8 [133]
Mean absolute errors					
$1s \rightarrow \pi^*$		1.91	1.03	0.44	
Rydberg states		1.10	1.11	0.40	

Table 4.1.: (continued)

	FCA	ROHF	MCCEPA	exp
IP	0.35		0.18	
All types	1.26	0.91	0.37	

In table 4.1 the calculated excitation energies and the corresponding experimental data listed, for all the methods with the largest basis sets used in this work. Also the mean absolute errors of all methods for different types of transitions are listed bellow. The results show that all three methods give qualitatively correct excitation energies. For $1s \rightarrow \pi^*$ type transitions, the ROHF results (mean absolute error of 1.03 eV) are significantly more accurate than those of the FCA approach ones (mean absolute error of 1.91 eV) and MCCEPA (mean absolute error of 0.44 eV) further improves the ROHF results. This shows that for $1s \rightarrow \pi^*$ type transitions, the orbital relaxation and electronic correlation are both important. For *Rydberg states*, the ROHF shows no better performance than FCA that the mean absolute values of both methods are around 1.1 eV. Since for *Rydberg states* the singly occupied orbital are rather far away from the other orbitals, further optimization on the orbitals does not lead to significant improvements of the wavefunction, because it is already well described within the FCA approach. However, the electronic correlation effect (about 0.71 eV in average) is still very important and should not be neglected for such transitions. For IP calculations, the FCA and ROHF results are identical and both are very close (mean absolute error of 0.35 eV) to the experimental data. With electronic correlation effects, the mean error is reduced to 0.18 eV. All together, MCCEPA is an excellent method for calculating *C* K-shell excited states and provides mean absolute error of only 0.37 eV. It proves that electronic correlation is an important factor for core excitation energies. The orbital relaxation is important for $1s \rightarrow \pi^*$ type transitions, however, less important for *Rydberg states*.

Similar to the methods, the basis set requirements vary for the different transition types. For $1s \rightarrow \pi^*$ transitions of the given molecules, Fig. 4.25 plotted the basis set dependence for all the three methods. In the first box (Fig. 4.25) where the Core0-SV(P) basis set was used, the 12 different $1s \rightarrow \pi^*$ transitions have been calculated. The FCA results show a error range from 1.7 to 2.8 eV. As discussed before, we find a clear improvement for the ROHF results (from 0.4

Figure 4.25.: Basis set dependence of $1s \rightarrow \pi^*$ excitation energy errors between the experimental data and calculated results of FCA, ROHF and MCCEPA methods. From the first box to the last one, the Core0-SV(P), Core0-SVP, Core1-SVP, Core1-TZVP, Core2-TZVP and Core2-TZVPP basis sets are used, respectively. In each box, the black curve with square points is calculated by FCA and each point is corresponding to a excited state which is listed in the first box. The red curve with round points is the ROHF one and the blue curve with triangle points is calculated with MCCEPA.

to 2.2 eV). The MCCEPA results are generally a little bit better than the ROHF ones. For the second π^* states of pyridine, the improvements from the MCCEPA are large which is because for these states the electronic correlation effects are stronger than the lower ones. In the second box where the Core0-SVP basis set was used, it only improves the description of H atoms compared to the Core0-SV(P) basis set. Therefore, we found very similar trends for the curves but no clear improvement. In the third box we used Core1-SVP basis set. Compared to the Core0-SVP basis set, several polarization functions have been added for describing the core excited carbon atom. We find that the error of the MCCEPA method is much smaller than the one with the smaller basis set. However, for the FCA and ROHF approaches, there are only small errors reductions. For the latter three boxes, we found no big change of the error curves of FCA and ROHF. The improvement for MCCEPA is not too much as well. Thus, we can conclude that, for $1s \rightarrow \pi^*$ transitions, the performance of FCA and ROHF is much less dependent on the basis set than MCCEPA. Also, the change of the basis set of the core hole atom is more important than an improvement on the other atoms. For *Rydberg* type transitions, 8 basis sets have been compared for the three methods applied on five different excited states of HCHO and CO, respectively (Fig. 4.26). In the first box, the Core1-SVP basis set was used. We found that the ROHF results are almost not improvement to the FCA ones. This behavior holds true for all basis sets. As we discussed before, a Rydberg orbital has its largest density in a region where the valence electron density is small. Thus, *Rydberg states* show only a weak interaction between the valence and Rydberg orbitals. Therefore, further relaxation for these orbitals will neither lower the orbital energy nor change the core hole energy. In the second box, where the Core1-TZVP basis set was used, the errors of all the three methods were reduced about 0.5 eV. This can be understood as that Rydberg orbital was poorly described with Core1-SVP basis set and with large percent of the oxygen components. Therefore, the energy of Rydberg orbital is lowered by the Core1-TZVP basis set, since it includes several more polarized *s* and *p* functions at the oxygen atom. In the third and forth boxes, the results didn't change too much because the increased functions have no big contribution on describing Rydberg orbitals. In the fifth box, we used the Core0d-SV(P) basis set, which is one of the smallest basis sets through all the calculations. However, the results are surprisingly good. The main reason is that an *s*, a *p* and a *d* diffuse functions are included in the basis set. Thus, Rydberg orbital was for the first time correctly described. The sixth box again further

Figure 4.26.: Basis set dependence of *Rydberg state* excitation energy errors between the experimental data and calculated results of FCA, ROHF and MCCEPA methods. From the first box to the last one, the Core1-SVP, Core1-TZVP, Core2-TZVP, Core2-TZVPP, Core0d-SV(P), Core1d-TZVP, Core2d-TZVP and Core2d-TZVPP basis sets are used, respectively. In each box, the black curve with square points is calculated by FCA and each point is corresponding to an excited state which is listed in the first box. The red curve with round points is the ROHF one and the blue curve with triangle points is calculated with MCCEPA.

modified Rydberg orbital and the error is further reduced. Later basis sets have no more significant improvement on the error curves which did not change too much as well. For all excitation energy errors in Fig. 4.26, the MCCEPA curves are always about 0.5 eV lower than the FCA and ROHF ones which means the electronic correlation is a constant effect for Rydberg orbitals. The last type of core excitation is the IP where the core electron is completely kicked out of the molecule. The energy of the core hole is the energy of the corresponding 'excited states'. As mentioned before, FCA and ROHF provides the same results for the core hole energy. Therefore, in Fig. 4.27 we only plotted the curves of the FCA and MCCEPA. Different from the last two types of transitions, both methods gave almost equally good IPs. As usual that the errors decrease if a large basis set is used. Since the MCCEPA method includes electronic correlation effect, it gives a little bit better results than the FCA approach.

4.3.4. Conclusion

We compared the method- and basis set dependence for a series of C K-shell excitation energies. The results show that for C $1s \rightarrow \pi^*$ type transitions, the relaxation for core hole and the virtual orbital is very important. This may provide 0.9 eV excitation energy error in average. The electron correlation effect (in MCCEPA) gave about 0.6 eV correction upon the ROHF results. Different basis sets for this type of transition had no obvious influence on the FCA and the ROHF, but for MCCEPA. A better basis set for the core hole improves the results. For *Rydberg* type transitions, since the core hole and Rydberg orbital have very weak coupling, the FCA and the ROHF approaches always give similar results. The MCCEPA provided about 0.5 eV correction due to the electronic correction effect. We also found that the diffuse functions are absolutely necessary for a proper basis set. For some expensive calculations, one could reduce several polarized functions but should always include diffuse functions.
Finally, for the IP calculations, the performance of the much cheaper FCA was more or less equally good as the ones of the much more expensive MCCEPA. A better basis set would improve the results but the improvement is limited.

Figure 4.27.: Basis set dependence of *ionization potential* energy errors between the experimental data and calculated results of FCA and MCCEPA methods. From the first box to the last one, the Core0-SV(P), Core0-SVP, Core1-SVP, Core1-TZVP, Core2-TZVP and Core2-TZVPP basis sets are used, respectively. In each box, the black curve with square points is calculated by FCA and each point is corresponding to an excited state which is listed in the first box. The red curve with round points is calculated with MCCEPA.

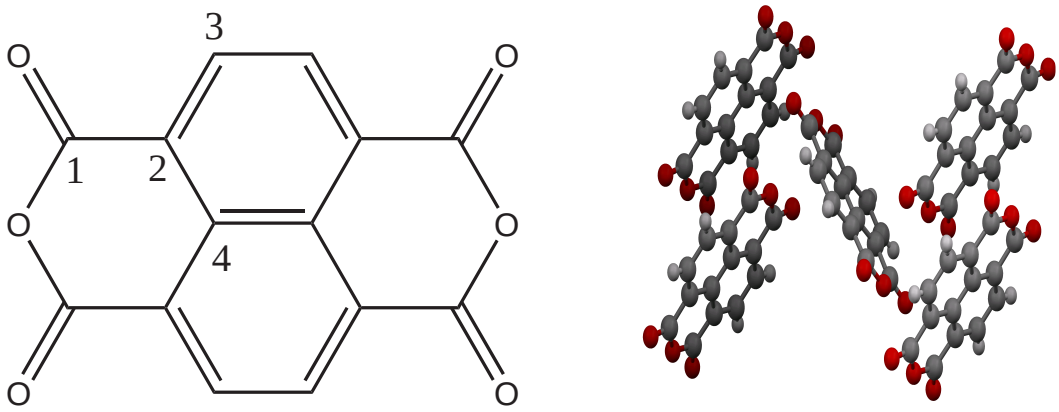

Figure 4.28.: Left: the planar naphthalene tetracarboxylic dianhydride (NTCDA) moiety, and lables besides C atoms specify different types due to the symmetry; Right: the crystal structure of NTCDA (view along a-axis).

4.4. Davydov splitting effects in the core excited states of NTCDA

4.4.1. Introduction

The splitting of electronic terms due to a crystalline surrounding is intimately connected with the name of A. S. Davydov since his 1948 landmark paper on this effect in naphthalene tetracarboxylic dianhydride (NTCDA) crystal.[134] The effect has been thoroughly investigated.[37,135,136,137,138] It is now well established, that the energy splitting of excited state levels is up to the order of magnitude of 0.5 eV.[96] One characteristic feature of *Davydov splittings* is that they have so far only be confirmed for excitations in the visible and near UV region . Here the effect has been shown to be strongly connected to energy transfer, where the Förster mechanism was shown to play a major role for the actual size of the observed splitting.

Very recently Holch *et al.* managed to measure highly resolved NEXAFS spectra of naphthalene tetracarboxylic dianhydride (NTCDA) crystals (Fig. 4.28) with a resolution that allows to disentangle splittings in the order of 0.1 eV. Actually the measured spectra also showed unexpected and unprecedented effects in this order of magnitude. As further information was not available, a Davydov splitting effect was proposed as one possible explanations for the observed effect. On

Table 4.2.: Calculated absolute transition dipole moments $|\mu|$, vertical excitation energies ΔE and oscillator strengths f of different C atoms in the NTCDA monomer (Fig. 4.28 left) with FCA/cc-pVTZ (in parenthesis cc-pVDZ) level of theory.

excitation	$\|\mu\|$ (a. u.)	ΔE (eV)	f (a. u.)
$C_1 : 1s \rightarrow 1\pi^*$	0.0687(0.0676)	290.7439(292.5815)	0.0337(0.0328)
$C_1 : 1s \rightarrow 2\pi^*$	0.0456(0.0454)	292.9147(294.7869)	0.0150(0.0149)
$C_2 : 1s \rightarrow 1\pi^*$	0.0583(0.0564)	286.2547(288.0030)	0.0238(0.0224)
$C_2 : 1s \rightarrow 2\pi^*$	0.0251(0.0248)	288.6115(290.4266)	0.0044(0.0044)
$C_2 : 1s \rightarrow 5\pi^*$	0.0357(0.0364)	292.1798(294.0684)	0.0091(0.0096)
$C_3 : 1s \rightarrow 1\pi^*$	0.0609(0.0589)	286.1957(288.0160)	0.0260(0.0245)
$C_3 : 1s \rightarrow 2\pi^*$	0.0453(0.0436)	288.1910(290.0549)	0.0145(0.0135)
$C_3 : 1s \rightarrow 4\pi^*$	0.0193(0.0189)	290.6524(292.5571)	0.0026(0.0025)
$C_3 : 1s \rightarrow 1\sigma^*$	0.0403(0.0447)	291.3615(293.7681)	0.0116(0.0144)
$C_4 : 1s \rightarrow 2\pi^*$	0.0760(0.0739)	287.8124(289.5649)	0.0407(0.0387)
$C_4 : 1s \rightarrow 5\pi^*$	0.0268(0.0253)	292.2924(294.1922)	0.0052(0.0046)

the other hand, the geometry deformation of the monomer and the interactions with neighboring molecules may contribute to this effect.

4.4.2. NEXAFS SPECTRA OF NTCDA MONOMER

In the last section, we tested three different methods on calculating C K-shell excited states. The best choice for calculating these kind of excited states would be the most expensive MCCEPA. However, for the rather extended NTCDA these calculations turns out to be too cumbersome. Even for the ROHF approach, only the first excited state could be calculated. Thus, we chose the FCA method because it is much more robust and provides qualitatively correct excitation energies for core excited states. Since, this method is less sensitive to the basis set, we took the standard cc-pVTZ and cc-pVDZ basis sets for all the core excited states calculations. All calculations were performed with the WAVELS program package.[122]

Table 4.2 listed the FCA/cc-pVTZ and FCA/cc-pVDZ results of transition dipole moments ($|\mu|$), excitation energies (ΔE) and oscillator strengths (f) for all the core excited states with significant transition dipoles ($|\mu| > 0.01$ a. u.). We found

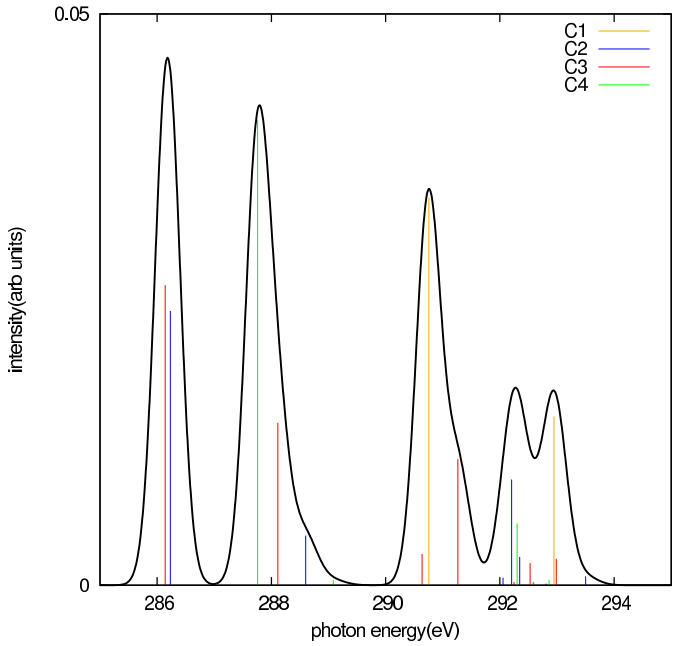

Figure 4.29.: Calculated NEXAFS spectra for the planner monomer in gas phase.

a rather constant shift to lower excitation energies (1.6 - 1.9 eV) for $1s \rightarrow \pi^*$ type transitions of the FCA/cc-pVTZ results compared to the FCA/cc-pVDZ ones. For the only $1s \rightarrow \sigma^*$ transition, a shift of 2.4 eV was obtained. The transition dipole moments and oscillator strengths of all excited states were quite similar at both levels of theory. The spectra are generated as Gaussian convolutions of the stick spectra resulting from the calculated oscillator strengths and excitation energies (Fig. 4.29). They compare well with the experimental ones (Fig. 4.30 (1)), but show a blue shift of about 1.9 eV. The calculations allow to assign the α peak in Fig. 4.30 (1) to the two first excitations of C_2 and C_3. The β peak stems mostly from the second excitation of C_4 and partially from the second excitation of C_3. The γ peak is more complicated and it contains the first and second excitations of C_1, the forth and fifth ($1s \rightarrow 1\sigma^*$) excitations of C_3 and the fifth excitations of C_2 and C_4.

In the gas phase the NTCDA monomer has a planer structure, but in the condensed phase the structure is distorted due to the crystal surrounding. The symmetry of the monomer decreases from D_{2h} for the gas phase to C_i for the condensed phase. Furthermore, it is well known that the positions of H atoms are uncertain in the X-ray structures. Therefore, we took the monomer structure out of the condensed phase structure and partially optimized the geometry by fixing all heavy atoms. The optimization is performed with the B3LYP [49,51,53,56,57]

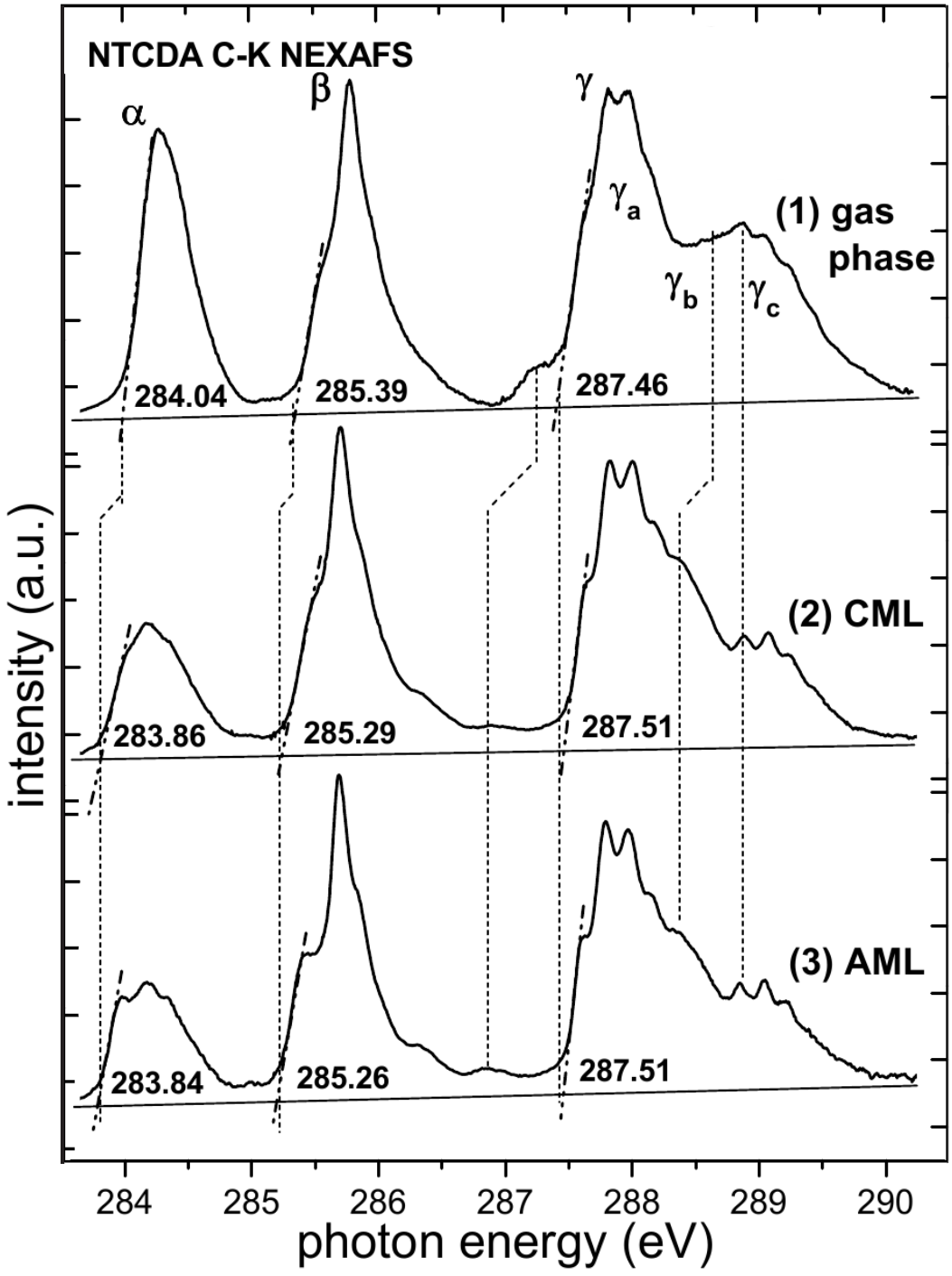

Figure 4.30.: NEXAFS spectra of NTCDA (1), in gas phase (2), in condensed cold multilayer (3), after annealing.

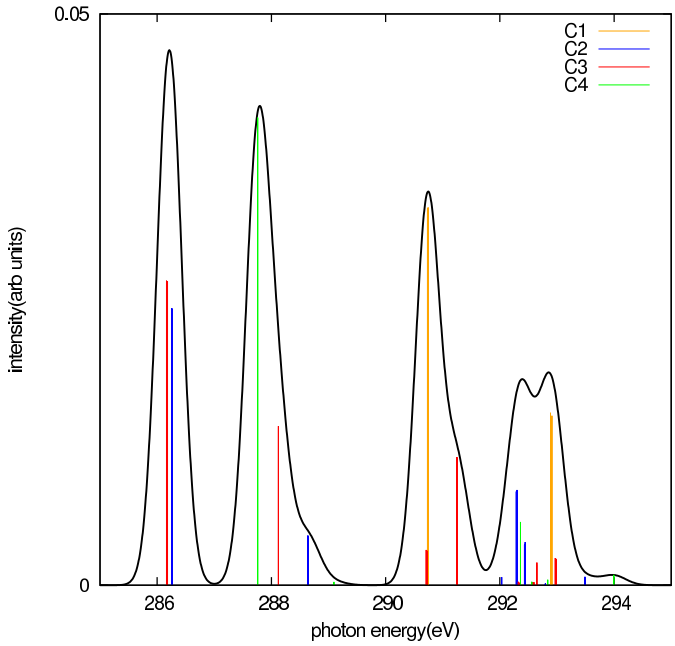

Figure 4.31.: Calculated NEXAFS spectra for the distorted monomer in the NTCDA crystal.

functional and the TZVP basis sets [62] using the TURBOMOLE 6.0 program package. [100] Based on the optimized monomer structure, we calculated the core excited states for all C atoms and plotted the spectra in the same way as shown in Fig. 4.31. Compared to the phase spectra, we found very small energy shifts in the order of 5 - 30 meV. This effect is too small to explain the observed red shifts of the experimental spectra.

4.4.3. Davydov splitting

The Davydov splitting effects are often found for excited states in the visual and ultra-violet regions. [134,135] However in X-ray spectroscopy, this effect has never been evaluated before. Therefore, we put through our method to calculate the Davydov splitting effects for core excited spectra.

As shown in Fig. 4.32, the two degenerate localized excited states Φ_A and Φ_B, which refer to excitations at the monomers A and B, respectively, split into two delocalized excited states Φ_+ and Φ_-. Each core hole gives rise to a series of excited states. These excited states share the same set of orthonormalized MOs. On the other hand, different sets of MOs will be used for excited states which do not share the same core hole. In general, different sets of MOs are not

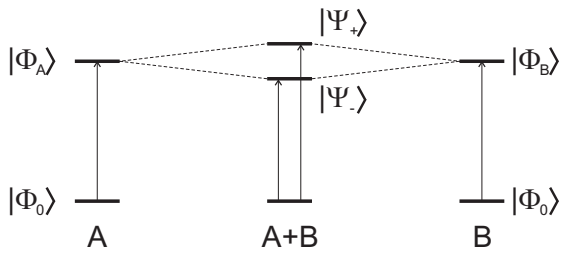

Figure 4.32.: Energy diagram of Davydov splitting.

orthogonal to each other. Hence, we give the explicit expression for the localized excited states Φ_A and Φ_B as follows

$$\Phi_A = \frac{1}{\sqrt{2}}\left(a_i^\dagger a_a + a_{\bar{i}}^\dagger a_{\bar{a}}\right)\Phi_{0(A)}, \tag{4.4.1}$$

$$\Phi_B = \frac{1}{\sqrt{2}}\left(\tilde{a}_i^\dagger \tilde{a}_a + \tilde{a}_{\bar{i}}^\dagger \tilde{a}_{\bar{a}}\right)\Phi_{0(B)}. \tag{4.4.2}$$

Φ_A and Φ_B can also be denoted as $\Phi^i_{a(A)}$ and $\Phi^i_{a(B)}$ since both refer to excitations from occupied orbital a to virtual orbital i. $a_i^\dagger$ and $a_{\bar{i}}^\dagger$ are the creation operators for monomer spatial orbital i with α and β spin, respectively. a_a and $a_{\bar{a}}$ are the annihilation operators for monomer spatial orbital a with α and β spin, respectively. The same definitions hold for $\tilde{a}_a^\dagger$, $\tilde{a}_i$, $\tilde{a}_{\bar{a}}^\dagger$ and $\tilde{a}_{\bar{i}}$, but they refer to a different set of MOs. $\Phi_{0(A)}$ and $\Phi_{0(B)}$ are the ground state wavefunctions of monomer A and B, respectively. For instance, $\Phi_{0(A)}$ is given as

$$\Phi_{0(A)} = \sum_{i=1}^{n} \hat{a}_i^\dagger |0\rangle = |\hat{\chi}_1 \hat{\chi}_2 \cdots \hat{\chi}_n\rangle. \tag{4.4.3}$$

$|\hat{\chi}_1, \hat{\chi}_2, \cdots \hat{\chi}_n|$ is another set of orthonormalized spin orbitals than the ones used in excited states. $\hat{a}_i^\dagger$ is the corresponding creation operator for spin orbital $\hat{\chi}_i$. Then, the interaction effects can be written into a matrix equation

$$\begin{pmatrix} H_{aa} & H_{ab} \\ H_{ba} & H_{bb} \end{pmatrix}, \tag{4.4.4}$$

where

$$H_{aa} = \langle \Phi^i_{a(A)} | \hat{\mathbf{H}} | \Phi^i_{a(A)} \rangle, \tag{4.4.5}$$

$$H_{ba} = \langle \Phi^i_{a(B)} | \hat{\mathbf{H}} | \Phi^i_{a(A)} \rangle, \tag{4.4.6}$$

$$H_{ab} = \langle \Phi^i_{a(A)} | \hat{\mathbf{H}} | \Phi^i_{a(B)} \rangle, \tag{4.4.7}$$

$$H_{bb} = \langle \Phi^i_{a(B)} | \hat{\mathbf{H}} | \Phi^i_{a(B)} \rangle. \tag{4.4.8}$$

Since A and B are identical monomers, H_{aa} is equal to H_{bb} as well as for H_{ba} and H_{ab}. By diagonalizing the matrix in equation (4.4.4), we get the expressions and energies of the two dimer excited states Φ_+ and Φ_-

$$\Psi_\pm = \frac{1}{\sqrt{2(1 \pm S)}} (\Phi^i_{a(A)} \pm \Phi^i_{a(B)}), \tag{4.4.9}$$

$$E_\pm = \frac{H_{aa} \pm H_{ab}}{1 \pm S}. \tag{4.4.10}$$

S is the overlap between $\Phi^i_{a(A)}$ and $\Phi^i_{a(B)}$

$$S = \langle \Phi^i_{a(A)} | \Phi^i_{a(B)} \rangle. \tag{4.4.11}$$

The commonly used parameter related to the Davydov splitting is the electronic coupling parameter J which is half of the energy difference of E_+ and E_-

$$J = \frac{E_+ - E_-}{2} = \frac{H_{ab} - H_{aa}S}{1 - S^2}. \tag{4.4.12}$$

For $1s \rightarrow \pi^*$ type transitions, S is normally close to 0. Therefore, equation (4.4.12) can be simplified as

$$J \approx H_{ab} - H_{aa}S \approx H_{ab}. \tag{4.4.13}$$

Since S is negligible, H_{ab} can be written as the interaction of transition densities $P(\mathbf{r})$ of local excited states [66]

$$J \approx H_{ab} \approx \int d\mathbf{r}_1 d\mathbf{r}_2 P_A(\mathbf{r}_1) \frac{1}{r_{12}} P_B(\mathbf{r}_2). \tag{4.4.14}$$

$\mathbf{r}_1$ and $\mathbf{r}_2$ are the spatial coordinates of electron 1 and 2, respectively. $\frac{1}{r_{12}}$ is the two-electron operator. P_A and P_B are the transition densities of local excitations on monomer A and B, respectively. For instance, considering an excited state

which has the form

$$\Phi_{ex} = |\chi_1 \chi_2 \cdots \chi_n\rangle, \tag{4.4.15}$$

the corresponding transition density P, according to Löwdin's definition,[69] is given as

$$\begin{aligned} P &= n \int d\sigma_1 \cdots d\sigma_n d\mathbf{r}_1 \cdots d\mathbf{r}_n \Phi_0^* \Phi_{ex} \\ &= \sum_{k,l}^{n} (-1)^{k+l} \int \hat{\chi}_k^* \chi_l d\sigma_1 \cdot \underbrace{\langle \hat{\chi}_1 \hat{\chi}_2 \cdots \hat{\chi}_n}_{no\ \hat{\chi}_k} | \underbrace{\chi_1 \chi_2 \cdots \chi_n \rangle}_{no\ \chi_l} \\ &= \sum_{k,l}^{n} (-1)^{k+l} \cdot T_{kl} \int \hat{\chi}_k^* \chi_l d\sigma_1. \end{aligned} \tag{4.4.16}$$

$d\sigma_1, \cdots d\sigma_n$ are the spin coordinates for each electron respectively. Φ_0 is the ground state wavefunction and we take the form in equation (3.3.1). $|\chi_1, \chi_2, \cdots \chi_n|$ is a set of orthonormalized spin orbitals of the excited state Φ_{ex}. T_{kl} is one matrix element of the so called 'Transition density matrix' $\mathbf{T}$, and it equals the scalar product of the bra and ket vectors

$$T_{kl} = \underbrace{\langle \hat{\chi}_1 \hat{\chi}_2 \cdots \hat{\chi}_n}_{no\ \hat{\chi}_k} | \underbrace{\chi_1 \chi_2 \cdots \chi_n \rangle}_{no\ \chi_l}. \tag{4.4.17}$$

Since the two sets of MOs which are used for ground and excited states are not orthogonal to each other, T_{kl} equals the cofactor of the matrix element $\langle \hat{\chi}_k | \chi_l \rangle$ in the overlap matrix $\mathbf{S}$ between the ground and the excited states. The matrix $\mathbf{T}$ is just the adjugate matrix of the matrix $\mathbf{S}$. We used the modified Gauss-Elimination algorithm (section 3.3.2) to calculate the adjugate matrix of $\mathbf{S}$. There are also many related works[139,140,141,142,143] on the evaluation of matrix elements for non-orthogonal MOs.

As the Davydov splitting is a strong function of the distance (r) between two exciton centers ($J \propto \frac{1}{r^3}$), we calculated the Davydov splitting only for the two nearest monomers in the NTCDA crystal (Fig. 4.33). As a comparison, we also calculated J values by using the transition dipole-dipole approximation introduced by Förster[66] [equation (4.2.14)].
The calculated J values with the largest absolute values are collected in table 4.3. They are calculated in the FCA/cc-pVDZ level of theory. However, the calculated Davydov splitting effects have only small absolute values (< 0.44 meV) which

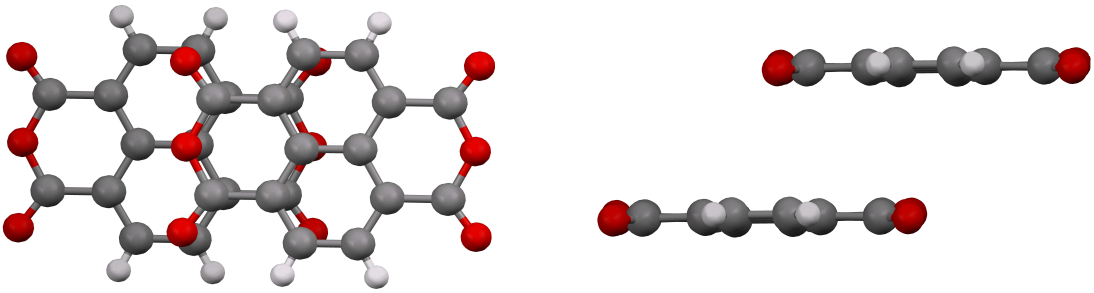

Figure 4.33.: Selected dimer structures of NTCDA for evaluating the Davydov splitting effect. Left: a view along an axis which is perpendicular to both monomer planes; Right: a view along an axis which is parallel to both monomer planes.

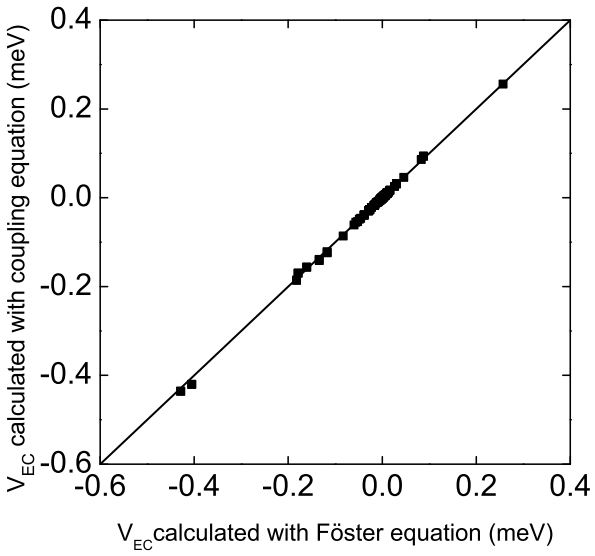

Figure 4.34.: Comparison between the results of Förster' transition dipole-dipole interaction equation and ones of the coupling equation.

is even much smaller than the geometry deformation effects. The comparison between these results and the ones calculated by the Förster's transition dipole-dipole equation (Fig. 4.34) showed that the two methods gives practically identical results.

Based on the idea of the Förster's transition dipole-dipole interaction equation, the exciton coupling parameter is proportional to the product of the two monomer transition dipole moments. For our core excitations, the largest product in our calculations is in the order of 0.005 a. u. Compared to the valance excitations (see Fig. 4.3), these value are about 3000 times smaller for the core

Table 4.3.: Calculated Davydov splitting effects for the NTCDA monomer exciton pairs. Only a single number is given for symmetry equivalent excitations.

exciton pair	J(meV)
$C2_1^A \rightarrow 1\pi^*$ / $C2_3^B \rightarrow 1\pi^*$ $C2_2^A \rightarrow 1\pi^*$ / $C2_4^B \rightarrow 1\pi^*$	-0.436
$C1_1^A \rightarrow 1\pi^*$ / $C1_3^B \rightarrow 1\pi^*$ $C1_2^A \rightarrow 1\pi^*$ / $C1_4^B \rightarrow 1\pi^*$	-0.420
$C1_1^A \rightarrow 2\pi^*$ / $C1_3^B \rightarrow 2\pi^*$ $C1_2^A \rightarrow 2\pi^*$ / $C1_4^B \rightarrow 2\pi^*$	-0.185
$C2_1^A \rightarrow 3\pi^*$ / $C2_3^B \rightarrow 3\pi^*$ $C2_2^A \rightarrow 3\pi^*$ / $C2_4^B \rightarrow 3\pi^*$	-0.170
$C3_1^A \rightarrow 1\pi^*$ / $C3_3^B \rightarrow 1\pi^*$ $C3_2^A \rightarrow 1\pi^*$ / $C3_4^B \rightarrow 1\pi^*$	-0.156
$C1_2^A \rightarrow 1\pi^*$ / $C1_3^B \rightarrow 1\pi^*$	-0.141
$C2_2^A \rightarrow 1\pi^*$ / $C2_3^B \rightarrow 1\pi^*$	-0.139
$C1_1^A \rightarrow 1\pi^*$ / $C1_4^B \rightarrow 1\pi^*$	-0.124
$C2_1^A \rightarrow 1\pi^*$ / $C2_4^B \rightarrow 1\pi^*$	-0.121
$C2_1^A \rightarrow 2\pi^*$ / $C2_3^B \rightarrow 2\pi^*$ $C2_2^A \rightarrow 2\pi^*$ / $C2_4^B \rightarrow 2\pi^*$	0.086
$C3_1^A \rightarrow 2\pi^*$ / $C3_3^B \rightarrow 2\pi^*$ $C3_2^A \rightarrow 2\pi^*$ / $C3_4^B \rightarrow 2\pi^*$	0.094
$C4_1^A \rightarrow 1\pi^*$ / $C4_2^B \rightarrow 1\pi^*$	0.256

excited states. Therefore, the Davydov splitting is generally not an important effect for core excited states.

4.4.4. Conclusion

We calculated the NEXAFS spectra of the NTCDA monomer at the FCA/cc-pVTZ and FCA/cc-pVDZ levels of theories. The calculated spectra reproduce the main features of the experimental spectra correctly. However, as expected, the FCA results overestimated the excitation energies for about 1.9 eV with cc-pVTZ basis set and for about 3.8 eV if the cc-pVDZ basis sets are employed.

In the experiment, a red shift of about 0.1 eV was found for the NEXAFS spectra of NTCDA in the condensed phase when compared with the ones in the gas phase. One possible explanation may be the geometry deformation which is caused by the surrounding molecules. Our calculations show that this effect introduces energy splittings up to 30 meV as compared to the gas phase spectra,

which does not explain the 0.1 eV red shift found in the experiments.
Another possible explanation is the Davydov splitting. We proposed an algorithm for calculating this effect where non-orthogonal MOs are used for the ground and excited states. The calculated Davydov splitting agreed perfectly with the ones calculated with Förster theory. However, the largest absolute value was still less than 0.5 meV. This showed that the Davydov splitting is generally negligible for core excited states.

CHAPTER 5

SUMMARY

We used theoretical approaches to investigate character and properties of valence and core excited states for aggregates of large π-conjugated molecules.
The PBI dimer is chosen as an example for the valence excited states. We tested several excited state methods such as SCS-CC2, TD-HF and TD-DFT with different functionals for a torsion motion of the PBI dimer. The most accurate method among them, SCS-CC2, is taken as reference. A simplified characters analysis is proposed based on the transition dipole moments of the excited states. It provides qualitatively correct descriptions of the characters for the lowest four excited states of the PBI dimer and allows to judge the performance of TD-HF and TD-DFT with different functionals. We found that the TD-HF method gives correct energy order for the lowest four excited states. Furthermore, the shapes of the potential energy curves are very similar to the ones obtained with SCS-CC2. For pure GGA functionals, e. g. BLYP and PBE, the energetic order of the lowest eight excited states are completely mixed. Additionally the potential energy curves of these excited states are wrong. For the hybrid GGA functionals, e. g. B3LYP, PBE and BHLYP, provide improved descriptions for the excited states. The potential energy curves of the lowest four excited state have similar shapes as the SCS-CC2 ones. However, the energetic order of the lowest NE and CT states are exchanged, these potential energy curves lead to incorrect conclusions. We also used a long-range corrected (LC) functional, CAM-B3LYP, to predict the excited states of PBI dimer, but it gives essentially identical results as BHLYP.
We proposed a more general character analysis method for aggregated systems. It is based on a CIS type wavefunction with orbitals that are localized on the

single molecules of the aggregate. The CIS wavefunction is transformed into the basis of the localized orbitals which allows to evaluate the amount of pure NE or CT configurations, such that one can determine the character of the excited state. This analysis is applied on a translation motion and the torsion motion of the PBI dimer. It is explained in a two-state approximation and shown that the character mixing of an excited state can be explained by the excitation energy difference ΔE of the two excited configurations which dominate the excited state. In the model Hamiltonian (MH) approach, these energies can be understood in terms of electron- and hole-transfer parameters. The MH method is derived in a CI picture which allows us to evaluate the coupling parameters and the energies of diabatic states. The method shows that the energy order of the lowest four excited states are mostly determined by the excitation energy of the diabatic states and the exciton coupling parameter. For the torsion motion in small φ regions, the energetic order of the lowest two $^1B_1$ states differs if calculated at the CISD(4,4)/SV(P) or the SCS-CC2/TZV(P) level of theory. This is caused by the large V_{EC} value and the small excitation energy difference between the diabatic NE and CT states. The character analysis method is a very useful tool for the interpretation of the excited state calculations. We are going to apply this method to other CIS type methods such as TD-HF and TD-DFT. The MH method is proved to be a useful and cheap method for understanding the character of the excited states of aggregate systems. It can be easily applied to trimer or even higher oligomer systems.

Similar to the valence excited states investigations, we used several theoretical approaches, e. g. Frozen core approximation (FCA), ROHF and multi-configuration coupled electron pair approximation (MCCEPA), to predict the core excited state properties. Besides, the basis sets dependence is also studied. We have chosen a series of small organic molecules as examples. Their C atom K-shell excited states are calculated. These excited states are discussed separately for the different types of transitions: $1s \rightarrow \pi^*$, $1s \rightarrow$ *Rydberg state* and IP. For the $1s \rightarrow \pi^*$ type transition, the orbital relaxation is as important as correlation effects. An improved description of the core hole atom is more important than for the other atoms of the molecule. For the $1s \rightarrow$ *Rydberg state* type transition, the orbital relaxation is considerably less important than correlation effects. Appropriate descriptions of Rydberg orbitals are of crucial importance. Therefore, one should always include diffuse functions in the basis sets. For the IP calculations, all methods give better results than for the other types of transitions. The inclusion

of correlation effects further improves the results. The basis sets has only minor effect on those results.

The C atom K-shell excited states of the NTCDA monomer is calculated at the FCA/cc-pVTZ and FCA/cc-pVDZ levels of theories. The calculated NEXAFS spectra are obtained by Gaussian convolutions. They reproduce the main features of the experimental spectra correctly. In order to explain the 0.1 eV red shift which is found in the experiment for the NTCDA in the condensed phase in comparison to the gas phase, we investigated several possible explanations: geometry deformation, Davydov splitting and correlation effects. For the geometry deformations, we calculated the NEXAFS spectra for the distorted NTCDA monomer. The results show an energy splitting up to 30 meV which can only partially explain the 0.1 eV red shift. For the Davydov splitting, we proposed an algorithm for evaluating this effect when the non-orthogonal MOs are used for different excitations. However, the results show that this effect is too small (< 0.5 meV). Due to the size of the system, it is not easy to perform MCCEPA calculations for the NTCDA dimer systems.

Appendix A

Acronyms

B3LYP	Becke 3-Parameter (20% exact exchange), Lee, Yang and Parr (correlation)
BHLYP	Becke 3-Parameter (half exact exchange), Lee, Yang and Parr (correlation)
BLYP	Becke (exchange), Lee, Yang and Parr (correlation)
CAM-B3LYP	Coulomb-attenuating method based on the B3LYP functional
CASSCF	complete active space self consistent field
CC	coupled cluster
CC2	second-order approximate coupled-cluster
CI	configuration interaction
CT	charge transfer
DFT	density functional theory
EET	excitation energy transfer
FCA	frozen core approximation
FET	field-effect transistors
GGA	generalised gradient approximation
HF	Hatree-Fock
HOMO	highest occupied molecular orbital
IP	ionization potential
LC	long range corrected
LUMO	lowest unoccupied molecular orbital
MCCEPA	multi-configuration coupled election pair approximation
MH	model Hamiltonian

MO	molecular orbital
NE	neutral excited
NEXAFS	near edge X-ray absorption fine structure
NTCDA	naphthalene tetracarboxylic dianhydride
OLED	organic light-emitting diodes
PBE	Perdew-Burke-Ernzerhof functional
PBE0	Perdew-Burke-Ernzerhof (25% exact exchange) hybrid functional
PBI	perylene tetracarboxylic bisimide
PTCDA	perylene tetracarboxylic dianhydride
RET	resonance energy transfer
ROHF	restricted open-shell Hatree-Fock
SCF	self consistent field
SCS	spin component scaled
TD-DFT	time dependent density functional theory
TD-HF	time dependent Hatree-Fock

APPENDIX B

SIZE CONSISTENCY

As an obvious physical property, for any system, which is composed of many non-interacting monomers, its total energy is equal to the sum of all the monomer energies

$$E_{(\underbrace{A, B, C, \cdots}_{\substack{\text{no interaction} \\ \text{with each other}}})} = E_A + E_B + E_C + \cdots . \tag{B.0.1}$$

B.1. HATREE-FOCK METHOD

A "size consistent" method fulfills this property exactly. Take a simple dimer system as an example, where the two monomers A and B are separated by an infinite distance. In the HF approach, the ground state wavefunction of monomer A ($\Phi_{0(A)}$) given by a *Slater determinant*

$$\Phi_{0(A)} = \begin{vmatrix} \psi_1(\mathbf{x}_1) & \psi_2(\mathbf{x}_1) & \cdots & \psi_n(\mathbf{x}_1) \\ \psi_1(\mathbf{x}_2) & \psi_2(\mathbf{x}_2) & \cdots & \psi_n(\mathbf{x}_2) \\ \vdots & \vdots & \ddots & \vdots \\ \psi_1(\mathbf{x}_n) & \psi_2(\mathbf{x}_n) & \cdots & \psi_n(\mathbf{x}_n) \end{vmatrix}, \tag{B.1.1}$$

where we assume the monomer A to be a system with n elections and $\mathbf{x}_1$, $\mathbf{x}_2$, $\cdots$, $\mathbf{x}_n$ are their corresponding coordinates. $\{\psi_1, \psi_n, \cdots, \psi_m\}$ is a set of MOs describing the monomer A. Similarly, if the monomer B is a system of m elections,

its HF ground state wavefunction is given by

$$\Phi_{0(B)} = \begin{vmatrix} \psi'_1(\mathbf{x}_1) & \psi'_2(\mathbf{x}_1) & \cdots & \psi'_m(\mathbf{x}_1) \\ \psi'_1(\mathbf{x}_2) & \psi'_2(\mathbf{x}_2) & \cdots & \psi'_m(\mathbf{x}_2) \\ \vdots & \vdots & \ddots & \vdots \\ \psi'_1(\mathbf{x}_m) & \psi'_2(\mathbf{x}_m) & \cdots & \psi'_m(\mathbf{x}_m) \end{vmatrix}. \tag{B.1.2}$$

where $\mathbf{x}_1$, $\mathbf{x}_2$, $\cdots$, $\mathbf{x}_m$ are the election coordinates. $\{\psi'_1, \psi'_2, \cdots, \psi'_m\}$ are the MOs of the monomer B. If A is far away from B, the electrons on A do not occupy the orbitals of B and vice versa. Thus the HF ground state wavefunction of the AB dimer $\Phi_{0(AB)}$ is given by

$$\begin{aligned} \Phi_{0(AB)} &= \begin{vmatrix} \psi_1(\mathbf{x}_1) & \psi_2(\mathbf{x}_1) & \cdots & \psi_n(\mathbf{x}_1) & 0 & 0 & \cdots & 0 \\ \psi_1(\mathbf{x}_2) & \psi_2(\mathbf{x}_2) & \cdots & \psi_n(\mathbf{x}_2) & 0 & 0 & \cdots & 0 \\ \vdots & \vdots & \ddots & \vdots & \vdots & \vdots & \ddots & \vdots \\ \psi_1(\mathbf{x}_n) & \psi_2(\mathbf{x}_n) & \cdots & \psi_n(\mathbf{x}_n) & 0 & 0 & \cdots & 0 \\ 0 & 0 & \cdots & 0 & \psi'_1(\mathbf{x}_{n+1}) & \psi'_2(\mathbf{x}_{n+1}) & \cdots & \psi'_m(\mathbf{x}_{n+1}) \\ 0 & 0 & \cdots & 0 & \psi'_1(\mathbf{x}_{n+2}) & \psi'_2(\mathbf{x}_{n+2}) & \cdots & \psi'_m(\mathbf{x}_{n+2}) \\ \vdots & \vdots & \ddots & \vdots & \vdots & \vdots & \ddots & \vdots \\ 0 & 0 & \cdots & 0 & \psi'_1(\mathbf{x}_{n+m}) & \psi'_2(\mathbf{x}_{n+m}) & \cdots & \psi'_m(\mathbf{x}_{n+m}) \end{vmatrix} \\ &= \Phi_{0(A)} \cdot \Phi_{0(B)}. \end{aligned} \tag{B.1.3}$$

According to the *Schrödinger equation*, we assume that $\hat{\mathbf{H}}_A$ and $\hat{\mathbf{H}}_B$ are the monomer electronic Hamiltonians for evaluating the electronic energies of monomer A and B (E_A and E_B), respectively. Their HF energies are given by

$$\begin{aligned} E_A &= \frac{\langle \Phi_{0(A)} | \hat{\mathbf{H}}_A | \Phi_{0(A)} \rangle}{\langle \Phi_{0(A)} | \Phi_{0(A)} \rangle} \\ &= \sum_{a \text{ in A}} \langle a | \hat{h} | a \rangle + \frac{1}{2} \sum_{a,b \text{ in A}} \langle ab || ab \rangle, \end{aligned} \tag{B.1.4}$$

and

$$\begin{aligned} E_B &= \frac{\langle \Phi_{0(B)} | \hat{\mathbf{H}}_B | \Phi_{0(B)} \rangle}{\langle \Phi_{0(B)} | \Phi_{0(B)} \rangle} \\ &= \sum_{c \text{ in B}} \langle c | \hat{h} | c \rangle + \frac{1}{2} \sum_{c,d \text{ in B}} \langle cd || cd \rangle, \end{aligned} \tag{B.1.5}$$

Since there is no interaction between the two monomers, the total electronic Hamiltonian $\hat{\mathbf{H}}_{AB}$ is given as the sum of the two monomer Hamiltonians

$$\hat{\mathbf{H}}_{AB} = \hat{\mathbf{H}}_A + \hat{\mathbf{H}}_B. \tag{B.1.6}$$

Thus the *Schrödinger equation* for the dimer system gives

$$\begin{aligned} E_{AB} &= \frac{\langle \Phi_{0(AB)} | \hat{\mathbf{H}}_{AB} | \Phi_{0(AB)} \rangle}{\langle \Phi_{0(AB)} | \Phi_{0(AB)} \rangle} \\ &= \sum_{e \text{ in AB}} \langle e|\hat{h}|e\rangle + \frac{1}{2} \sum_{e,f \text{ in AB}} \langle ef||ef\rangle \\ &= \sum_{a \text{ in A}} \langle a|\hat{h}|a\rangle + \sum_{c \text{ in B}} \langle c|\hat{h}|c\rangle \\ &\quad + \frac{1}{2} \sum_{a,b \text{ in A}} \langle ab||ab\rangle + \frac{1}{2} \sum_{c,d \text{ in B}} \langle cd||cd\rangle \\ &= E_A + E_B \end{aligned} \tag{B.1.7}$$

This shows that the HF is a "size consistent" method. It can be shown that, for any "size consisten" method, its wavefunction Ψ_0 of non-interacting systems is equal to the product of the ground state wavefunctions of all the subsystems $(\Phi_{0(A)}, \Phi_{0(B)}, \Phi_{0(C)}, \cdots)$

$$\Psi_0 = \prod_{i=A,B,C\cdots} \Phi_{0(i)}. \tag{B.1.8}$$

B.2. Configuration Interaction Doubles method

An intermediate normalized ground state wavefunction of Configuration Interaction Doubles (CID) method for the same dimer system AB ($\Psi_{0(AB)}$) is given by a linear combination of the HF ground state $\Phi_{0(AB)}$ and doubly excited configurations $\Phi^{mn}_{ef(AB)}$

$$\Psi_{0(AB)} = \Phi_{0(AB)} + \sum_{\substack{e<f,\\ m<n}} c^{mn}_{ef(AB)} \Phi^{mn}_{ef(AB)}. \tag{B.2.1}$$

Since the monomers A and B have no interaction with each other, only two parts of the doubly excited configurations in equation (B.2.1) can survive

$$\sum_{\substack{e<f,\\ m<n}} c^{mn}_{ef(AB)} \Phi^{mn}_{ef(AB)} = \sum_{\substack{a<b,\\ i<j}} c^{ij}_{ab(A)} \Phi^{ij}_{ab(A)} \cdot \Phi_{0(B)} + \sum_{\substack{c<d,\\ k<l}} c^{kl}_{cd(B)} \Phi^{kl}_{cd(B)} \cdot \Phi_{0(A)}, \tag{B.2.2}$$

where the $\Phi^{ij}_{ab(A)}$ and $\Phi^{kl}_{cd(B)}$ are the doubly excited configurations restricted to monomer A and B respectively. Other terms such as the neutral separately single excited configurations on A and B ($\Phi^{i}_{a(A)} \cdot \Phi^{j}_{b(B)}$) and charge transfer configurations ($\Phi^{ij(-)}_{a(A)} \cdot \Phi^{+}_{b(B)}$ and $\Phi^{ij(2-)}_{(A)} \cdot \Phi^{(2+)}_{ab(B)}$ etc.) disappear due to the infinite distance between the two monomers that cause that these configurations have no coupling with the HF ground state.
Similarly, we get the CID ground state wavefunctions for monomers A and B

$$\Psi_{0(A)} = \Phi_{0(A)} + \sum_{\substack{a<b,\\ i<j}} c^{ij}_{ab(A)} \Phi^{ij}_{ab(A)}, \qquad \Psi_{0(B)} = \Phi_{0(B)} + \sum_{\substack{c<d,\\ k<l}} c^{kl}_{cd(B)} \Phi^{kl}_{cd(B)}. \tag{B.2.3}$$

By inserting equations (B.2.1 and B.2.2), the product of monomer's CID ground state wavefunctions gives

$$\begin{aligned}
\Psi_{0(A)} \cdot \Psi_{0(B)} =& \Phi_{0(A)} \cdot \Phi_{0(B)} + \sum_{\substack{a<b,\\ i<j}} c^{ij}_{ab(A)} \Phi^{ij}_{ab(A)} \cdot \Phi_{0(B)} + \sum_{\substack{c<d,\\ k<l}} c^{kl}_{cd(B)} \Phi^{kl}_{cd(B)} \cdot \Phi_{0(A)} \\
&+ \sum_{\substack{a<b,\\ i<j}} \sum_{\substack{c<d,\\ k<l}} c^{ij}_{ab(A)} c^{kl}_{cd(B)} \Phi^{ij}_{ab(A)} \Phi^{kl}_{cd(B)} \\
=& \Psi_{0(AB)} + \sum_{\substack{a<b,\\ i<j}} \sum_{\substack{c<d,\\ k<l}} c^{ij}_{ab(A)} c^{kl}_{cd(B)} \Phi^{ij}_{ab(A)} \Phi^{kl}_{cd(B)}.
\end{aligned} \tag{B.2.4}$$

This shows immediately that the CID method is not "size consisten".

B.3. Coupled Cluster Singles and Doubles method

Considering the same dimer system composed of two non-interacting monomers A and B, its *Coupled Cluster Singles and Doubles* (CCSD) ground state function $\Psi_0(AB)$ is given as an excitation operator $e^{\mathbf{T}_{AB}}$ acting on the HF ground state of the system $\Phi_0(AB)$

$$\Psi_0(AB) = e^{\mathbf{T}_{AB}} \Phi_0(AB). \tag{B.3.1}$$

For monomers A and B, their ground state wavefunctions are given in a similar way

$$\Psi_0(A) = e^{\mathbf{T}_A} \Phi_0(A), \qquad \Psi_0(B) = e^{\mathbf{T}_B} \Phi_0(B). \tag{B.3.2}$$

As discussed in section 3.1.2, $\mathbf{T}_A$, $\mathbf{T}_B$ and $\mathbf{T}_{AB}$ are the singly and doubly excitation operators for the systems A, B and AB, respectively. For this non-interacting case,

$\mathbf{T}_{AB}$ is equal to the sum of $\mathbf{T}_A$ and $\mathbf{T}_B$

$$\mathbf{T}_{AB} = \mathbf{T}_A + \mathbf{T}_B. \tag{B.3.3}$$

By inserting equations (B.1.3, B.3.3 and B.3.2) into equation (B.3.1), we get

$$\begin{aligned} \Psi_0(AB) &= e^{(\mathbf{T}_A+\mathbf{T}_B)}\Phi_0(AB) \\ &= e^{\mathbf{T}_A}e^{\mathbf{T}_B}\Phi_0(AB) \\ &= e^{\mathbf{T}_A}e^{\mathbf{T}_B}\Phi_{0(A)}\cdot\Phi_{0(B)} \\ &= \Psi_0(A)\cdot\Psi_0(B). \end{aligned} \tag{B.3.4}$$

This shows that the CCSD ground state wavefunction satisfies equation (B.1.8). Therefore, the CCSD method is “size consistent”.

APPENDIX C

EXPLICIT FORMULATIONS

In this section, the explicit derivations for equations (3.2.7, 3.2.8 and 3.2.9) are given.

V_{EC}:

We start with the definition for V_{EC} of equation (2.2.3). By inserting the equations (3.2.2 and 3.2.3), we get

$$\begin{aligned} V_{\mathrm{EC}} &= \frac{1}{2}\big[\langle h_A\bar{l}_A h_B\bar{h}_B|\hat{\mathbf{H}}|h_A\bar{h}_A h_B\bar{l}_B\rangle + \langle h_A\bar{l}_A h_B\bar{h}_B|\hat{\mathbf{H}}|h_A\bar{h}_A l_B\bar{h}_B\rangle \\ &\quad + \langle l_A\bar{h}_A h_B\bar{h}_B|\hat{\mathbf{H}}|h_A\bar{h}_A h_B\bar{l}_B\rangle + \langle l_A\bar{h}_A h_B\bar{h}_B|\hat{\mathbf{H}}|h_A\bar{h}_A l_B\bar{h}_B\rangle\big]. \end{aligned} \tag{C.0.1}$$

In order to simplify the above equation, we interchange several orbitals based on the *Pauli Principle*. By using the *Slater-Condon rules*, we get

$$\begin{aligned} V_{\mathrm{EC}} &= \frac{1}{2}\big[\langle h_A h_B\bar{l}_A\bar{h}_B|\hat{\mathbf{H}}|h_A h_B\bar{h}_A\bar{l}_B\rangle + \langle h_A\bar{h}_B\bar{l}_A h_B|\hat{\mathbf{H}}|h_A\bar{h}_B\bar{h}_A l_B\rangle \\ &\quad + \langle\bar{h}_A h_B l_A\bar{h}_B|\hat{\mathbf{H}}|\bar{h}_A h_B h_A\bar{l}_B\rangle + \langle\bar{h}_A\bar{h}_B l_A h_B|\hat{\mathbf{H}}|\bar{h}_A\bar{h}_B h_A l_B\rangle\big] \\ &= \frac{1}{2}\big[\langle\bar{l}_A\bar{h}_B||\bar{h}_A\bar{l}_B\rangle + \langle\bar{l}_A h_B||\bar{h}_A l_B\rangle \\ &\quad + \langle l_A\bar{h}_B||h_A\bar{l}_B\rangle + \langle l_A h_B||h_A l_B\rangle \\ &= \frac{1}{2}\big[(l_A h_A|h_B l_B) - (l_A l_B|h_B h_A) + (l_A h_A|h_B l_B) \\ &\quad + (l_A h_A|h_B l_B) + (l_A h_A|h_B l_B) - (l_A l_B|h_B h_A)\big] \\ &= 2(l_A h_A|h_B l_B) - (l_A l_B|h_B h_A). \end{aligned} \tag{C.0.2}$$

W:

By inserting the equations (3.2.4 and 3.2.5) into equation (2.2.5), we get

$$\begin{aligned} W &= \frac{1}{2}\big[\langle h_A\bar{l}_B h_B\bar{h}_B|\hat{\mathbf{H}}|h_A\bar{h}_A h_B\bar{l}_A\rangle + \langle h_A\bar{l}_B h_B\bar{h}_B|\hat{\mathbf{H}}|h_A\bar{h}_A l_A\bar{h}_B\rangle \\ &\quad + \langle l_B\bar{h}_A h_B\bar{h}_B|\hat{\mathbf{H}}|h_A\bar{h}_A h_B\bar{l}_A\rangle + \langle l_B\bar{h}_A h_B\bar{h}_B|\hat{\mathbf{H}}|h_A\bar{h}_A l_A\bar{h}_B\rangle\big]. \end{aligned} \tag{C.0.3}$$

Similarly, we interchange several orbitals and get

$$\begin{aligned} W &= \frac{1}{2}\big[\langle h_A h_B\bar{l}_B\bar{h}_B|\hat{\mathbf{H}}|h_A h_B\bar{h}_A\bar{l}_A\rangle + \langle h_A\bar{h}_B\bar{l}_B h_B|\hat{\mathbf{H}}|h_A\bar{h}_B\bar{h}_A l_A\rangle \\ &\quad + \langle\bar{h}_A h_B l_B\bar{h}_B|\hat{\mathbf{H}}|\bar{h}_A h_B h_A\bar{l}_A\rangle + \langle\bar{h}_A\bar{h}_B l_B h_B|\hat{\mathbf{H}}|\bar{h}_A\bar{h}_B h_A l_A\rangle\big] \\ &= \frac{1}{2}\big[\langle\bar{l}_B\bar{h}_B||\bar{h}_A\bar{l}_A\rangle + \langle\bar{l}_B h_B||\bar{h}_A l_A\rangle \\ &\quad + \langle l_B\bar{h}_B||h_A\bar{l}_A\rangle + \langle l_B h_B||h_A l_A\rangle \\ &= \frac{1}{2}\big[(l_B h_A|h_B l_A) - (l_B l_A|h_B h_A) + (l_B h_A|h_B l_A) \\ &\quad + (l_B h_A|h_B l_A) + (l_B h_A|h_B l_A) - (l_B l_A|h_B h_A)\big] \\ &= 2(l_B h_A|h_B l_A) - (l_B l_A|h_B h_A). \end{aligned} \tag{C.0.4}$$

It is worth to mention that in the *chemists notation* the two election integrals are written as electron density interactions. Such that the integrals do not change the value if the orbitals interchange in the following way

$$\begin{aligned} (l_B h_A|h_B l_A) &= (h_A l_B|h_B l_A) = (l_B h_A|l_A h_B) = (h_A l_B|l_A h_B) \\ (h_B l_A|l_B h_A) &= (l_A h_B|l_B h_A) = (h_B l_A|h_A l_B) = (l_A h_B|h_A l_B) \end{aligned} \tag{C.0.5}$$

D_e:

By inserting the equations (3.2.2 and 3.2.4) into equation (2.2.6), we get

$$\begin{aligned} D_e &= \langle\Psi_{A^+B^-}|\hat{\mathbf{H}}|\Psi_{A^*B}\rangle \\ &= \frac{1}{2}\big[\langle h_A\bar{l}_B h_B\bar{h}_B|\hat{\mathbf{H}}|h_A\bar{l}_A h_B\bar{h}_B\rangle + \langle h_A\bar{l}_B h_B\bar{h}_B|\hat{\mathbf{H}}|l_A\bar{h}_A h_B\bar{h}_B\rangle \\ &\quad + \langle l_B\bar{h}_A h_B\bar{h}_B|\hat{\mathbf{H}}|h_A\bar{l}_A h_B\bar{h}_B\rangle + \langle l_B\bar{h}_A h_B\bar{h}_B|\hat{\mathbf{H}}|l_A\bar{h}_A h_B\bar{h}_B\rangle\big]. \end{aligned} \tag{C.0.6}$$

Again, we interchange several orbitals and get

$$\begin{aligned}
D_e &= \frac{1}{2}\big[\langle h_A h_B \bar{h}_B \bar{l}_B|\hat{\mathbf{H}}|h_A h_B \bar{h}_B \bar{l}_A\rangle + \langle h_B \bar{h}_B h_A \bar{l}_B|\hat{\mathbf{H}}|h_B \bar{h}_B l_A \bar{h}_A\rangle \\
&\quad + \langle h_B \bar{h}_B l_B \bar{h}_A|\hat{\mathbf{H}}|h_B \bar{h}_B h_A \bar{l}_A\rangle + \langle \bar{h}_A h_B \bar{h}_B l_B|\hat{\mathbf{H}}|\bar{h}_A h_B \bar{h}_B l_A\rangle\big] \\
&= \frac{1}{2}\big[\langle \bar{l}_B|\hat{h}|\bar{l}_A\rangle + \langle h_A \bar{l}_B||h_A \bar{l}_A\rangle + \langle h_B \bar{l}_B||h_B \bar{l}_A\rangle + \langle \bar{h}_B \bar{l}_B||\bar{h}_B \bar{l}_A\rangle \\
&\quad + \langle h_A \bar{l}_B||l_A \bar{h}_A\rangle \\
&\quad + \langle l_B \bar{h}_A||h_A \bar{l}_A\rangle \\
&\quad + \langle l_B|\hat{h}|l_A\rangle + \langle \bar{h}_A l_B||\bar{h}_A l_A\rangle + \langle h_B l_B||h_B l_A\rangle + \langle \bar{h}_B l_B||\bar{h}_B l_A\rangle\big] \\
&= \frac{1}{2}\big[(l_B|\hat{h}|l_A) + (h_A h_A|l_B l_A) + (h_B h_B|l_B l_A) \\
&\quad + (h_B h_B|l_B l_A) - (h_B l_A|l_B h_B) + (h_A l_B|l_A h_A) \\
&\quad + (l_B h_A|h_A l_A) + (l_B|\hat{h}|l_A) + (h_A h_A|l_B l_A) \\
&\quad + (h_B h_B|l_B l_A) - (h_B l_A|l_B h_B) + (h_B h_B|l_B l_A)\big]. \qquad \text{(C.0.7)}
\end{aligned}$$

Let us introduce the *Fock operator* $\hat{\mathbf{F}}$, that it satisfy

$$(a|\hat{\mathbf{F}}|b) = (a|\hat{h}|b) + \sum_{i}^{nocc}\big[2(ii|ab) - (ib|ai)\big]. \qquad \text{(C.0.8)}$$

For our system, we have

$$\begin{aligned}
(l_B|\hat{\mathbf{F}}|l_A) =& (l_B|\hat{h}|l_A) + 2(h_A h_A|l_B l_A) - (h_A l_A|l_B h_A) \\
&+ 2(h_B h_B|l_B l_A) - (h_B l_A|l_B h_B). \qquad \text{(C.0.9)}
\end{aligned}$$

By inserting equation (C.0.9) into equation (C.0.7), we get

$$D_e = (l_B|\hat{\mathbf{F}}|l_A) + 2(h_A l_B|l_A h_A) - (h_A h_A|l_B l_A). \qquad \text{(C.0.10)}$$

APPENDIX D

ADDITIONAL RESULTS

Table D.1.: Excitation energy differences between TD-DFT and SCS-CC2.

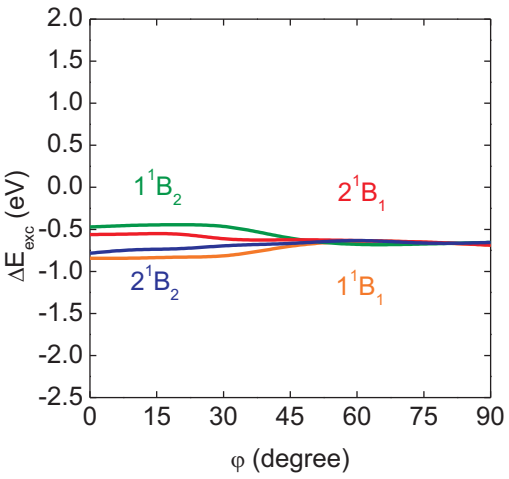

Excitation energy difference of TD-PBE0-D and SCS-CC2 ($\Delta E_{exc} = E_{\text{PBE0-D}} - E_{\text{SCS-CC2}}$) only considering the energy sequence of the states.

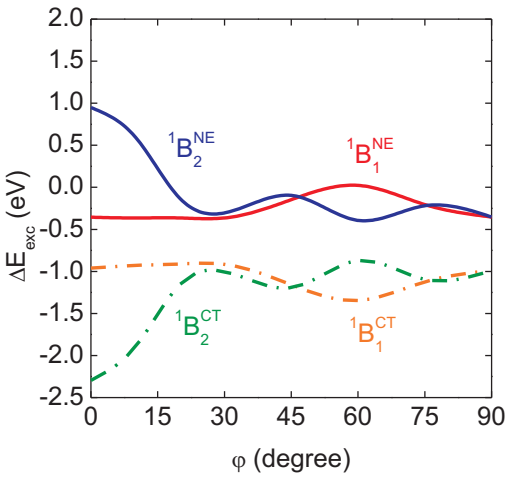

Excitation energy difference of TD-PBE0-D and SCS-CC2 ($\Delta E_{exc} = E_{\text{PBE0-D}} - E_{\text{SCS-CC2}}$) for the states of corresponding characters.

Table D.1.: continued

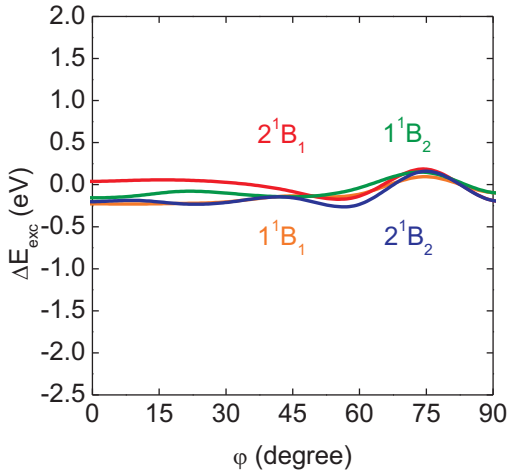

Excitation energy difference of TD-BHLYP-D and SCS-CC2 ($\Delta E_{exc} = E_{\text{BHLYP-D}} - E_{\text{SCS-CC2}}$) only considering the energy sequence of the states.

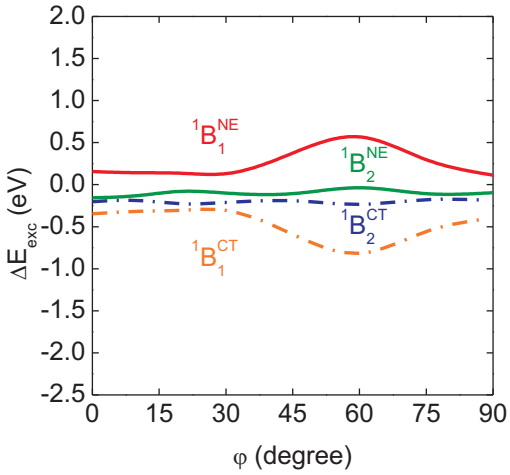

Excitation energy difference of TD-BHLYP-D and SCS-CC2 ($\Delta E_{exc} = E_{\text{BHLYP-D}} - E_{\text{SCS-CC2}}$) for the states of corresponding characters.

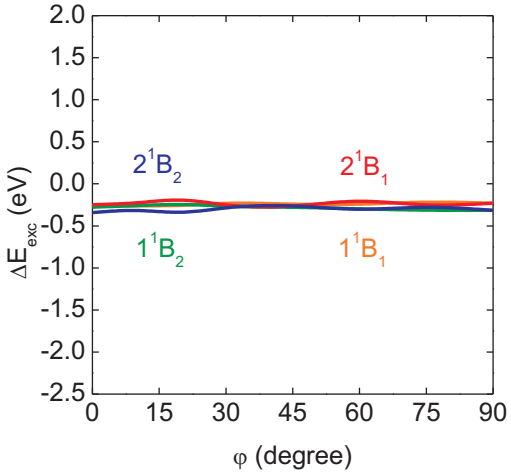

Excitation energy difference of TD-CAM-B3LYP-D and SCS-CC2 ($\Delta E_{exc} = E_{\text{CAM-B3LYP-D}} - E_{\text{SCS-CC2}}$) only considering the energy sequence of the states.

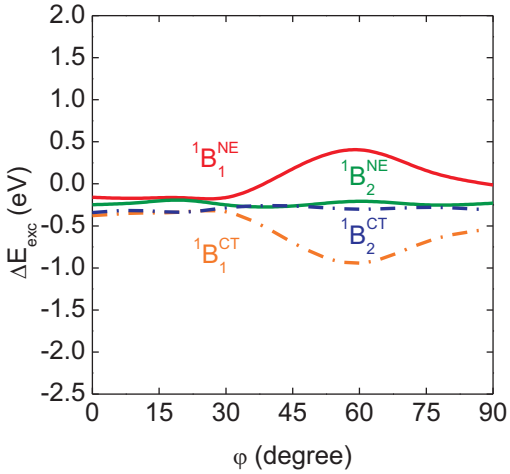

Excitation energy difference of TD-CAM-B3LYP-D and SCS-CC2 ($\Delta E_{exc} = E_{\text{CAM-B3LYP-D}} - E_{\text{SCS-CC2}}$) for the states of corresponding characters.

Table D.2.: Excited state properties of TD-PBE-D and TD-PBE0-D.

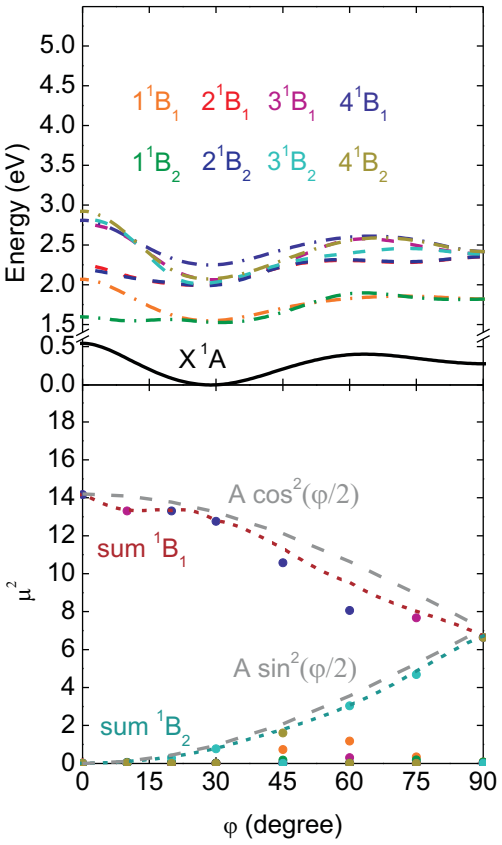

TD-PBE-D results: (Upper part) Potential energy curves of the ground state (black), the charge transfer states (colour, dot-dashed) and excited states with undefined character (colour, dashed) as a function of the torsional angle φ. (Lower part) Squared transition dipole moments of the excited states (ponits). The dashed lines are the sums of the squared transition dipole moments of the $^1B_1$ (brown) and $^1B_2$ (blue) excited states.

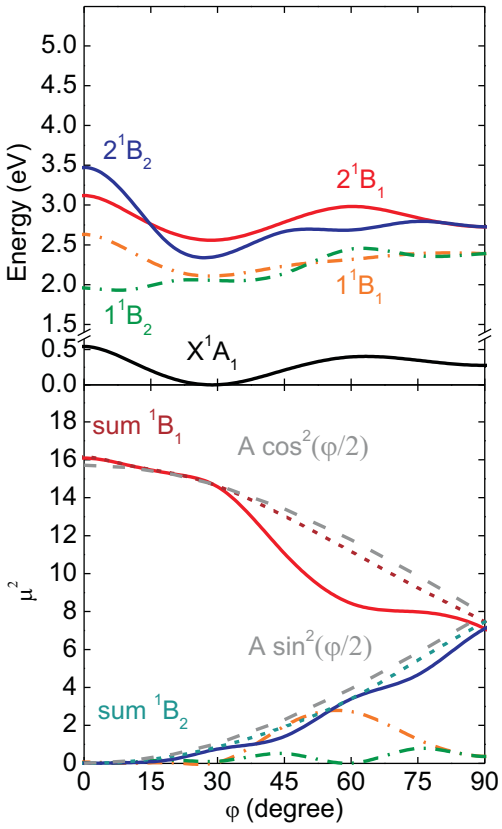

TD-PBE0-D results: (Upper part) Potential energy curves of the ground state (black), the charge transfer states (colour, dot-dashed) and neutral states (colour, solid) as a function of the torsional angle φ. (Lower part) Squared transition dipole moments of the excited states (ponits). The dashed lines are the sums of the squared transition dipole moments of the $^1B_1$ (brown) and $^1B_2$ (blue) excited states.

Table D.3.: CT characters of TD-PBE0-D, TD-BHLYP-D and TD-CAM-B3LYP-D.

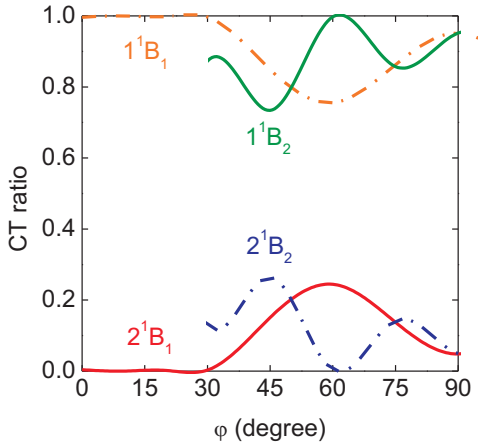

Calculated ratio of CT character for the four lowest excited states as obtained by TD-PBE0-D.

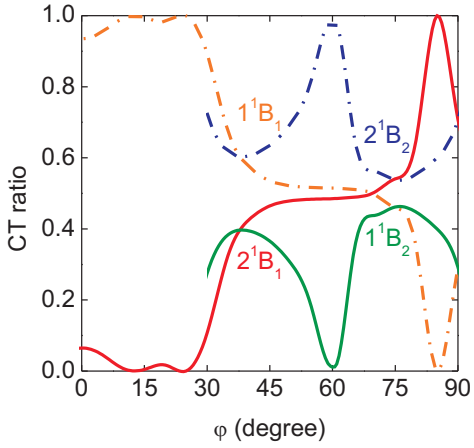

Calculated ratio of CT character for the four lowest excited states as obtained by TD-BHLYP-D.

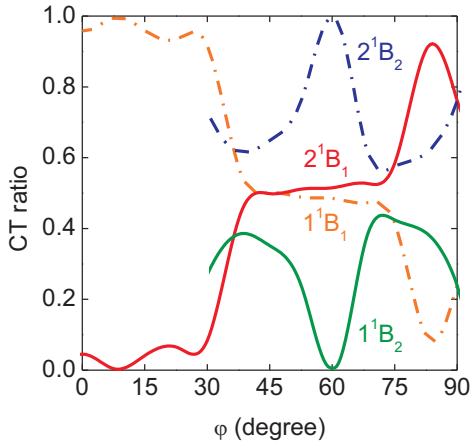

Calculated ratio of CT character for the four lowest excited states as obtained by TD-CAM-B3LYP-D.

Table D.4.: Contributions of the leading configurations in excited states.

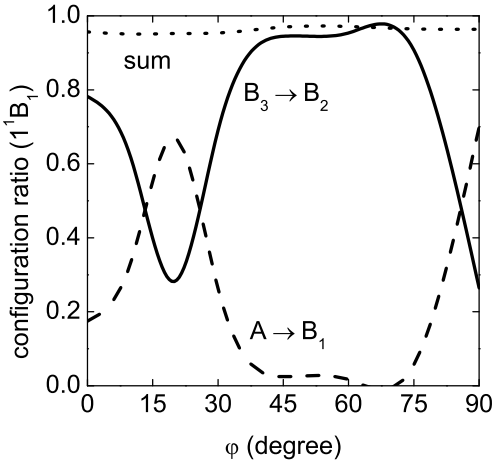

Contributions of the two leading configurations to the total wavefunction and their sum for the 1^1B_1 state.

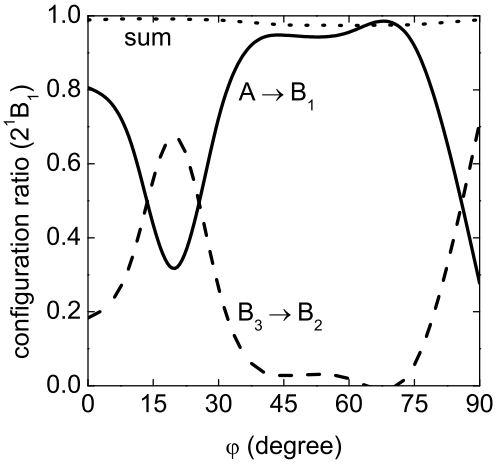

Contributions of the two leading configurations to the total wavefunction and their sum for the 2^1B_1 state.

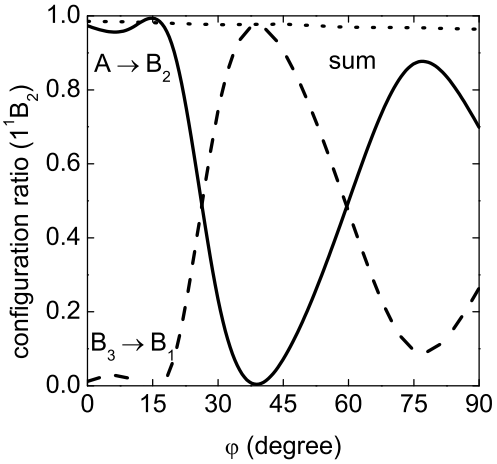

Contributions of the two leading configurations to the total wavefunction and their sum for the 1^1B_2 state.

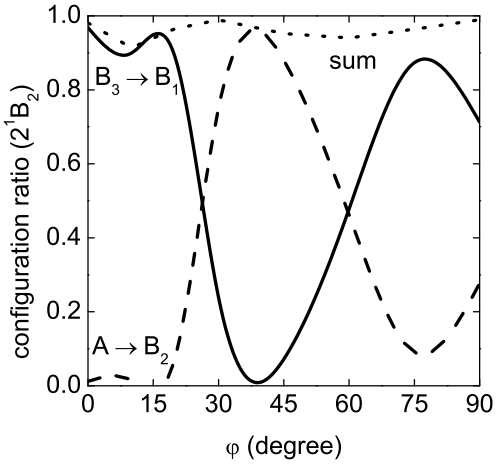

Contributions of the two leading configurations to the total wavefunction and their sum for the 2^1B_2 state.

BIBLIOGRAPHY

[1] Brédas, J.-L.; Beljonne, D.; Coropceanu, V.; Cornil, J. *Chemical Reviews* **2004**, *104*, 4971–5004.

[2] Cornil, J.; Beljonne, D.; Calbert, J.-P.; Brédas, J.-L. *Advanced Materials* **2001**, *13*, 1053–1067.

[3] Brédas, J.-L.; Cornil, J.; Heeger, A. J. *Advanced Materials* **1996**, *8*, 447–452.

[4] Pullerits, T. o.; Sundström, V. *Accounts of Chemical Research* **1996**, *29*, 381–389.

[5] Grimsdale, A. C.; Müllen, K. *Angewandte Chemie International Edition* **2005**, *44*, 5592–5629.

[6] Sancho-García, J. C.; Pérez-Jiménez, A. J. *The Journal of Chemical Physics* **2008**, *129*, 024103.

[7] Damjanović, A.; Kosztin, I.; Kleinekathöfer, U.; Schulten, K. *Phys. Rev. E* **2002**, *65*, 031919.

[8] Hadipour, A.; de Boer, B.; Wildeman, J.; Kooistra, F.; Hummelen, J.; Turbiez, M.; Wienk, M.; Janssen, R.; Blom, P. *Advanced Functional Materials* **2006**, *16*, 1897–1903.

[9] Gustafsson, G.; Cao, Y.; Treacy, G. M.; Klavetter, F.; Colaneri, N.; Heeger, A. J. *Nature* **1992**, *357*, 477–479.

[10] Brabec, C. J.; Cravino, A.; Meissner, D.; Sariciftci, N. S.; Fromherz, T.; Rispens, M. T.; Sanchez, L.; Hummelen, J. C. *Advanced Functional Materials* **2001**, *11*, 374–380.

[11] Coakley, K. M.; McGehee, M. D. *Chemistry of Materials* **2004**, *16*, 4533–4542.

[12] Forrest, S. R. *Chemical Reviews* **1997**, *97*, 1793–1896.

[13] Peumans, P.; Yakimov, A.; Forrest, S. R. *Journal of Applied Physics* **2003**, *93*, 3693–3723.

[14] Shaheen, S. E.; Jabbour, G. E.; Kippelen, B.; Peyghambarian, N.; Anderson, J. D.; Marder, S. R.; Armstrong, N. R.; Bellmann, E.; Grubbs, R. H. *Applied Physics Letters* **1999**, *74*, 3212–3214.

[15] Katz, H. E.; Lovinger, A. J.; Johnson, J.; Kloc, C.; Siegrist, T.; Li, W.; Lin, Y. Y.; Dodabalapur, A. *nature* **2000**, *404*, 478–481.

[16] Bao, Z. *Advanced Materials* **2000**, *12*, 227–230.

[17] Campbell, I. H.; Crone, B. K. *Journal of Applied Physics* **2009**, *106*, 113704.

[18] Sugawara, Y.; Kaji, Y.; Ogawa, K.; Eguchi, R.; Oikawa, S.; Gohda, H.; Fujiwara, A.; Kubozono, Y. *Applied Physics Letters* **2011**, *98*, 013303.

[19] Yang, G.; Si, Y.; Geng, Y.; Yu, F.; Wu, Q.; Su, Z. *Theoretical Chemistry Accounts: Theory, Computation, and Modeling (Theoretica Chimica Acta)* **2011**, *128*, 257–264.

[20] Rim, S.-B.; Fink, R. F.; Schöneboom, J. C.; Erk, P.; Peumans, P. *Applied Physics Letters* **2007**, *91*, 173504.

[21] Hippius, C.; van Stokkum, I. H. M.; Zangrando, E.; Williams, R. M.; Wykes, M.; Beljonne, D.; Würthner, F. *The Journal of Physical Chemistry C* **2008**, *112*, 14626–14638.

[22] Burquel, A.; Lemaur, V.; Beljonne, D.; Lazzaroni, R.; Cornil, J. *J. Phys. Chem. A* **2006**, *110*, 3447–3453.

[23] Petelenz, P. *Chem. Phys. Lett.* **1977**, *47*, 603–605.

[24] Reineker, P.; Schmid, B. J.; Petelenz, P. *Chem. Phys.* **1984**, *91*, 59–67.

[25] Petelenz, P.; Brovchenko, I.; Mucha, D.; Slawik, M. *Chem. Phys.* **1990**, *143*, 415–421.

[26] Nowakowska, M.; Smoluch, M.; Petelenz, P. *Chem. Phys. Lett.* **1997**, *270*, 234–240.

[27] Cheng, Y. C.; Silbey, R. J.; da Silva Filho, D. A.; Calbert, J. P.; Cornil, J.; Brédas, J. L. *The Journal of Chemical Physics* **2003**, *118*, 3764–3774.

[28] Valeev, E. F.; Coropceanu, V.; da Silva Filho, D. A.; Salman, S.; Brédas, J.-L. *Journal of the American Chemical Society* **2006**, *128*, 9882–9886.

[29] Coropceanu, V.; Cornil, J.; da Silva Filho, D. A.; Olivier, Y.; Silbey, R.; Brédas, J.-L. *Chemical Reviews* **2007**, *107*, 926–952.

[30] Scholz, R.; Kobitski, A. Y.; Zahn, D. R. T.; Schreiber, M. *Phys. Rev. B* **2005**, *72*, 245208.

[31] Gisslén, L.; Scholz, R. *Phys. Rev. B* **2009**, *80*, 115309.

[32] Förster, T. *Modern quantum chemistry, istanbul lectures, Part III: Action of light and organic crystals (ed.)*;
Academic Press, Inc.: New York, 1965;
pp 97–137.

[33] Agranovich, V. M.; Galanin, M. D. *Electronic Excitation Transfer in Condensed Matter*;
North Holland: Amsterdam, 1982.

[34] Van Der Meer, B. W.; Coker, G.; Chen, S. Y. S. *Resonance Energy Transfer: Theory and Data*;
VCH: New York, 1994.

[35] Kilså, K.; Kajanus, J.; Mårtensson, J.; Albinsson, B. *The Journal of Physical Chemistry B* **1999**, *103*, 7329–7339.

[36] Van Amerongen, H.; Valkunas, L.; Van Grondelle, R. *Photosynthetic Excitons*;
World Sci.: Singapore, 2000.

[37] Beljonne, D.; Cornil, J.; Silbey, R.; Millié, P.; Brédas, J. L. *The Journal of Chemical Physics* **2000**, *112*, 4749–4758.

[38] Smith, T. A.; Lokan, N.; Cabral, N.; Davies, S. R.; Paddon-Row, M. N.; Ghiggino, K. P. *Journal of Photochemistry and Photobiology A: Chemistry* **2002**, *149*, 55 – 69.

[39] Pettersson, K.; Kyrychenko, A.; Rönnow, E.; Ljungdahl, T.; Mårtensson, J.; Albinsson, B. *The Journal of Physical Chemistry A* **2006**, *110*, 310–318.

[40] Wasielewski, M. R. *Accounts of Chemical Research* **2009**, *42*, 1910–1921.

[41] Benk, H.; Haken, H.; Sixl, H. *J. Chem. Phys.* **1982**, *77*, 5730–5747.

[42] Hsu, C.-P.; Fleming, G. R.; Head-Gordon, M.; Head-Gordon, T. *The Journal of Chemical Physics* **2001**, *114*, 3065–3072.

[43] Scholes, G. D. *Annual Review of Physical Chemistry* **2003**, *54*, 57–87.

[44] Iozzi, M. F.; Mennucci, B.; Tomasi, J.; Cammi, R. *The Journal of Chemical Physics* **2004**, *120*, 7029–7040.

[45] Poulsen, L.; Jazdzyk, M.; Communal, J.-E.; Sancho-GarcÃa, J. C.; Mura, A.; Bongiovanni, G.; Beljonne, D.; Cornil, J.; Hanack, M.; Egelhaaf, H.-J.; Gierschner, J. *Journal of the American Chemical Society* **2007**, *129*, 8585–8593.

[46] Fückel, B.; Köhn, A.; Harding, M. E.; Diezemann, G.; Hinze, G.; Basché, T.; Gauss, J. *The Journal of Chemical Physics* **2008**, *128*, 074505.

[47] Kimura, A. *The Journal of Chemical Physics* **2009**, *130*, 154103.

[48] Sancho-García, J. *Chemical Physics* **2007**, *331*, 321–331.

[49] Dirac, P. A. M. *Proc. Royal Soc. A* **1929**, *123*, 714–733.

[50] Slater, J. C. *Phys. Rev.* **1951**, *81*, 385–390.

[51] Lee, C.; Yang, W.; Parr, R. G. *Phys. Rev. B* **1988**, *37*, 785–789.

[52] Becke, A. D. *The Journal of Chemical Physics* **1993**, *98*, 5648–5652.

[53] Becke, A. D. *Phys. Rev. A* **1988**, *38*, 3098–3100.

[54] Perdew, J. P.; Wang, Y. *Phys. Rev. B* **1992**, *45*, 13244–13249.

[55] Perdew, J. P.; Burke, K.; Ernzerhof, M. *Phys. Rev. Lett.* **1996**, *77*, 3865–3868.

[56] Vosko, S. H.; Wilk, L.; Nusair, M. *Can. J. Phys* **1980**, *58*, 1200–1211.

[57] Becke, A. D. *The Journal of Chemical Physics* **1993**, *98*, 1372–1377.

[58] Perdew, J. P.; Ernzerhof, M.; Burke, K. *The Journal of Chemical Physics* **1996**, *105*, 9982–9985.

[59] Yanai, T.; Tew, D. P.; Handy, N. C. *Chemical Physics Letters* **2004**, *393*, 51 – 57.

[60] Szabo, A.; Ostlund, N. S. *Modern quantum chemistry introduction to advanced electronic structure theory*, 1st ed.;
Dover Publications, Inc.: New York, 1996.

[61] Jensen, F. *Introduction to computational chemistry*, 1st ed.;
John Wiley & Sons Ltd.: Chichester, 1999.

[62] Schäfer, A.; Huber, C.; Ahlrichs, R. *J. Chem. Phys.* **1994**, *100*, 5829–5835.

[63] Christiansen, O.; Koch, H.; Jørgensen, P. *Chemical Physics Letters* **1995**, *243*, 409 – 418.

[64] Hoffmann, M.; Schmidt, K.; Fritz, T.; Hasche, T.; Agranovich, V. M.; Leo, K. *Chem. Phys.* **2000**, *258*, 73 – 96.

[65] Vragović, I.; Scholz, R. *Phys. Rev. B* **2003**, *68*, 155202.

[66] Förster, T. *Annalen der Physik* **1948**, *437*, 55–75.

[67] Dexter, D. L. *The Journal of Chemical Physics* **1953**, *21*, 836–850.

[68] Press, W. H.; Teukolsky, S. A.; Vetterling, W. T.; Flannery, B. P. *Numerical recipes in FORTRAN the art of scientific computing*, 2nd ed.;
Cambridge University Press: Cambridge, 1992.

[69] Löwdin, P.-O. *Phys. Rev.* **1955**, *97*, 1474–1489.

[70] Löwdin, P.-O. *The Journal of Chemical Physics* **1950**, *18*, 365–375.

[71] Mayer, I. *International Journal of Quantum Chemistry* **2002**, *90*, 63–65.

[72] Dreuw, A.; Head-Gordon, M. *J. Am. Chem. Soc.* **2004**, *126*, 4007–4016.

[73] Hieringer, W.; Görling, A. *Chem. Phys. Lett.* **2006**, *419*, 557–562.

[74] Dreuw, A.; Head-Gordon, M. *Chem. Phys. Lett.* **2006**, *426*, 231–233.

[75] Hieringer, W.; Görling, A. *Chem. Phys. Lett.* **2006**, *426*, 234–236.

[76] Peach, M. J. G.; Benfield, P.; Helgaker, T.; Tozer, D. J. *J. Chem. Phys.* **2008**, *128*, 044118.

[77] Teale, A. M.; Proft, F. D.; Tozer, D. J. *J. Chem. Phys.* **2008**, *129*, 044110.

[78] Kasha, M.; Rawls, H. R.; Asharf el-Bayoumi, M. *Pure Appl. Chem.* **1965**, *11*, 371–391.

[79] Mukamel, S.; Franchi, D. S.; Loring, R. F. *Chemical Physics* **1988**, *128*, 99–123.

[80] Hennebicq, E.; Pourtois, G.; Scholes, G. D.; Herz, L. M.; Russell, D. M.; Silva, C.; Setayesh, S.; Grimsdale, A. C.; MÃ$\frac{1}{4}$llen, K.; BrÃ©das, J.-L.; Beljonne, D. *Journal of the American Chemical Society* **2005**, *127*, 4744–4762.

[81] May, V.; Kühn, O. *Charge and Energy Transfer Dynamics in Molecular Systems*, 2nd ed.;
Wiley-VCH: Weinheim, 2004.

[82] Bulovic, V.; Burrows, P. E.; Forrest, S. R.; Cronin, J. A.; Thompson, M. E. *Chem. Phys.* **1996**, *210*, 1–12.

[83] Conboy, J. C.; Olson, E. J. C.; Adams, D. M.; Kerimo, J.; Zaban, A.; Gregg, B. A.; Barbara, P. F. *The Journal of Physical Chemistry B* **1998**, *102*, 4516–4525.

[84] Gregg, B. A. *The Journal of Physical Chemistry B* **2003**, *107*, 4688–4698.

[85] Gregg, B. A. *The Journal of Physical Chemistry* **1996**, *100*, 852–859.

[86] Gregg, B. A.; Hanna, M. C. *Journal of Applied Physics* **2003**, *93*, 3605–3614.

[87] Gómez, U.; Leonhardt, M.; Port, H.; Wolf, H. C. *Chem. Phys. Lett.* **1997**, *268*, 1–6.

[88] Giaimo, J. M.; Lockard, J. V.; Sinks, L. E.; Scott, A. M.; Wilson, T. M.; Wasielewski, M. R. *J. Phys. Chem. A* **2008**, *112*, 2322–2330.

[89] Scholz, R.; Kobitski, A. Y.; Kampen, T. U.; Schreiber, M.; Zahn, D. R. T.; Jungnickel, G.; Elstner, M.; Sternberg, M.; Frauenheim, T. *Phys. Rev. B* **2000**, *61*, 13659–13669.

[90] noz Losa, A. M.; Curutchet, C.; Galván, I. F.; Mennucci, B. *The Journal of Chemical Physics* **2008**, *129*, 034104.

[91] Zhao, H. M.; Pfister, J.; Settels, V.; Renz, M.; Kaupp, M.; Dehm, V. C.; Wurthner, F.; Fink, R. F.; Engels, B. *J. Am. Chem. Soc.* **2009**, *131*, 15660–15668.

[92] Gao, F.; Liang, W. Z.; Zhao, Y. *The Journal of Physical Chemistry A* **2009**, *113*, 12847–12856.

[93] Guthmuller, J.; Zutterman, F.; Champagne, B. *The Journal of Chemical Physics* **2009**, *131*, 154302.

[94] Fink, R. F.; Seibt, J.; Engel, V.; Renz, M.; Kaupp, M.; Lochbrunner, S.; Zhao, H. M.; Pfister, J.; Wurthner, F.; Engels, B. *J. Am. Chem. Soc.* **2008**, *130*, 12858.

[95] Clark, A. E.; Qin, C.; Li, A. D. Q. *Journal of the American Chemical Society* **2007**, *129*, 7586–7595.

[96] KLEBE, G.; GRASER, F.; HADICKE, E.; BERNDT, J. *ACTA CRYSTALLOGRAPHICA SECTION B-STRUCTURAL SCIENCE* **1989**, *45*, 69–77.

[97] Hellweg, A.; Grün, S. A.; Hättig, C. *Phys. Chem. Chem. Phys.* **2008**, *10*, 4119–4127.

[98] Peach, M. J. G.; Helgaker, T.; Salek, P.; Keal, T. W.; Lutnaes, O. B.; Tozer, D. J.; Handy, N. C. *Phys. Chem. Chem. Phys.* **2006**, *8*, 558–562.

[99] Jacquemin, D.; Perpète, E. A.; Scuseria, G. E.; Ciofini, I.; Adamo, C. *Journal of Chemical Theory and Computation* **2008**, *4*, 123–135.

[100] *TURBOMOLE V6.0 2009, a development of University of Karlsruhe and Forschungszentrum Karlsruhe GmbH, 1989-2007, TURBOMOLE GmbH, since 2007; available from* `http://www.turbomole.com`, 2009.

[101] Weigend, F.; Häser, M.; Patzelt, H.; Ahlrichs, R. *Chem. Phys. Lett.* **1998**, *294*, 143–152.

[102] Hättig, C.; Köhn, A. *J. Chem. Phys.* **2002**, *117*, 6939–6951.

[103] Hättig, C.; Weigend, F. *J. Chem. Phys.* **2000**, *113*, 5154–5161.

[104] Eichkorn, K.; Weigend, F.; Treutler, O.; Ahlrichs, R. *Theor. Chim. Acta.* **1997**, *97*, 119–124.

[105] Eichkorn, K.; Treutler, O.; Öhm, H.; Häser, M.; Ahlrichs, R. *Chem. Phys. Lett.* **1995**, *242*, 652 – 660.

[106] Frisch, M. J. et al. *Gaussian 09 Revision A.1*, Gaussian Inc. Wallingford CT 2009.

[107] Frisch, M. J.; Pople, J. A.; Binkley, J. S. *The Journal of Chemical Physics* **1984**, *80*, 3265–3269.

[108] Gordon, M. S. *Chemical Physics Letters* **1980**, *76*, 163 – 168.

[109] Francl, M. M.; Pietro, W. J.; Hehre, W. J.; Binkley, J. S.; Gordon, M. S.; DeFrees, D. J.; Pople, J. A. *The Journal of Chemical Physics* **1982**, *77*, 3654–3665.

[110] Hehre, W. J.; Ditchfield, R.; Pople, J. A. *The Journal of Chemical Physics* **1972**, *56*, 2257–2261.

[111] Grimme, S. *Journal of Computational Chemistry* **2004**, *25*, 1463–1473.

[112] Weigend, F.; Furche, F.; Ahlrichs, R. *The Journal of Chemical Physics* **2003**, *119*, 12753–12762.

[113] Rappoport, D.; Furche, F. *JOURNAL OF CHEMICAL PHYSICS* **2005**, *122*, 064105.

[114] Bauernschmitt, R.; Ahlrichs, R. *Chemical Physics Letters* **1996**, *256*, 454–464.

[115] Fink, R. F.; Pfister, J.; Zhao, H.-M.; Engels, B. *Chem. Phys* **2008**, *346*, 275–285.

[116] Helgaker, T.; Jørgensen, P.; Olsen, J. *Molecular Electronic-Structure Theory*, 1st ed.;
John Wiley & Sons Ltd.: Chichester, 2000.

[117] Jacquemin, D.; Perpète, E. A.; Ciofini, I.; Adamo, C. *Accounts of Chemical Research* **2009**, *42*, 326–334.

[118] Tirado-Rives, J.; Jorgensen, W. L. *Journal of Chemical Theory and Computation* **2008**, *4*, 297–306.

[119] Lefebvre-Brion, H.; Field, R. *Perturbations in the Spectra of Diatomic Molecules*;
Academic Press, Inc.: Toronto, 1986.

[120] Gangilenka, V. R.; Titova, L. V.; Smith, L. M.; Wagner, H. P.; DeSilva, L. A. A.; Gisslen, L.; Scholz, R. *PHYSICAL REVIEW B* **2010**, *81*, 155208.

[121] Schäfer, A.; Horn, H.; Ahlrichs, R. *The Journal of Chemical Physics* **1992**, *97*, 2571–2577.

[122] *et al.*, R. F. F. *WAVELS a wave functions based electronic structure code*.

[123] Asmuruf, F. A.; Besley, N. A. *Chemical Physics Letters* **2008**, *463*, 267–271.

[124] Fink, R.; Staemmler, V. *Theoretical Chemistry Accounts: Theory, Computation, and Modeling (Theoretica Chimica Acta)* **1993**, *87*, 129–145.

[125] Horn, H.; Preclik, G.; Stange, E. F.; Ditschuneit, H. *Scandinavian Journal of Gastroenterology* **1991**, *26*, 867–879.

[126] Osborne, S. J.; Ausmees, A.; Svensson, S.; Kivimäki, A.; Sairanen, O.-P.; de Brito, A. N.; Aksela, H.; Aksela, S. *The Journal of Chemical Physics* **1995**, *102*, 7317–7324.

[127] Ma, Y.; Chen, C. T.; Meigs, G.; Randall, K.; Sette, F. *Phys. Rev. A* **1991**, *44*, 1848–1858.

[128] Tronc, M.; King, G. C.; Read, F. H. *J. Phys. B: At. Mol. Phys.* **1979**, *12*, 137–157.

[129] Remmers, G.; Domke, M.; Kaindl, G. *Phys. Rev. A* **1993**, *47*, 3085–3091.

[130] Bianconi, A.; Incoccia, L.; Stipcich, S. *EXAFS and Near Edge Structure*; Splinger-Verlag: Berlin, 1983.

[131] Remmers, G.; Domke, M.; Puschmann, A.; Mandel, T.; Xue, C.; Kaindl, G.; Hudson, E.; Shirley, D. A. *Phys. Rev. A* **1992**, *46*, 3935–3944.

[132] Sorensen, S. L.; Osborne, S. J.; Ausmees, A.; Kikas, A.; Correia, N.; Svensson, S.; de Brito, A. N.; Persson, P.; Lunell, S. *The Journal of Chemical Physics* **1996**, *105*, 10719–10724.

[133] Horsley, J. A.; Stöhr, J.; Hitchcock, A. P.; Newbury, D. C.; Johnson, A. L.; Sette, F. *The Journal of Chemical Physics* **1985**, *83*, 6099–6107.

[134] Davydov, A. S. *Zhur. Eksptl. i Theoret. Fiz.* **1948**, *17*, 1106–1113.

[135] Davydov, A. S. *Theory of Molecular Excitons*; McGraw-Hill book company, inc.: New York, 1962.

[136] Yassar, A.; Horowitz, G.; Valat, P.; Wintgens, V.; Hmyene, M.; Deloffre, F.; Srivastava, P.; Lang, P.; Garnier, F. *The Journal of Physical Chemistry* **1995**, *99*, 9155–9159.

[137] El-Nahass, M.; Atta, A.; El-Sayed, H.; El-Zaidia, E. *Applied Surface Science* **2008**, *254*, 2458 – 2465.

[138] Inagaki, Y.; Shirotani, I.; Konno, M.; Sato, N.; Nishi, H. *Molecular Crystals and Liquid Crystals Science and Technology. Section A. Molecular Crystals and Liquid Crystals* **1997**, *296*, 397–407.

[139] Prosser, F.; Hagstrom, S. *International Journal of Quantum Chemistry* **1968**, *2*, 89–99.

[140] Malmqvist, P.-A. *International Journal of Quantum Chemistry* **1986**, *30*, 479–494.

[141] Malmqvist, P.-A.; Roos, B. O. *Chemical Physics Letters* **1989**, *155*, 189–194.

[142] Verbeek, J.; van Lenthe, J. H. *J. Mol. Struct. (Theochem)* **1991**, *229*, 115–137.

[143] Dijkstra, F.; Van Lenthe, J. H. *International Journal of Quantum Chemistry* **1998**, *67*, 77–83.

List of Figures

List of Tables